Aspects of Structural Design with Glass

A thesis submitted by

Mark Porter

for the degree of
Doctor of Philosophy

Supervised by
Professors David Hills and Guy Houlsby

Candidate affiliations:
Balliol College and the Department of Engineering Science,
The University of Oxford.

Title:	Aspects of Structural Design with Glass
Name of Candidate:	Mark Porter
Affiliation:	The Department of Engineering Science and Balliol College
Degree:	D.Phil
Term of submission:	Trinity 2001

Abstract

Glass is being increasingly used as a structural material. In particular, its favourable aesthetic qualities have made it popular with modern designers. The most recent developments have seen glass being used as major structural elements such as beams and columns. From the engineering viewpoint these new applications present a series of design problems which need to be addressed before a coherent and safe design philosophy can be achieved.

To date there has been much work on out-of-plane loading of glass, and in-plane loading of traditional materials is well described. However, there is little published advice on design for long term, in-plane loading of glass. In reality engineers have been borrowing design concepts from the two former areas to try and satisfy the latter. In this thesis it is demonstrated that this is not satisfactory, and a new "Crack Size Design" method is proposed.

Novel contact and fracture mechanics techniques are developed in the course of this thesis, which may also be applied to more general engineering problems. Of particular interest is the evaluation of the stress intensity factors for closed edge cracks in a half plane, and a description of their growth in a bulk compressive stress field. These techniques are used in an investigation of contact loading. Contact stresses are particularly important to glass design as glass is unable to flow plastically to relieve high local stresses. Hence "soft" interlayers are often inserted between the glass and the contacting material to facilitate stress redistribution. The problem of a rigid, square-ended punch loading glass via a perfectly linear elastic or rigid plastic interlayer is analysed. The results for an edge crack under such loading conditions are then investigated and incorporated into the newly derived Crack Size Design philosophy.

Acknowledgements

I gratefully acknowledge the bodies which funded this research. These are: Pilkington plc, the British Glass Education Trust, the Overseas Research Students Awards Scheme (ORS), the University of Oxford Bursary Scheme and Kinhill Engineers.

Special thanks go to my supervisors, Professors David Hills and Guy Houlsby, for their academic advice over the course of this D.Phil. In particular, I would like to thank David for his ability to make any situation seem less dire than it appears and for providing direction at times of troubling amorphousness. Paul Warren has also been of great help, showing Pilkington's support of my work to be much more than just monetary. Finally, I would like to thank Peter Crompton for his work on Structural Glass at Oxford, as it laid the foundations for the present thesis.

Three years ago I chose my college on the basis of a nice picture in the Graduate Prospectus, as every written description basically sounded the same. Little did I know that Balliol College provides the best environment for graduates in Oxford. I have found the atmosphere at Holywell Manor to be unique, and it is my time here that will probably be my most enduring memory of Oxford.

It is the people I have known at Holywell, as much as the institution itself, which have made my time here enjoyable. Special thanks go to: Alan Kingsley for showing me that my glass is always half full, and to Lopen Larma Karma Phuntsho for teaching me that things are always half empty; to Sebastian Rapsch for rowing bow side; to Dale Smith, Simon Clarke, Clyde Seepersad and Clinton Free for their cricketing expertise in Oxford and Devon; to Carmen Bugan for exercising the right side of my brain; to Jean-Francois Crombois, Graham Stoute and Siddhartha Sivaramakrishnan for confirming the value of monogamy; and, to Julian Harris, David Hagland, Yahonnes Cleary and William Booth for our band "The Makeout Room".

Thanks also go to Claus Wisser, Sotirios Psomas, Kaori Kuribayashi, Denis Clement, Davide De Focatiis, Andras Lengyel and Alan Bloodworth who have all undertaken research in the Civil Engineering Department at Oxford and can relate to the conditions in which this thesis has been produced.

I would like to thank my parents for their continuing confidence in me and ensuring that I return home at least once a year.

Finally, and most importantly, I would like to thank Ella Robinson. Her constant support and patience were invaluable in this time apart. Her emotional strength has been inspirational and put the difficulties of doctoral research into perspective. Her expert proof reading skills were also a priceless asset in the final stages of writing this thesis.

TABLE OF CONTENTS

NOTATION

A	reference loaded area
$A_{L/S}$	variables for the interlayer/substrate used in displacement calculations of Appendices C and D
A_1	loaded area
a	edge crack length, buried crack half length, or length of corner crack across plate thickness
$a_{contact}$	crack length in a contact stress field which maximises K_{II}
a_0	initial crack length
a_1	segment 1 length in kinked crack
a_2	segment 1 length in kinked crack
$a*(t)$	design crack size
a_0^*	initial crack size based on probabilistic methods
$B_{L/S}$	variables for the interlayer/substrate used in displacement calculations of Appendices C and D
B_x	glide dislocation density
$B_{\hat{x}}^{-1}$	glide dislocation density at crack mouth
B_y	climb dislocation density
b	interlayer thickness (note that in Chapter 6, this refers to half the interlayer thickness)
b_x	glide dislocation strength
b_y	climb dislocation strength
$C_{L/S}$	variables for the interlayer/substrate used in displacement calculations of Appendices C and D
c	length of corner crack along plate depth, or point of separation of interlayer and half plane
D	factor in interface dislocation stress calculation

$D_{L/S}$	variables for the interlayer/substrate used in displacement calculations of Appendices C and D
E	Young's Modulus
$E_{L/S}$	Young's Modulus of the interlayer/substrate (half plane)
f	coefficient of friction
f_1	Coefficient of friction between the rigid punch and the interlayer
f_2	Coefficient of friction between the interlayer and the half plane
G	influence function
$G(l, y)$	Fourier transform of the Airy stress function
$g(x)$	relative shear displacement
$g(u)$	triangular distribution
h	distance of edge crack mouth from the centreline of a punch
$h(x)$	relative normal displacement
i	integer variable
j	integer variable
J_0	Bessel function of the first kind, of order zero
k	Weibull distribution parameter, or, yield strength in pure shear
K	influence function, or generic expression for a stress intensity factor
K_a	stress intensity factor at the end of a corner crack defined by dimension *a*
K_c	stress intensity factor at the end of a corner crack defined by dimension *c*
K_I	mode I stress intensity factor
K_{II}	mode II stress intensity factor
K_I^*	design mode I stress intensity factor
K_{IC}	critical stress intensity factor
K_{I0}	threshold stress intensity factor
L	member length
m	Weibull distribution parameter
n	subcritical crack growth constant, or integer for solution routines
N	direct traction, or integer for solution routines

N_{11}, N_{12}, N_{22}	factors for interface dislocation stress calculation
P	applied load, or, probability of survival, or, factor used in calculation of interlayer stresses and displacements (Appendix D)
$P_{survival}$	probability of survival
P_{total}	total probability of survival
P_U	probability of survival under a uniform applied stress
p_0	height of triangular element of pressure
$p(x)$	applied contact pressure
$\tilde{p}_c(l)$	cosine Fourier transform of applied pressure
Q	factor used in calculation of interlayer stresses and displacements (Appendix D)
$q(t)$	shear traction
R	factor used in calculation of interlayer stresses and displacements (Appendix D)
R^2	measure of the "fit" of a trendline to data. $R^2=1$ implies perfect fit
R^*	design action
r	radius from crack tip
S	section or material strength, or, shape factor, or, shear traction, or, factor used in calculation of interlayer stresses and displacements (Appendix D)
s	transition point from stick to slip on interlayer/half plane interface
T	factor used in calculation of interlayer stresses and displacements (Appendix D)
t	time, plate thickness or integration variable
t_f	time to failure
U	factor used in calculation of interlayer stresses and displacements (Appendix D)
u	coordinate of dislocation along crack length
$u_{x/y}$	displacements in the x and y directions
$u_{\hat{b}}$	vertical displacement on the upper face of the interlayer due to a centrally located triangle or pressure, relative to the origin
u_f	final displacement under the rigid punch

$u_{primary}$	vertical displacement along the top of the interlayer due to the fundamental solution
$u_{tri}(\hat{x},x)$	vertical displacement of the interlayer upper surface relative to the origin due to a triangle centred on the point $\hat{x}=x$
u_y	vertical displacement due to a triangle of pressure centred on the origin
u_0	vertical displacement on the surface of the half plane due to a centrally located triangle or pressure, relative to the origin
V	factor used in calculation of interlayer stresses and displacements (Appendix D)
v	speed of subcritical crack growth, or, coordinate of collocation point along crack length
v_0	reference subcritical crack growth speed
w	punch half width
w_{tri}	half width of triangle of pressure
x	global axis
$\hat{x}$	local axis
$\bar{x}$	local axis
Y	geometric factor in fracture mechanics calculations
y	global axis
$\hat{y}$	local axis
$\bar{y}$	local axis
a	Dundurs' constant, or, integration variable
b	Dundurs' constant
Δ	displacement
$d(x)$	Dirac delta function
x	length variable
$\Phi_{L/S}$	Airy stress function for the interlayer/substrate
k	$(3-4n)$ in plane strain, $(3-n)/(1+n)$ in plane stress
$k_{L/S}$	k for the interlayer or substrate (half plane)
l	Fourier transform variable

Γ	ratio of shear modulii
f	capacity reduction factor, or, angle around elliptical crack, or, Muskhelishvili potential
$f(u)$	function used for quadrature solution technique
f_{pre}	capacity reduction factor for residual stress in toughened glass
f_{comp}	capacity reduction factor for compression loading
q	general angle, or, angle of inclination of crack to the surface normal
q_1	angle of inclination of segment 1 of a kinked crack to the surface normal
q_2	angle of inclination of segment 2 of a kinked crack to the surface normal
s	stress
$\tilde{s}$	stress due to a dislocation
$s_{\max}$	maximum stress along member length
s_{pre}	surface residual stress in toughened glass
s_N	normal stress on the line of a crack in its absence
s_0	magnitude of uniform compression field
s_{rate}	rate of stress increase in tensile test
s_S	shear stress on the line of a crack in its absence
$s*(t)$	design stress
t	shear stress
n	Poisson's ratio
$n_{L/S}$	Poisson's ratio of interlayer/substrate (half plane)
m	shear modulus
$m_{L/S}$	shear modulus of the layer or substrate (half plane)

Chapter 1

Introduction

Traditionally, the use of glass in buildings has been limited to windows (see Figure 1.1). Used in this way glass is subject only to transient wind loading and its self weight, conditions where its brittle nature and variable strength are not significant. However, over time interest in using glass in construction has grown. Architects, fascinated with the concept of a transparent building, increased natural light levels or an open work environment, have used glass in greater and greater quantities. The most obvious example today is the fully glass clad modern skyscraper. With these developments the size of the glass panelling used has increased and the method of connection has become more complicated (see Figure 1.2), but the way in which the glass is loaded has remained essentially the same.

Figure 1.1 Traditional glass uses

Figure 1.2 Modern glass usage

In recent years designers have begun to use glass in much more structural applications. Instead of panes of glass being supported on metal beams and columns, glass is now being used to support itself through glass structural members. The aesthetic result is a totally transparent structure (see Figure 1.3). The engineering consequence is that the glass must now sustain long term, in-plane loading.

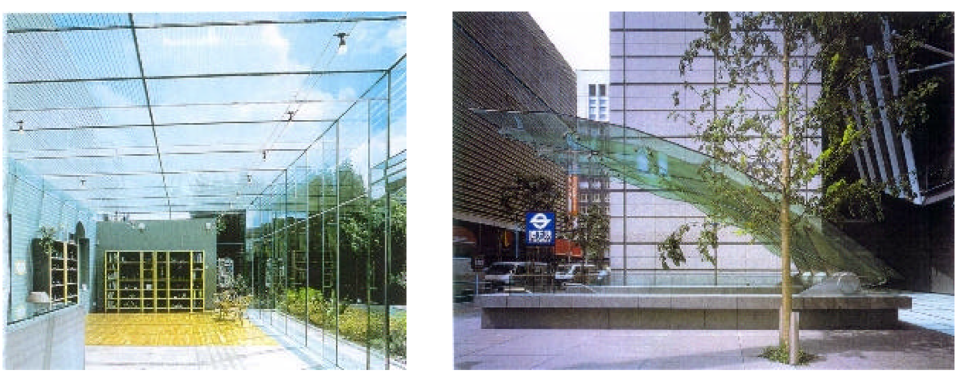

Figure 1.3 New glass structures

The properties of glass are such that it seems to behave quite differently when the loading is long term rather than short term and transient. In fact, the glass appears to become weaker as the duration of loading increases. This problem has been of little importance to traditional designers for whom the maximum load period is a several second wind gust. For the new applications, however, it is crucial to the design.

One might ask why glass is used in these new applications if it is so badly suited to them. The basic answer is cost. Glass is a mass produced product with cheap raw materials, and is therefore one of the cheapest fully transparent materials available. For example, the cantilevered structure shown in Figure 1.3 had some acrylic material included in the plies of the beams to provide a degree of ductility in case of failure. Although the volume of glass used in the other plies and the roof sheeting greatly exceeded that of the three individual acrylic plies, it was the cost of the acrylic which was greater. It can therefore be seen that glass is a crucial material if the new transparent architecture is to be widespread, because of its price. The cost is that a new structural design philosophy must be developed to account for the new application.

A detailed description of the properties of glass and its behaviour is presented in Chapter 2, but a brief account is given here for clarity. The term “glass” is often applied in the materials sciences to mean any substance which does not exhibit long range order on the molecular scale. In this thesis the term “glass” shall correspond to the popular understanding of the word, which is the substance which is used in windows. This soda-lime silica glass is a solid, non-crystalline, brittle material. It is perfectly linear elastic until failure, with a Young’s modulus of 70MPa, similar to that of aluminium. Its failure is governed by fracture, which occurs at cracks on the glass surface. In most cases these cracks are too small to be seen by eye. Owing to variation in the size of the cracks there is variation in the failure stress. Values for short-term strength might range from 20-200MPa. Glass also undergoes a loss in strength with duration of loading, which is commonly referred to as “static fatigue”. The long term strength of glass is often quoted in the range 7-20MPa. This variation in strength depends on a myriad of factors. It is predominantly affected by the surface finish but is also influenced by glass type, environmental conditions (especially humidity), production effects and others. Essentially, glass is highly predictable under normal operation, but the point at which failure occurs can appear quite random.

The literature concerning the material properties of glass is extensive. Griffith (1920) presented experimental results on glass with introduced flaws of various sizes to show that it was the flaws which determined the strength of the glass. His work is the foundation of modern fracture mechanics, which is the field that is used to describe glass failure in the material sciences. Due to the perfect linear elastic behaviour of glass it has often been the material of choice for experimentalists when investigating fracture mechanics. This means that considerable information on glass is available. Much of this information is presented in Chapter 2 and will not therefore be reproduced here.

Until recently there was little information publicly available on structural design of commercial glass. This was due to competition between glass manufacturers who also performed most of the engineering design for glass in structures. A major advancement in public glass engineering theory came with the paper of Beason & Morgan (1984). This paper focused on lateral loading of glass plates, as wind-loaded building cladding was the main use for glass at this time. The work of Beason & Morgan became the basis for many glass design codes around the world. Later modifications were suggested, such as by Fischer-Cripps & Collins (1995) and Sedlacek *et al.* (1995), which account for more localised loading conditions and more accurate fracture mechanics phenomena. The most recent method, proposed by Overend *et al.* (1999), allows for any load, support and plate geometry through the use of an equivalent stress procedure. The various design methods and scarce public information on glass have been collected in a single volume by Jofeh (1999). All of this previous work, however, has been tailored to applications of panels of glass being loaded out-of-plane.

The work on glass at The University of Oxford began when an engineering consultancy approached the Civil Engineering Department seeking assistance with a structural glass design. At this early stage the research comprised a number of fourth year undergraduate projects. Investigations of in-plane glass beam bending, column compression and contact loading were conducted. The variability in glass failure strength was demonstrated by Fair (1996) who loaded a series of annealed and heat toughened beams in bending. Strength variability was also encountered by Wren (1998) who tested cylindrical glass columns. In his experiments Wren also had to deal with a new problem: failure originating at the connections. Scarr (1997) investigated the stresses which occur due to a bearing pad connection (similar to that shown in Figure 1.4). It was shown that the inability of glass to redistribute stresses plastically results in high local stresses due to contact loading. A series of different bearing materials was used. It was found that materials of low Young's modulus were most efficient at transmitting the applied load evenly to the glass. It was also noted that small imperfections on the surface of the glass can greatly affect the resulting stress profile.

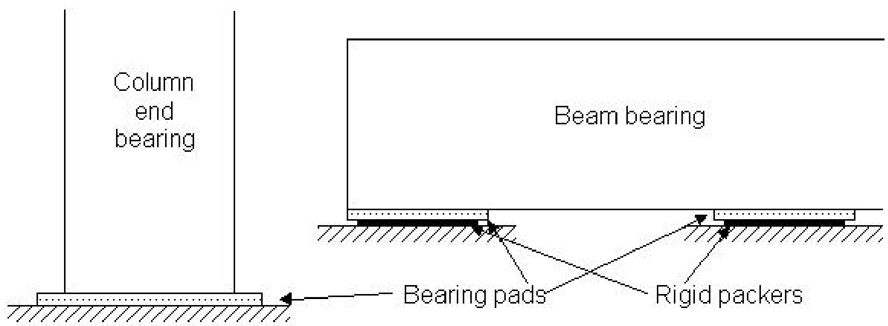

Figure 1.4 Glass being supported on pads

The projects described above focused on determining the strength of glass and the stresses developed within it under certain loading regimes. In his M.Sc thesis, Crompton (1999) studied a number of design theories and their applicability to glass. This thesis therefore represents the first real comment on glass design methods from the work conducted at Oxford.

Crompton studied the various design philosophies that have been widely used in Structural Engineering over the last century. These included Permissible Stress, Plastic and Limit State Design theories. He followed their development with the major construction materials: steel, reinforced concrete, masonry and timber. Crompton commented that Limit State Design was a derivative of Plastic Design, and therefore had an emphasis on ultimate load and strength. He showed that its application to masonry was not rigorous, as masonry rarely fails due to being over-stressed, but more frequently as a result of stability issues. Stability, as with other non-stress related actions, is poorly incorporated into current Limit State Design methods. Crompton proposed that of the four major construction materials listed above, glass was most similar to timber. This was mainly due to the variability in brittle failure stress for both materials. Indeed, Crompton concluded that of the present design methods available a Permissible Stress design similar to that used for timber was preferential to a stress based Limit State Method as used for steel or concrete when dealing with glass.

Crompton (1999) also went on to investigate a topic of current interest in glass engineering: alternative load paths. It is common in glass construction to use more than one glass member in each structural element, resulting in the widespread use of multi-ply beams, for example. Since glass is a brittle material, the failure of any single element could lead to global structural failure unless alternative load paths are provided. The consequences of failure are another reason for this added redundancy. Should the sole load path fail then overhead shards of glass could fall and seriously injure people below.

In his investigation Crompton studied the case of a multi-ply beam with a constant overall width. The same probabilistic strength statistical parameters were applied to each ply in the glass member. It was shown that as the number of plies increased, the probability of failure under a given load decreased. Hence, having alternative load paths provides greater safety in design and is more economical, as the volume of glass required for a particular stress and probability of failure reduces with increasing plies.

The thesis presented here is mainly concerned with annealed glass being loaded in-plane. In practical terms in-plane loading means that it is the edge of the glass member which experiences the greatest stresses, such as the bottom face of a simply supported glass beam. Glass is often heat or chemically strengthened to provide a layer of compression over its surface. Although aspects of this are discussed, the focus here is on the basic annealed state of the glass. More general, localised residual stresses are also omitted in this somewhat preliminary treatment of structural glass.

In the first part of this thesis a new design philosophy for glass is proposed. Termed “Crack Size Design”, it adapts conventional limit state design concepts to fit the properties and behaviour of glass. In the first instance this method is developed for uniform tension along the glass edges, and for cracks of uniform depth extending across those edges. The method is then broadened to incorporate more practical loading and cracking patterns. It should be noted that Crack Size Design, and indeed this whole thesis, is focused on designing for material failure of glass elements. Member failure modes, such as buckling, are well documented for linear elastic materials, and are independent of the variable strength of glass.

In the traditional uses of glass (see Figures 1.1 and 1.2) the compressive loads encountered are modest, and generally similar in magnitude to the tensile stresses likely to be generated. Since glass failure arises at zones of tension it is therefore the tensile stresses, rather than the compressive ones, which are critical in design. In the new structural glass applications, greater concentrations of load are found in compressive members, such as columns. Hence, an understanding of the failure mechanism in the absence of global tensile stresses is required in order to develop a rigorous design method for these members. A mathematical analysis of compressive failure in an infinite plane has only been dealt with relatively recently by such authors as Ashby and Hallam (1986) and Vaughan (1998), although experimental investigations of the failure mechanism are somewhat older, for example Hoek and Bieniawski (1965). In this thesis the failure mechanism is applied to edge cracks in compression, as edge cracks are critical in structural glass. This is done through a rigorous fracture mechanical analysis using a novel technique based on distributed dislocations. The results are used to describe the behaviour of glass in compression and hence to formulate a design method consistent with the main Crack Size Design method described earlier.

The second section of this thesis deals with connection design. Connections are more important for glass than for other materials because of its brittle nature. Due to the absence of plastic flow, the stress concentration which occurs at the connection cannot be relieved. To reduce this concentration it is normal for a layer of "soft" material to be inserted between the glass and the generally hard connecting piece, which might be a metal pin or support pad. The case of a support pad arrangement is focused on in this thesis, represented as a rigid punch with square ends, loading the glass via an interlayer of varying material properties. This might arise in the case of supports for beams or columns, as shown in Figure 1.4. Two instances are considered: in the first instance the interlayer is assumed to be perfectly rigid plastic with a low yield stress. In the second instance the pad is assumed to be linear elastic, with a low Young's Modulus.

In traditional Civil engineering design with ductile materials, bearing connections, such as those shown in Figure 1.4, are often designed by simply assuming an even distribution of “bearing” stress along the pad length. Owing to its brittleness, this is insufficient for glass and so a more rigorous analysis of these contact stresses is required. Since a fully three-dimensional solution would be computationally expensive, various simplifying assumptions are made which lead to a two dimensional analysis being undertaken here.

In the case of the rigid plastic interlayer, a slip line field theory approach is used to determine the contact loading. For the elastic interlayer, stress functions for the layer and half plane are used to calculate the contact stresses. This is done for all possible combinations of full adhesion and lubrication on the top and bottom faces of the interlayer. Distributed edge dislocations are then introduced to allow for a finite degree of friction on the half plane surface.

The stress profile results for the glass due to the contact loading show that the interlayer achieves its goal of reducing the possible stress concentrations and eliminating tension. The work on compression loading of columns in the literature demonstrates that there need not be a global tensile stress for brittle fracture to occur. It is the presence of a crack, and its behaviour in the applied stress field which determines failure. The fracture mechanical analysis used earlier for compression loading is applied later to the contact stresses of the interlayer connection. The results are used to interpret the Crack Size Design method in a manner relevant to this connection detail.

Although structural glass design was the impetus for the compression and connection analysis, the work also has a more general application to other situations encountered in fracture and contact mechanics. The solutions to the problems are valid, and computationally efficient, for any linear elastic material being loaded under the prescribed conditions. In many cases the solution method is described so that it may be applied to any specified stress profile. Some problems, such as the growth of cracks in compressive stress fields, are applicable to other situations, such as squat cracks in rail heads. Finally, the manner in which the distributed dislocation method is applied is slightly different from the traditional usage (Hills *et al.*, 1996), which may be of more general interest to researchers in the field of fracture mechanics.

Chapter 2

Development of Crack Size and Limit State Design Methods for Edge-Abraded Glass Members

2.1 Introduction

Design codes for commonly used structural materials (*e.g.* steel or concrete) make use, either explicitly or implicitly, of an assumption that the material has a certain ductility. The use of glass as a structural material is increasing, and so design methods for structural glass are being developed (Jofeh, 1999). Glass, however, is a material which exhibits no ductility whatsoever, and so it is important to question whether design methods for glass should be based on the same concepts as those used for other structural materials. The purpose of this chapter is twofold. First, it is demonstrated that the observed variability in the strength of glass is entirely explained by fracture mechanics, and that underlying this variability is in fact a true material constant, the critical stress intensity factor. Secondly this result is built upon to suggest a new framework for design with structural glass. Much further work would be required on the details of such a framework, but an outline of the basic concepts is given here.

The particular case addressed here is the use of flat glass in a long-term structural load bearing capacity, such as in beams. This use may result in higher and more variable design stresses than those encountered in glass plates. The use of glass in this way has some similarities to the use of steel, in that both materials are used to form skeletal structures, unlike concrete, which is used more in monolithic components. The similarity in application of the two materials has led some practising engineers to adopt design methods for glass based on the approach used for steel. The result is that the concept of a design or allowable stress has arisen when designing with glass.

The design stress for steel is based on its yield stress, which is a well-defined value that is highly repeatable between material tests. Such a dependable value is not available for glass. The question “What is the strength of glass?” or “What allowable stress can be used when working with glass?” often arises. When people ask such questions, the answer usually is that there is no single, minimum strength for glass. Manufacturers have charts which give probabilities associated with given stresses, and often answer such questions by saying for example “You can have 95% confidence that the glass will have a strength of at least 30MPa for the next five years”.

The stress which the glass manufacturer gives the engineer is no longer a material constant as it is for steel. The designer finds that the allowable stress is now combined with a probability of failure, and both vary with time. Yet the method of allowable stresses and the process of borrowing steel design philosophy persists, despite the fact that the fundamental material basis has changed.

This chapter shows how the strength properties of glass relevant to structural engineering can be completely explained by considering the cracks that are present on its surface. It is common for structural glass elements to have ground edges. The resulting crack patterns are used as the basis for a fracture mechanics analysis. The role of this “Crack Size Design” in the wider limit state design method is then explored. The differences between Crack Size Design used for structural glass members and existing strength models used for glass plates are outlined.

This chapter considers only glass subjected to tension, although the concepts presented may also be applied to other actions such as compression and bearing. It does not deal with the buckling of glass, which is independent of the stress at which fracture occurs.

2.2 Fracture and the observed strength properties of glass

Glass is a perfectly elastic material, and fails by brittle fracture, exhibiting no ductility whatsoever. The Crack Size Design method proposed in this chapter is based therefore on the fracture mechanics of elastic materials. To have confidence in the theory it is necessary to show that all the experimentally observed strength characteristics of glass can be explained by this theory.

2.2.1 Relevant fracture mechanics

Griffith (1920) proposed the concept of fracture based on surface energy concepts around cracks at which failure initiated. He performed experiments on glass specimens with known initial macroscopic crack sizes, and these experiments showed good agreement with his theory. Irwin (1957), and others, modified Griffith's approach to develop a stress intensity factor model. According to this model, glass will fail when the stress intensity factor K_I reaches a critical value K_{IC}. It is also a requirement that the stress intensity factor increases as the crack propagates, which is valid for most structural engineering applications. The general relationship between the stress intensity factor, the applied far-field tensile stress normal to the crack σ and the crack half-size a present is given by equation (2.1) (Anderson, 1995). The factor Y is discussed in later sections.

$$K_I = Ys\sqrt{pa} \tag{2.1}$$

Griffith's original 10 data points can be converted, using the above formula, to stress intensity factors at failure. These give a reasonably constant value of $K_{IC} = 0.47$ MPa.m$^{1/2}$. Hence Griffith's data shows that macroscopic cracks in glass obey the modern theory of fracture. Modern soda-lime silica glasses have a higher critical stress intensity factor of 0.75 MPa.m$^{1/2}$, due to different chemical composition resulting in higher glass strength.

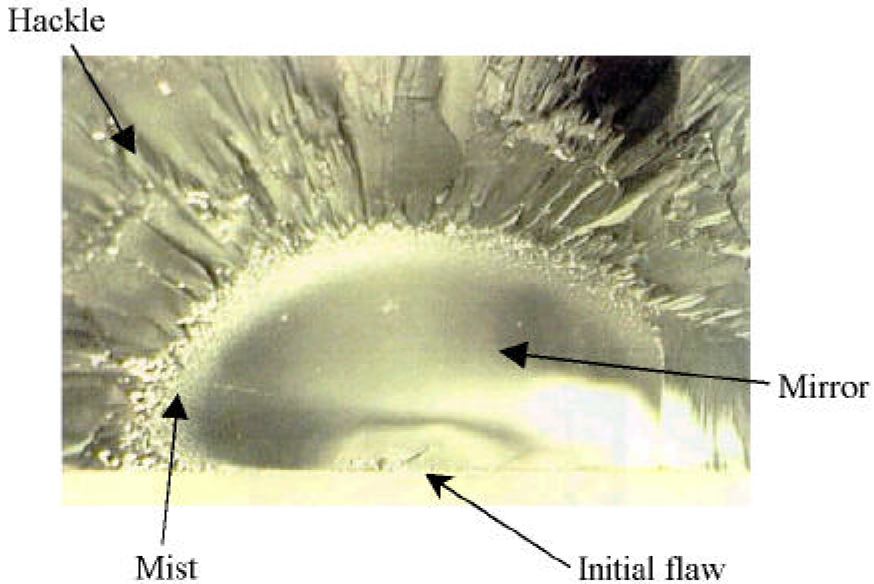

Figure 2.1 Glass failure origin

The theory of fracture at the macroscopic scale is equally valid for the microscopic cracks that are found in normal glass. Levengood (1958) conducted an extensive series of tests on regular sheet glass (80 specimens). Each specimen was investigated after failure in order to find the crack at which fracture initiated. The mirror radius (the definition of which is shown in Figure 2.1) of each failure origin was measured, and compared with the failure stress σ. Further investigation of the failure origins also revealed a relationship between the mirror radius and the size a of the original crack. The result was the linear relationship as shown in Figure 2.2, where the straight line fit is given by $\sigma\sqrt{a} = 0.579\text{MPa.m}^{1/2}$. This result is consistent with equation (2.1), and supports the theory of fracture at a critical stress intensity factor. In order to do this, a value of Y is required, and this in turn requires some simplifying assumptions about the shape of the cracks. We assume that the cracks are semi-circular in shape and that the crack depths are negligible compared to the glass thickness (the spread in data points shown in Figure 2.2 may be due to variations from this semi-circular assumption). For this case Murakami (1987) gives $Y = 0.75$, which leads to a critical stress intensity factor of 0.77 MPa.m$^{1/2}$ for Levengood's glass. This compares well with the modern value of 0.75 MPa.m$^{1/2}$. The smallest crack sizes considered by Levengood were of the order of 0.003mm, while the largest cracks considered by Griffith were 22mm. This demonstrates that fracture mechanics accurately describes the short-term strength of glass with cracks of widely differing sizes.

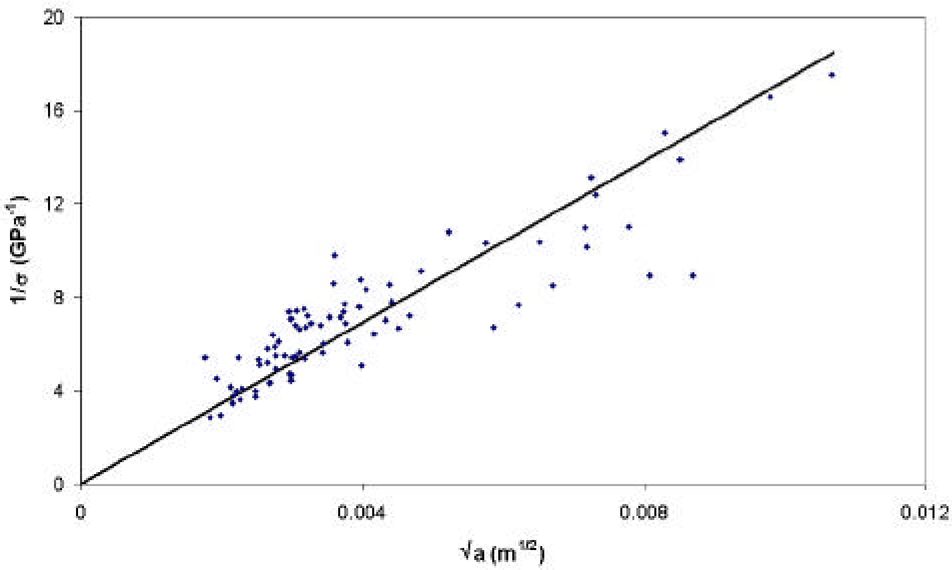

Figure 2.2 Experimental data from Levengood (1958)

2.2.2 Variability in the short term strength of glass

It is well known that the strength of glass under short term loading is not constant. Numerous works (for example, Phillips (1972)) have shown that the strength distribution of a set of similar glass specimens is modelled well by a Weibull distribution. This is based on the weakest link principle (Weibull, 1939), and is thus appropriate to glass as it is only at a single critical crack location that failure originates.

The distribution of cracks in glass and their sizes is quite variable. It depends on the handling of the glass after production, the orientation of the glass sheet in the production process and any other number of factors. Indeed, manufacturers find that there is even variability between sets of glass which have come from the same production line, but which were made at different times. If we accept the variability in crack size, then equation (2.1) shows that the failure stress will vary accordingly. This explains the inherent variability in the short-term strength of glass, and highlights that it is not the material itself, but the cracks on its surface which are variable.

2.2.3 Crack growth

When a piece of glass with a pre-existing crack is subjected to a stress less than that required to reach K_{IC}, the crack will grow with time. Figure 2.3 shows experimental data (Weiderhorn & Bolz (1970), Evans (1972)) for crack speeds where the stress intensity factor is less than the critical value K_{IC} for various environmental conditions. Figure 2.4 shows an idealisation of the experimental results. This idealisation was first suggested by Wiederhorn & Bolz (1970), and it was later shown by Evans (1974) that the experimental data gave a best fit when both axes are on a logarithmic scale, as shown in Figures 2.3 and 2.4. Figure 2.4 shows three distinct regions. Lawn (1993) discussed the graph with particular reference to the environment during loading. In slow crack growth it has been found that water is the principle corrosive agent. Indeed, Figure 2.3 shows that testing specimens in water resulted in much higher propagation speeds than when testing in dry air. The value of K_{IO} in Figure 2.4 is a threshold below which no slow crack growth occurs, and its value is a function of the humidity and temperature during loading. Region I is shown as a straight line with a slope which also depends on the environment. Region III shows another linear relationship which corresponds to the crack propagation relationship for glass in a vacuum. As the crack speed increases the supply of OH^- ions in water to the crack tip tends to zero, thus making the crack growth behaviour revert to that in a vacuum. Region II is a transition zone between regions I and III, and is again dependent on the environment.

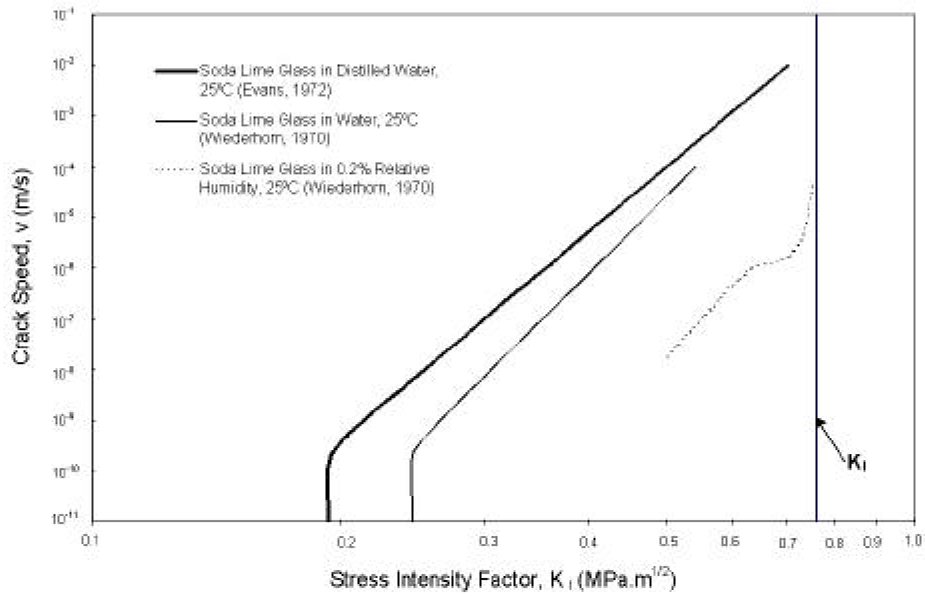

Figure 2.3 Slow crack-growth speed data

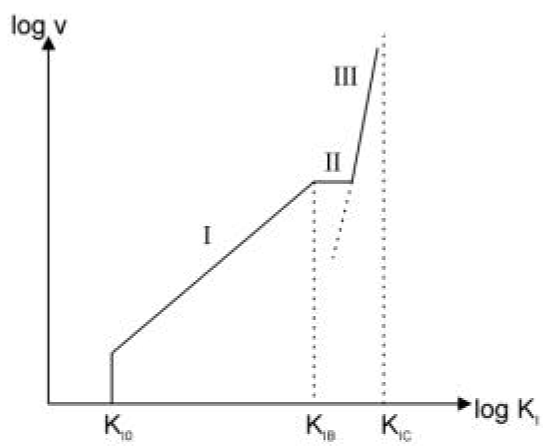

Figure 2.4 Idealised crack propagation speed versus stress intensity

Crack speeds in regions II and III are very high, so that slow crack growth in these regions leads to failure in a matter of seconds. Since structural engineering projects are generally expected to last for decades, it seems reasonable to base design solely on the slow crack growth of region I. The common expression for the rate v at which this region I growth occurs is shown in equation (2.2) (Lawn, 1993), where K_I and K_{IC} are as defined above, and v_0 and n are constants for a given set of environmental conditions.

$$v = v_0 \left(\frac{K_I}{K_{IC}} \right)^n \tag{2.2}$$

2.2.4 Static fatigue

The duration for which a constant stress can be sustained by a piece of glass reduces as the stress increases, as shown in Figure 2.5. This decrease in static strength with time is usually referred to as “static fatigue”.

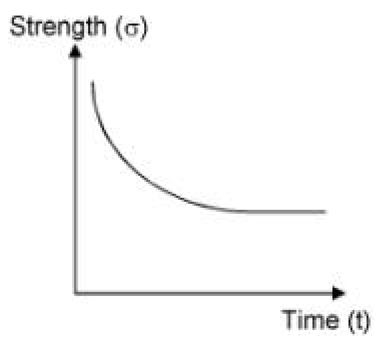

Figure 2.5 Variation in strength with duration of loading

During loading the crack size increases at a rate described by equation (2.2). Over time the critical crack grows to such an extent that, under the applied load, the stress intensity factor reaches the critical value and failure occurs. Figure 2.5 is an idealisation of experimental results (Charles, 1958). Empirical relationships are usually fitted to the data in the form:

$$\sigma^n t = \text{constant} \tag{2.3}$$

Equations (2.1) and (2.2) can be combined, as in Appendix A, to give:

$$\sigma^n t = \frac{2}{(n-2)v_0}\left(\frac{K_{IC}}{Y\sqrt{\pi}}\right)^n \left(a_0^{(2-n)/2} - a^{(2-n)/2}\right) \tag{2.4}$$

where a_0 = the initial crack size

The right hand side of equation (2.4) is constant except for the term in a. This is the crack size at failure and depends on the applied stress. However, if the duration of loading is not negligible, then the final crack size will be significantly larger than the initial crack size, a_0. Since the exponent $(2-n)/2$ typically takes a value around -7, the final bracketed factor is dominated by the term in a_0. Since this is a constant, the right hand side then reduces to an almost constant value. Comparing equations (2.3) and (2.4), it can be seen that the observed variation of strength with time is entirely explained by the equations of crack growth, and the exponent n in equation (2.3) obtained from experimental work is the same exponent as in equation (2.2).

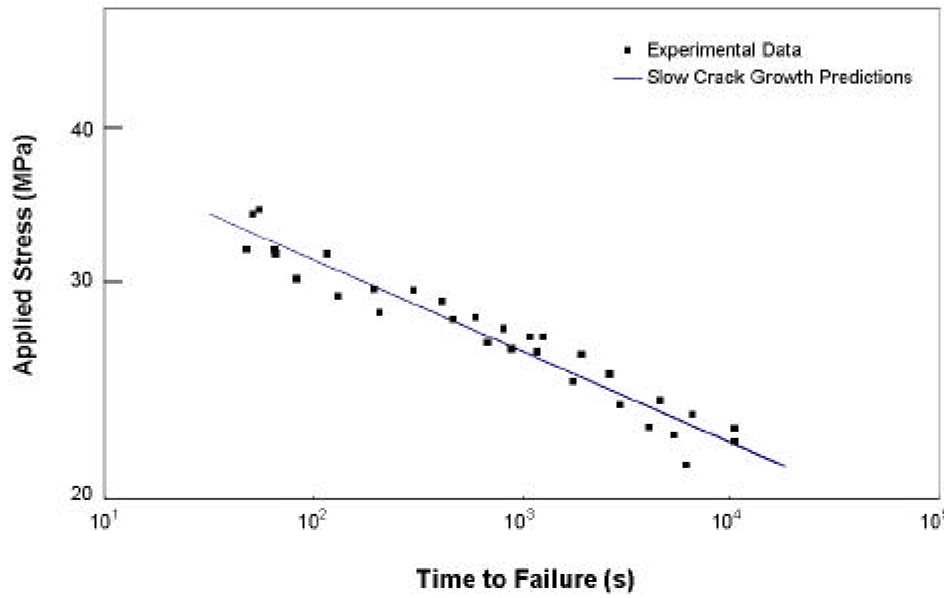

Figure 2.6 Results and predicted values from Sglavo (1997) for applied constant stress versus time to failure

Sglavo (1997) did extensive work on the long-term and cyclic strength of glass. A series of glass rod beams with uniform initial indentation cracks were tested in bending. For this case the equation for the stress intensity factor is different from equation (2.1), due to the crack geometry and residual stresses. The results of these tests are shown by the points in Figure 2.6. Also shown on the same plot is the line representing the predictions of slow crack growth model of equation (2.2). There is good agreement between the experimental and predicted results, hence verifying equations (2.2) and (2.4). There is therefore good experimental evidence to show that the model of slow crack growth of equation (2.2) is valid for glass and that it describes the process of static fatigue.

2.2.5 Minimum long term strength

Equation (2.3) suggests that, even for a very small stress, there will still be slow crack growth and a corresponding degradation in strength over time. This is not observed in practice. It has been demonstrated (see for example Wiederhorn(1970)) that there is a stress intensity factor below which slow crack growth does not occur. This threshold stress intensity factor K_{IO} is shown in Figure 2.4. This property is reflected in Figure 2.5 by the strength becoming constant for very long time periods.

It is important to note that the minimum strength of glass is related to a threshold stress intensity factor, rather than a unique minimum stress. If the initial crack size is known then a minimum long-term stress strength can be determined. If, however, during the loading history of the member this stress is exceeded, then cracks will grow, resulting in a lower subsequent minimum strength, even if the stress then reverts to its initial value.

2.2.6 Cyclic loading

In many materials it is found that cyclic loading at loads lower than the ultimate strength will still cause failure. Is this the case for glass? One possibility is that the effects of cyclic loading are simply represented by the appropriate growth of cracks during each application of loading.

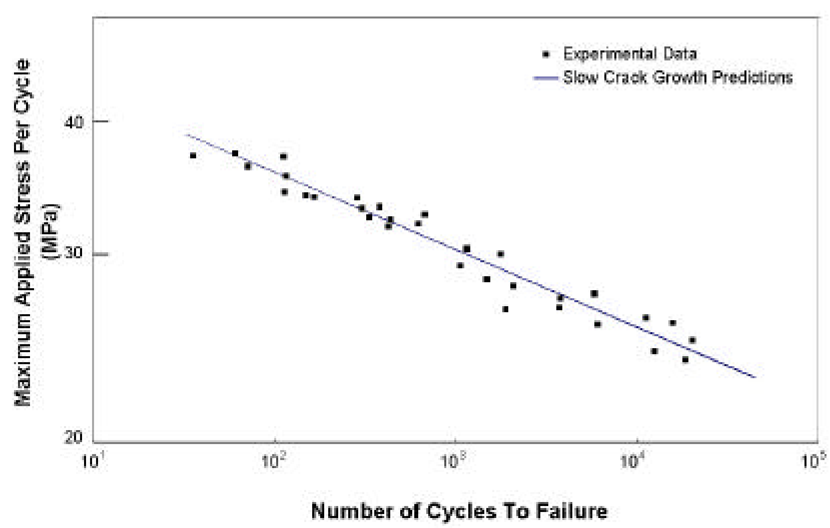

Figure 2.7 Cyclic fatigue test results and predicted values in terms of cycles to failure against applied maximum stress (after Sglavo (1997))

Cyclic loading of glass was considered by Sglavo (1997). Figure 2.7 shows the results obtained in comparison with predictions. The predicted failure values are based on slow crack growth occurring during each cycle of load in accordance with equation (2.2). Figure 2.7 shows good correlation between the experimental and predicted results and verifies that the slow crack growth approach is valid. This demonstrates that there are no additional cyclic loading effects which need to be accounted for in design. This contrasts with the behaviour of some other materials, where the process of cycling proves to be more destructive than the straightforward application of a static load.

2.3 Edge cracks due to grinding

The edges of glass members are usually ground to remove major flaws and reduce the variation in crack sizes along the cut edges. The result is that the average strength is reduced but it becomes more consistent. The process involves abrasion of the glass by grinding wheels. Wheels of various roughness are used, depending on the quality of finish required. The glass is moved over the wheel so that it is in a plane perpendicular to that of the grinding wheel. The result is that the scratches produced extend from one side of the edge to the other.

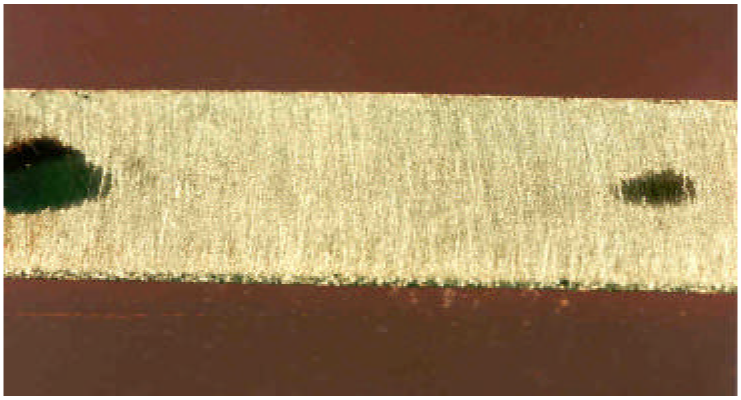

Figure 2.8 Typical edge condition of glass after grinding

Figure 2.8 shows a typical scratch pattern produced by grinding, with scratches extending across the whole width of the edge. The two areas of unscratched glass are a result of local "troughs" formed during the original cutting of the glass. Individual lines can be seen which confirm the cross-scratching nature of the abrading process. The implication is that the resulting cracks are edge cracks with a reasonably constant depth across the width of the plate. This information is of use because it means that cracks may be characterised by only one unknown dimension, their depth. It will be shown later how this is advantageous. In analysing such cracks using fracture mechanics the factor Y of equation (2.1) takes a value of 1.12. Grinding may leave residual stresses in the glass which would alter the value of Y. Further work is required to establish this, but for current purposes it will be assumed that an unmodified Y is correct.

2.4 The basis of “Crack Size Design”

The strength properties of glass relevant to structural engineering have now been explained by the role of cracks in glass and by use of fracture mechanics theory. It is proposed here to use this result to develop a structural design method for glass, called “Crack Size Design”.

In Crack Size Design it is assumed that “design cracks” are located at all critical points in the structure, such as in regions of maximum tension. This provides the two components required to evaluate the strength of glass: the critical crack size and the applied stress. The manner in which the strength criterion is expressed is discussed later.

Cracks grow over time as described earlier. Thus, throughout the life of the structure, there will be a gradual enlargement of the cracks, which will reduce the strength of the structure. To allow for this the design crack size must be modelled over the whole life of the structure. For each period of loading the strength of the structure is assessed on the basis of the maximum design crack size and stress for that period.

The equations used to model crack growth are given in Appendix A. It should be noted that if the stress intensity factor at the start of a loading period is less than the threshold value then no sub-critical crack growth will occur.

In Crack Size Design it is assumed that the weakest part of the member (corresponding to the location of the largest cracks) coincides with the location of the highest stresses. This is inherently conservative, but is not without precedent. Concrete also displays a variable strength: when designing with concrete the strength is taken at a value which has a low probability of occurrence. This conservative design strength is then applied to the whole structure. Hence, this aspect of Crack Size Design is already in widespread use in current structural engineering design.

2.5 Material and design constants used in Crack Size Design

2.5.1 Material constants

Only four material properties are required to design using the crack size method. The first is the critical stress intensity factor K_{IC}. For soda-lime silica glass K_{IC} is typically 0.75 MPa.m$^{1/2}$. This value is a material constant and introduces a degree of certainty into design. For a given crack size the strength of a piece of glass can be determined with high confidence via the stress intensity factor. This allows us to move away from probabilistic allowable stress concepts. The critical stress intensity factor gives the criterion for sudden failure. The material constants involved in slow crack growth are K_{IO}, v_0 and n as shown in Figure 2.4 and equation (2.2).

Figure 2.3 showed crack growth velocity data from two different sources. There are two lines representing glass tested in water at 25ºC, but these two sets of data still differ. Evans (1972) showed that the differences are not due to inconsistencies in experimental procedures, but rather between the types of glass and water used. Evans used distilled water, while the exact chemistry of the water used by Wiederhorn(1970) is not known.

Figure 2.3 shows that K_{IO} for glass in water can range from 0.18 to 0.23 MPa.m$^{1/2}$. A value of 0.2 MPa.m$^{1/2}$ is often used. Also, by extrapolating the region I linear portion of the graph to the K_{IC} line the range of v_0 is found. For dry air (0.2% humidity), v_0 is of the order of 3×10^{-5} m/s. When glass is immersed in water v_0 can rise to 0.02 m/s. For the normal use of glass v_0 is often taken as 0.0025 m/s.

It was shown earlier that the constant n in equation (2.5) is the same variable as that used in equation (2.2). Charles (1958) performed extensive experiments under various environmental conditions and found for a relative humidity of 100% that n was consistently 16. This value may vary between 12 and 20 for other values of humidity, but 16 is generally accepted as a representative value. Lower values of n are appropriate for a more aggressive environment.

The four material properties required for crack size design: K_{IC}, K_{IO}, n and v_0 will be material constants for a given type of glass and design environmental conditions.

2.5.2 Design constants

2.5.2.1 Initial crack size

The proposed design approach relies on the analysis of cracks in glass. Hence, to begin the design we must have an initial design crack size. There is negligible literature available on the typical crack sizes in glass at the start of a structure's life. However, there is ample experimental data on the short-term strength of glass, which can be re-interpreted for this application.

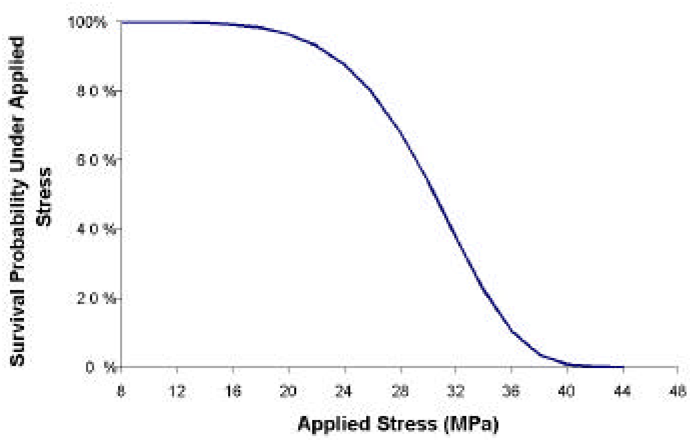

Figure 2.9 A typical Weibull strength probability plot for glass

Probabilistic glass strength data is generally presented using a Weibull distribution. A typical example is given in Figure 2.9. From such a graph it is possible to determine a stress for which there is a particular probability of survival. For example, of the family of glass specimens tested, there is a 95% probability of survival under an applied stress of 20 MPa. The stress of 20 MPa can be converted by the critical stress intensity factor and equation (2.1), to find the crack size which initiated failure. Since we are assuming edge cracks due to grinding, there is only one crack size variable to be determined based on the strength data: the crack depth. There is a 5% chance that this size of crack will be exceeded in the given sample of specimens. This allows a choice of an initial crack size for an appropriate design probability of survival.

It is unlikely, however, that the area of glass tested will be the same as the area of glass to be used in the structural member, so it is necessary to account for area effects. These are discussed by various authors (Sedlacek *et al.* (1995), Fischer-Cripps & Collins (1995)). Equation (2.5) gives an expression for the initial crack size a_0 as a function of the desired survival probability P, the loaded edge area of the member A_1, Weibull distribution variables (k and m) and the fracture mechanics quantities defined earlier:

$$a_0 = \left(\frac{K_{IC}}{Y\sqrt{\pi}}\right)^2 \left(-\frac{kA_1}{\ln P}\right)^{2/m} \tag{2.5}$$

The derivation of equation (2.5) is given in Appendix B. It is important to note that the Weibull variables must be derived from tests relevant to the application of the glass, that is from experiments on edge abraded members. The survival probability P is then the main variable which affects the material strength for the whole life of the structure.

It is important to note that the stresses obtained from a Weibull distribution of initial crack sizes, such as in Figure 2.9, are not constant for glass of a given type. They vary with time (since cracks will grow), environment and the different initial crack distribution. Thus the initial design crack size will not be constant for all projects, but will need to be evaluated for every set of glass to be used.

For a crack which is perpendicular to the surface, the factor *Y* in equation (2.5) is 1.12. When the crack is inclined to the perpendicular this *Y* factor varies. However, under the uniform far-field tension that is considered here, the inclined crack grows with a kink which is perpendicular to the surface, as shown in Figure 2.10. Yingzhi & Hills (1990) showed that such a crack orientation could be accurately modelled (that is, result in the same stress intensity factor) by an equivalent perpendicular edge crack, as shown in the figure. By considering slant edge cracks as equivalent perpendicular cracks they may be incorporated into the method described earlier for determining an initial crack size for design.

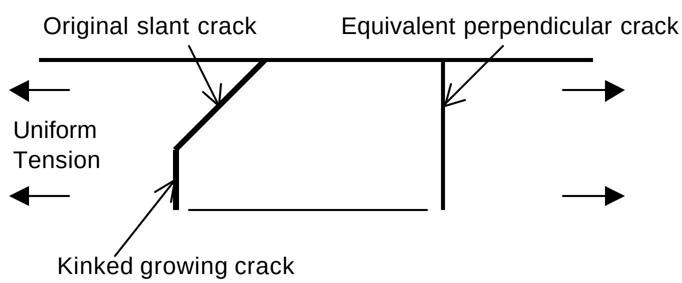

Figure 2.10 The slant edge crack and its perpendicular equivalent

2.5.2.2 Event crack size

If the design crack is modelled based only on the load history, no account is taken of possible random events in the life of the structure. Such events might include the impact of airborne debris. It is proposed here that an additional “event crack size” be incorporated into the design, most conservatively at the start of the design life, to allow for events which occur independently of the load history.

2.6 Crack Size and limit state design

Every crack size design must begin with an anticipated design stress history $\sigma^*(t)$. An example of such a history is shown in Figure 2.11. This, in turn, allows us to establish a design crack size history $a^*(t)$, based on slow crack growth theory, as shown in Figure 2.12.

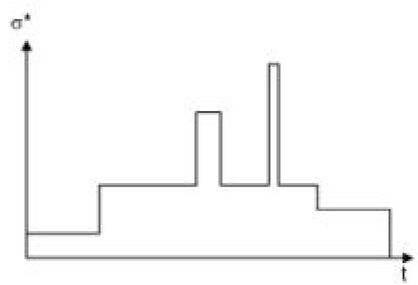

Figure 2.11 Example stress history

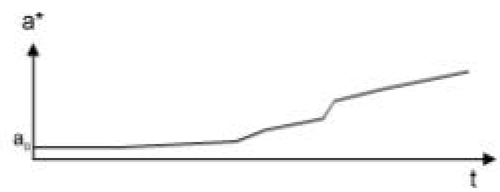

Figure 2.12 Design crack size history

Now consider how these design histories relate to limit state design. The generic requirement of design in limit state theory could be given as:

$$R^* < \phi S \tag{2.6}$$

where R^* is an appropriate measure of the design action on the structure, including the loads on the structure and factors which take account of uncertainties in loading. On the right hand side ϕ is a capacity reduction factor and S is the appropriate section, member or material strength.

The question now is "What are appropriate measures of R^* and S for glass?". It was shown earlier that the basic strength relationship, equation (2.1), incorporated the critical stress intensity factor, the applied stress and the crack size. To fit Crack Size Design into the limit state framework it is necessary to identify which of these three components will form the point of comparison between the structural capacity and the applied actions.

It was demonstrated previously that, for a given crack size and applied stress, it is the stress intensity factor which determines whether failure will occur. The critical stress intensity factor K_{IC} is the material strength property which remains constant as the failure criterion throughout the life of the member, regardless of the combination of applied stress and crack size. This suggests that the most rational choice for S in equation (2.6) is K_{IC}, which is a true measure of the material strength.

The left hand side of equation (2.6) must now also be in the form of a stress intensity factor. Let us call this the design stress intensity factor K_I^*, which will be a function of time:

$$K_I^* = Y\sigma^*\sqrt{\pi a^*} \tag{2.7}$$

This relationship combines the design stress and design crack size into a single variable.

We can now express equation (2.6) in terms of stress intensity factors:

$$K_I^* \leq \phi K_{IC} \tag{2.8}$$

The left hand side of equation (2.8) represents the design actions on the structure, including uncertainties in loading over the life of the member, while the right hand side gives a material strength which is independent of time. This strength criterion is illustrated in Figure 2.13. Expressing the strength criterion as in equation (2.8) provides an appropriate method for incorporating Crack Size Design into limit state design methods.

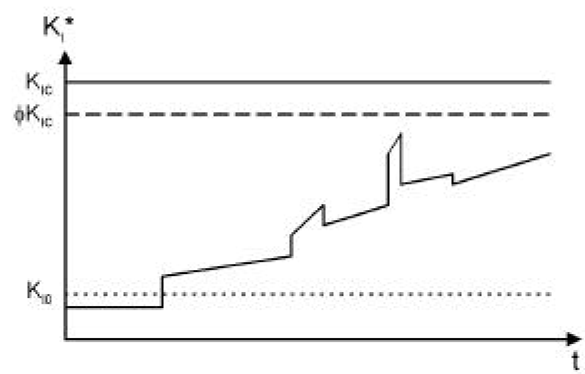

Figure 2.13 Stress intensity factor based design

2.7 Advantages of Crack Size Design

2.7.1 Increased certainty in design

At present glass designers have to make use of both a stress and a probability. They know from testing that the glass they are using has, say, a 95% chance of survival under a given short-term stress. For those designing for transient lateral forces this is all that is required. For structural glass applications however, long-term strengths need to be considered. This involves the use of a different strength and associated survival probability for various stages of the design life. Designing with glass then becomes a complex exercise in the use of probabilities and judgements of acceptable failure risks.

Using Crack Size Design only one probabilistic calculation is required. Once an acceptable failure risk *for the whole life of the structure* has been determined, a statistically acceptable initial crack size is defined. All subsequent design is then based on this crack size and its implied failure risk, right up to the design life of the project. Hence the need for repeated use of statistically determined strengths is avoided.

2.7.2 Possible reduction in material testing cost

Since this design method is based on crack size, an appropriate material test would be to test a piece of glass with a critical crack of known size. It would rapidly be discovered that the glass failure became highly predictable, as this test would simply confirm the value of the critical stress intensity factor K_{IC}.

A more appropriate test is the determination of the crack sizes in a normal piece of glass. Non-destructive testing, such as acoustic or thermal methods, may become available for investigating the crack sizes in large areas of glass. The use of these would mean that many pieces of glass could be tested without needing to be broken. Hence Crack Size Design would reduce material testing costs by eliminating the need for extensive breaking and thus wastage of glass. By testing full size specimens, the practice of basing design on Weibull statistics would no longer be necessary, eliminating one step in the analysis and therefore rendering the process more accurate and reliable.

2.8 Comparison with existing models

There are a number of existing glass strength models (Beason & Morgan (1984), Fischer-Cripps & Collins (1995), Sedlacek *et al.* (1995) and most recently Overend *et al.*(1999)). The differences between these models and Crack Size Design are related to the different types of loading treated in each design method. The existing models are primarily for plates of glass under uniform lateral short-term pressures. Crack Size Design is focused on glass beams, columns and struts in which sustained in-plane loading may vary substantially over time.

The plate models do take some account of long-term loads, but not in a completely rigorous manner. In some methods there is an implication that the long-term load is constant, while others incorporate varying stress levels, but not the corresponding variation in the minimum strength. For example, if the minimum strength is exceeded for any period of time, by construction loading for instance, then slow crack growth will occur. After this period of loading the minimum strength will now be lower than its initial value, due to the larger cracks present. This subtlety is easily accounted for in Crack Size Design but is neglected in the plate models.

Another advantage of Crack Size Design is that it allows designers to work directly with the stresses obtained from structural analysis. The plate models typically require designers to convert design stresses to equivalent stresses as a function of time period of loading and area of glass. No such procedure is necessary for Crack Size Design.

It is worth noting that approaches similar to Crack Size Design have been used in mechanical engineering for design against fatigue, see for instance Hopkins & Rau (1981) and Anderson (1995).

2.9 Extension of the Crack Size Design method to incorporate non-linear stress profiles

When deriving the expression for the initial crack size in section 2.5.2.1 it was implicitly assumed that the tensile stress profile along the glass edge was constant. This is because the Weibull statistics are derived from glass tested in uniform tension which, after being modified for area effects, are then applied to the member being designed. In this section this implicit assumption is investigated to determine whether a more accurate and efficient method is possible for members that experience tensile stress profiles which are not constant in magnitude.

The measured failure strengths of a family of specimens are used to generate a survival probability curve with the following general equation.

$$P_{Survival} = e^{-kA\sigma^m} \tag{2.9}$$

where k and m are Weibull distribution parameters related to a reference area loaded in uniform tension and are the same as those given in equation (2.5) of section 2.5.2.1.

Equation (2.9) can be used to extrapolate the results from the reference area tested to larger areas, A, of glass from the same family.

The Weibull function of equation (2.9) gives the probability of survival of a piece of glass of area A under a tensile stress σ. In the Crack Size Design method it is recognised that failure at the stress σ results from the presence of a crack of a sufficiently large size, say a. Hence, the Weibull distribution is re-interpreted to say that P is the probability that there will not be a crack greater in size than a present in the piece of glass of area A. The Crack Size Design method then goes on to determine an initial design crack size based on an acceptable maximum probability of survival. It is assumed that this critical crack is located at points of maximum stress within the structure.

In the course of this investigation two loading situations will be considered, uniform tension and a parabolically varying tensile stress distribution resulting from beam action. For the uniform tension case there is no doubt that the probability given in equation (2.9) is accurate for the probability of survival. However, for the parabolic case Crack Size Design assumes that the critical initial design crack occurs at the midspan where the stress is maximum. Since the cracks are randomly distributed, it is equally likely that the critical crack will occur elsewhere along the length of the beam where the stresses are less, implying that Crack Size Design is over-conservative. This section aims to develop methods by which the variation in stress can be incorporated into the initial crack size determination.

2.9.1 Problem definition

The two cases under consideration are shown in Figure 2.14. These are both for a member of length A units with associated Weibull statistic variables of k and m. The maximum tensile stress along the member edge is σ_{max}, which is common along the uniformly stress member, and varies parabolically to zero in the case of the beam.

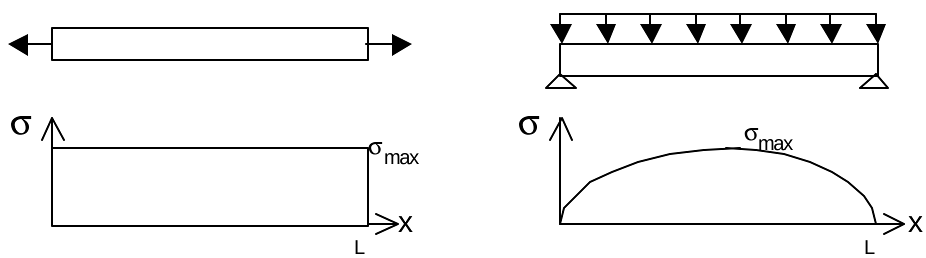

Figure 2.14 a) Uniformly stressed member b) Parabolically stressed member, as in a beam

2.9.2 Derivation of survival probability for uniform tension

The probability of survival for case (a) of Figure 2.14 is easily defined by equation (2.9), as shown below.

$$P_U = e^{-kA\sigma_{max}^m} \tag{2.10}$$

For use in Crack Size Design, stress corresponding to a desired probability of survival is converted to a crack size, a_U say. There is only a $(1-P_U)$ probability that there exists a crack size greater than a_U within the length of the member.

2.9.3 Derivation of survival probability for a specific example of a varying stress profile – viz. parabolic variation

When considering the varying tensile stress profile the beam is divided up into n

sections, each of length dx. The probability of survival within each element, where the stress is $s(x_i)$ is given by

$$P_i = e^{-kdx\sigma(x_i)^m} \tag{2.11}$$

The total probability of survival, P_{total}, is then the product of the probabilities for each element.

$$\begin{aligned} P_{Total} &= e^{-kdx\sigma(x_1)^m} \times e^{-kdx\sigma(x_2)^m} \times \ldots\ldots \times e^{-kdx\sigma(x_i)^m} \times \ldots\ldots \times e^{-kdx\sigma(x_n)^m} \\ &= e^{-kdx\left\{\sigma(x_1)^m + \sigma(x_2)^m + \ldots + \sigma(x_i)^m + \ldots\ldots + \sigma(x_n)^m\right\}} \\ &= e^{-k\int_{length}\sigma(x)^m dx} \end{aligned}$$

(2.12)

This is the probability of finding a sufficiently sized crack to cause failure under the local stress at each point along the member. Since the integral term is difficult to quantify for a parabolic stress profile it has been evaluated numerically. The integral, shown in equation (2.13), can be expressed in terms of the maximum stress, σ_{max}, and a "shape factor" S, which is dependent on the Weibull modulus m. The variation of S with m for a parabolic stress distribution is given in Figure 2.15, which demonstrates that S is less than or equal to unity.

$$\int_0^L s(x)^m dx = S s_{\max}^m \tag{2.13}$$

The reduction in the exponential factor from 1 to S for the two loading cases demonstrates that the allowance for uncertainty in critical crack location increases the probability of survival for corresponding maximum stresses, as expected.

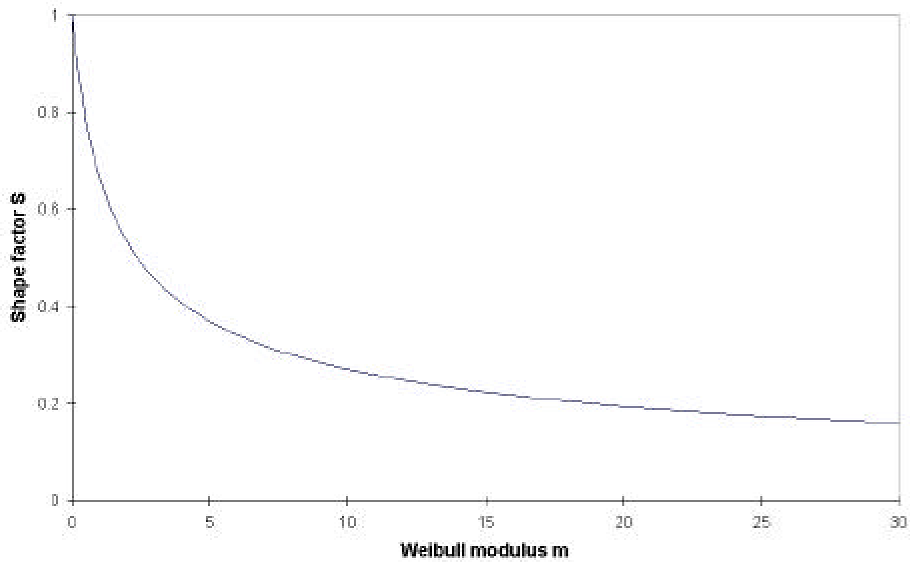

Figure 2.15 Variation in shape factor with Weibull modulus

2.9.4 Initial crack size calculation and location

With the evaluation of the survival probability function the initial design crack size is easily determined, as outlined earlier in this chapter.

Given $P = e^{-kAS\sigma_{\max}^{m}}$, then

$$a = \left(\frac{K_{IC}}{Y\sqrt{\pi}}\right)^2 \left(\frac{-kAS}{\ln P}\right)^{2/m} \qquad (2.14)$$

In the original concept it was proposed that the initial crack size be based on the Weibull probabilities for glass in uniform tension (S=1). The resulting initial crack size is one which has a chosen probability of occurrence in a given area of glass. The current modification recognises that with a varying tensile stress profile the location of the largest crack is unlikely to coincide with the position of maximum tensile stress. The new crack size is based on the probability of a crack occurring at a location in the glass of sufficient stress to cause failure. The resulting design crack is smaller than the corresponding uniform tension crack, thus representing an increase in the design capacity of the member. Since the shape function factor, S, obtained from the integral in equation (2.13), is associated with the maximum stress, σ_{max}, the design crack in the varying stress field should be assessed assuming it is located at the position of maximum stress. That is, when carrying out the full Crack Size Design, the design crack is still located at the midspan of the beam, but is now smaller due to the allowance for non-uniform stress.

2.9.5 Implications for other stress profiles

The method described above may be used for any varying stress profile where the "shape" of the variation remains constant in time. While the shape remains constant the evaluation of S from the integral of equation (2.13) is unchanged, even though the overall scale (σ_{max}) may change.

If there is significant difference in the tensile stress distribution shape then a constant S factor is inapplicable. Consider the case shown in Figure 2.16. The location of the maximum tensile stress changes with time. For such cases evaluation of a shape factor becomes very difficult. It is proposed that if large variations in the location of the maximum stress occur, that the derivation of the initial crack size revert to that of a uniform tensile stress along the member. In this case the initial crack size is one which has a chosen probability of not being exceeded along the whole length of the member, so the variation in maximum stress location becomes irrelevant, although design for each stress point is still necessary.

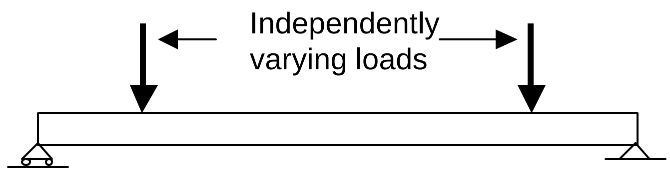

Figure 2.16 Example of loading which results in changing tensile stress distribution

2.10 Application to toughened glass

Although the main focus of this thesis is annealed glass, it is possible to comment on the implications Crack Size Design has for heat or chemically toughened glass. The emphasis here will be on heat toughened glass, as that is most common, although the concepts are equally applicable to glass toughened by means of chemical processes.

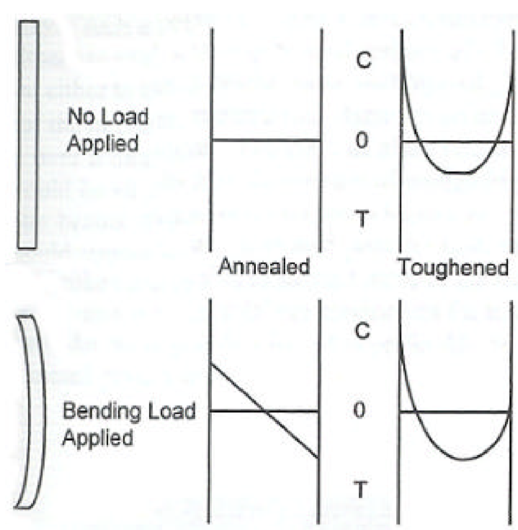

Figure 2.17 Stress profile of annealed and toughened glass

Glass is heat toughened by heating a piece of annealed glass and then cooling it very quickly. The surfaces cool fastest, and the differential cooling rate compared with the interior results in a residual stress profile, as shown in Figure 2.17. On the surface the residual stress is compressive, which is beneficial as it is tensile surface stresses which lead to failure.

Figure 2.17 shows the difference in effect of loading on annealed and toughened glass beams. In the annealed case any bending results in tension on the glass surface. In the toughened case the residual surface compression must first be overcome before tension is evident. In design the residual compressive stress is often used as an "allowable stress". Design is then much more reliant on the ability of the manufacturer to ensure a minimum level of residual compression to be used as the allowable stress. However, if the residual compression is exceeded during the lifetime of the structure, it may be necessary to employ Crack Size Design in the analysis. Also, by limiting the applied stress to the "allowable" residual stress then the additional material strength of the glass is unused, and the design is therefore possibly inefficient.

Let σ_{pre} be the compressive prestress on the surface of the glass due to heat toughening. The applied stress history is unaffected by the presence of the prestress, so that Figure 2.11 is still applicable. The difference comes in generating the new crack size and stress intensity factor histories for Figures 2.12 and 2.13. In this case the stress propagating the crack is $\sigma^* - |\phi_{pre}\sigma_{pre}|$, where ϕ_{pre} is a capacity reduction factor to account for uncertainties in the level of the prestress. The equivalent graph of Figure 2.13 will have much greater periods of loading less than K_{I0}, as most of the loading will be insufficient to cause the tensile load, σ^*, to exceed the magnitude of the prestress, $|\phi_{pre}\sigma_{pre}|$.

One added complication of glass toughening is the possibility for self-fatigue, which has been dealt with in the literature (Bakioglu *et al*., 1976). If a crack on the surface becomes sufficiently large that it extends into the tensile zone in the central region of the member, then slow crack growth may occur. This can happen even in the absence of an external load if the crack is deep enough. When slow crack growth begins under these conditions it is self-propagating, as the tensile stresses increase with depth. The result is a sudden, explosive failure as cracks extend throughout the tensile zone of the whole glass member.

Normal allowable stress design methods have difficulty in accounting for self-fatigue. They are accurate if the applied stress never exceeds the prestress, but when this does occur, they are unable to predict the point at which self-fatigue might begin, as there is no knowledge of the crack depth. Crack Size Design, on the other hand, is based on the crack size, and is therefore able to be used by the designer to investigate this failure criterion.

It has been stated earlier that this discussion is intended as a brief comment on the use of Crack Size Design for toughened glass, rather than being a full design method specifically targeted at the application. Points which have not been dealt with are given below, so as to provide a focus for possible future work.

The relative dimensions of the compression zone and the design crack have not been considered. If the depth of compressive prestress is much larger than design crack then the design method described above is accurate, but self-fatigue will not occur. In the case of the design crack being comparable in dimension to the depth of compression, the compressive prestress will vary over the crack length and will therefore cause a deviation in the fracture mechanics constant of $Y=1.12$.

It is also assumed here that the material testing required to generate a failure stress versus probability curve (such as in Figure 2.9) will be based on tests of the toughened glass members. It is possible to determine the amount of prestress with relative accuracy, which would then allow a failure stress to be converted into an initiating crack size. However, this would be tedious, and expensive, as toughened glass is much more expensive than the equivalent annealed glass. It might therefore be more practical to test the annealed glass before toughening. However, it is not known whether the toughening process has a large effect on the size of cracks present. This would need to be established before an affordable testing regime could be devised, which might then impact on the economic incentives of using Crack Size Design in industry.

Chapter 3

The application of the Crack Size Design method to edge-loaded structural glass members with corner cracks

3.1 Introduction

The Crack Size Design method proposed in Chapter 2 was tailored towards members whose edges had been ground. The cracks in this case extend across the whole thickness of the glass plate. A recent study (Williams & McKenzie, 1997) investigated the types of cracks produced at the glass edge by wheel cutters at the end of the float glass production line. The study found that corner cracks (idealised in Figure 3.1) formed the majority, and in most cases worst, of the cracks produced in the process. In addition it was shown that the crack depths, a, were rarely larger than 15% of the glass thickness, t. In highly polished, square edged glass members it is also highly unlikely that a crack will extend the full way across the thickness. In this case the critical crack will also be a corner crack. The aim of this chapter is to extend further the applicability of the Crack Size Design method to glass edges with corner cracks, as represented in Figure 3.1.

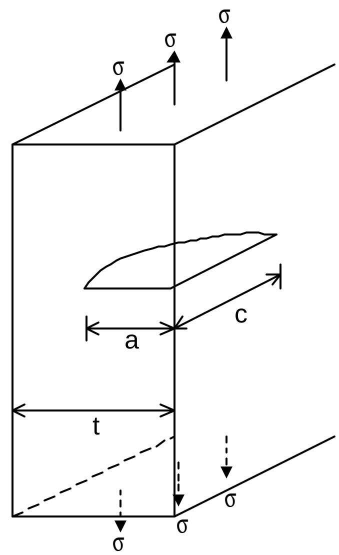

Figure 3.1 Geometry of corner crack

Being able to design for corner cracks could reduce the cost of structural glass construction. If a glass member could be designed for a non-abraded, as-cut surface, then the cost of edge processing is eliminated. Since this is expensive compared to the material cost, economic savings would result. There is no loss in aesthetic quality from using as-cut glass, as the edge away from the initial scoring marks is very smooth and has a polished appearance. However, corner cracks also occur in polished square-edged members, and so a more accurate design method for these will also be of benefit.

The Crack Size Design method is based on modelling the long term crack growth over the lifetime of a structure. It is uncertain, at the outset, whether a corner crack under stress would grow to equate the lengths a and c, or whether the larger of these two dimensions would be critical and extend rapidly to failure. This chapter focuses on how the corner crack propagates, with particular emphasis on the variation in crack aspect ratio. Also, the effect of finite plate thickness on the stress intensity factor, which might normally be investigated in a quarter plane formulation, is considered.

The long term growth patterns of corner cracks in plates of finite thickness, and a way in which to allow for them design, is the subject of this chapter. It is also necessary to determine the size of the initial crack as a starting point for design. In the initial Crack Size Design method, short-term failure stresses could be converted to a failure-initiating crack size by making use of the fact that the edge crack geometry is determined by a single parameter, the crack depth. Corner cracks, if considered simply as quarter ellipses, have two dimensions that define their shape, viz. their depth up the plate and their width across the glass thickness (dimensions *c* and *a* of Figure 3.1 respectively). It is not possible to determine from the single piece of information (the failure stress) what these two dimensions are. A way to overcome this indeterminancy in the design process is therefore sought here.

3.2 Fracture mechanics of a corner crack and the modelling method

Figure 3.1 shows a quarter ellipse corner crack under far field tension. This is an idealisation of the cracks that often occur on glass edges. Since structural glass members are deep compared to the size of the crack, the stress field caused by bending effects is assumed to be constant over the crack. The applied stress is shown as σ in Figure 3.1.

Newman & Raju (1984) performed numerous finite element analyses of the crack geometry of Figure 3.1. Their results formed the basis of empirically derived equations which are lengthy and therefore not reproduced here. Similar problems were later investigated mathematically by Zhao & Sutton (1995), whose work supports the earlier results. The Newman & Raju equations show that the stress intensity factor varies smoothly around the crack perimeter and is dependent on the aspect ratio *a/c* and the crack to plate width ratio *a/t*. Figure 3.2 shows a typical stress intensity factor distribution around the edge of a corner crack.

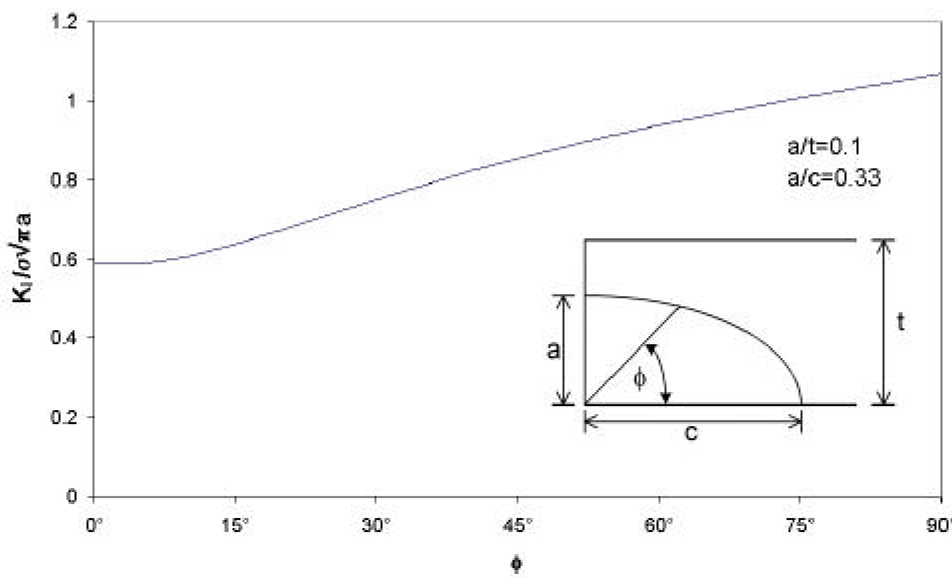

Figure 3.2 Stress intensity factor variation around crack perimeter

$$v = v_0 \left(\frac{K_I}{K_{IC}} \right)^n \qquad (3.1)$$

As the stress intensity factor varies around the perimeter of the corner crack, equation (3.1) (reproduced here from equation (2.2)) implies that the speed of crack growth, v, will also vary around the crack. Hence the dimensions of the crack will change so that the aspect ratio will not remain constant. The analysis pursued here assumes that although the aspect ratio changes, the quarter-elliptical profile of the crack remains. This assumption is made on the basis of experimental and theoretical evidence. Ohji *et al.* (1992) experimentally tracked the growth of quarter-elliptical cracks in steel. Crack propagation in steel is described by Paris' Law, which is of a similar form to equation (3.1). These experiments found that an elliptical profile was maintained. Dai *et al.* (1997) modelled the growth of a series of crack profiles, not just quarter ellipses. Their results show that the crack maintains a smooth profile, and more interestingly that even an initially "rough" crack propagates so that the profile becomes smooth and very nearly elliptical. These results suggest that the assumption of a crack maintaining a smooth quarter-ellipse profile during loading is acceptable.

Once it is established that a quarter-ellipse profile is appropriate, the stress intensity factor at any point on the circumference of the crack may be obtained from Newman & Raju (1984). The growth of the two perpendicular crack dimensions, a and c, are modelled over time. For each time point, the Newman & Raju stress intensity factors at the two ends of the crack are used to determine the respective growth speeds, using equation (3.1), and hence the new crack dimensions and aspect ratio. This corresponds to a progression of the crack front similar to that shown in Figure 3.3. The process continues until the stress intensity factor at either end of the quarter-ellipse reaches the critical value at which point sudden failure is assumed to occur.

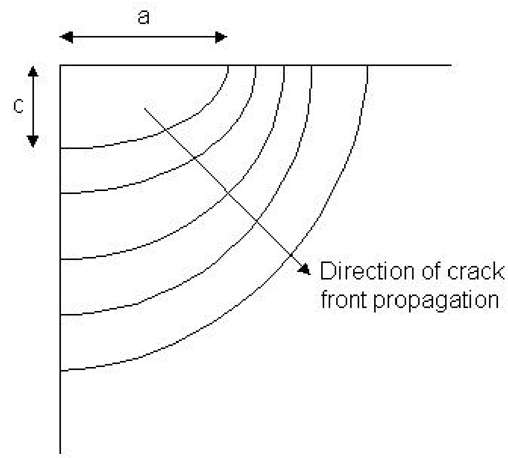

Figure 3.3 Crack front propagation with time for a quarter ellipse crack in a quarter plane

3.3 Crack growth behaviour

Figure 3.4 shows the degradation in strength with duration of loading due to crack growth, often referred to as "static fatigue". The case analysed is for an initial value of a/c=0.2. It demonstrates the well known behaviour that the stress that a piece of glass can sustain reduces with the period over which it is being loaded. The plot for the quarter elliptical crack was based on the crack growth algorithm described in the previous section. The figure shows that the current model produces results that agree with the empirically based relationship $\sigma^n t$=const (Charles, 1958).

Figure 3.5 gives a typical set of data showing the variation in crack aspect ratio over the lifetime of the cracks when subjected to constant stress. In this instance it is assumed that the thickness of the glass plate is sufficiently large compared with the crack size so that a quarter plane may be used to model the glass. The effect of thickness is discussed later.

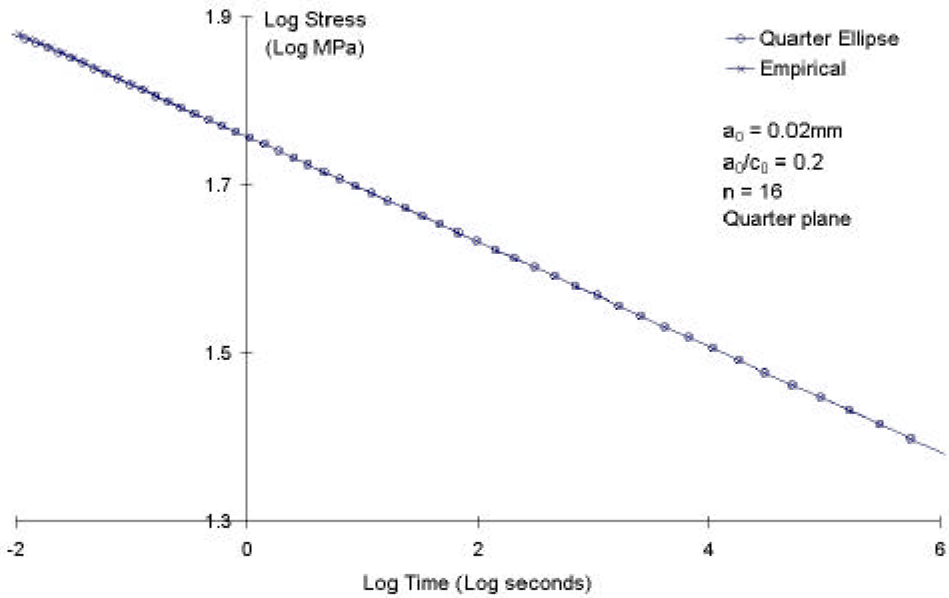

Figure 3.4 "Static fatigue" strength degradation with time

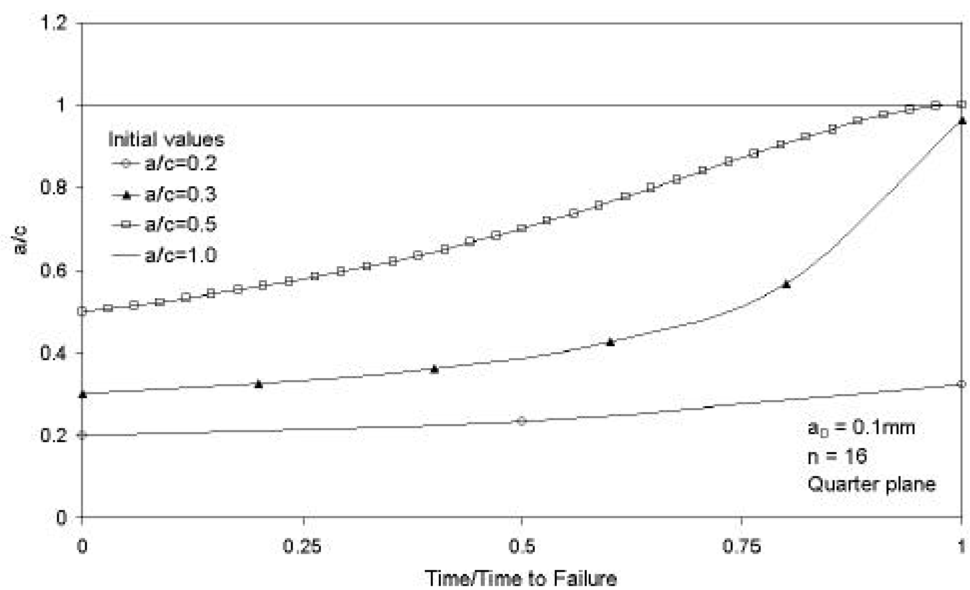

Figure 3.5 Variation in crack aspect ratio with time

The figure clearly shows that the aspect ratio tends to unity with time, that is the profile approaches a quarter circle. The failure times for each crack represented in Figure 3.5 were different, with that for a/c=0.2 being very short. For this particular case, the stress used in the model caused failure after a matter of seconds so that the initial stress intensity factor at one end of the crack was already close to the critical value and failure intervened before significant amounts of slow crack growth occurred.

The convergence to a quarter circle profile can be explained through an investigation of the fracture mechanical processes. Let K_a and K_c denote the stress intensity factors corresponding to the dimensions *a* and *c* of a quarter-elliptical crack. Figures 3.6a and 3.6b give example histories for the growth of *a* and *c* and their respective stress intensity factors. It is found that the smaller dimension has the highest corresponding stress intensity factor. For example, if *c* is twice as large as *a* then K_a will be larger than K_c. The dimension with the higher stress intensity factor will grow at a faster rate, as given in equation (3.1). This equation shows that the speed is a power function of stress intensity factor with the exponent *n*. Since *n* is generally of the order of 16 for glass, any difference between the stress intensity factors K_a and K_c will result in a proportionally much higher difference in the crack growth speed. Therefore, the crack dimensions tend to grow to a point where the stress intensity factors become equal. For an infinite quarter plane this configuration is a quarter circle. The process of convergence can be seen in Figures 3.6a and 3.6b.

If the stress is sufficiently high that the initial stress intensity factor at one end of the crack is near K_{IC}, then failure can occur before there has been much opportunity for crack growth. This results in failure at an aspect ratio lower than 1, as seen in the curve for *a/c=0.2* in Figure 3.5.

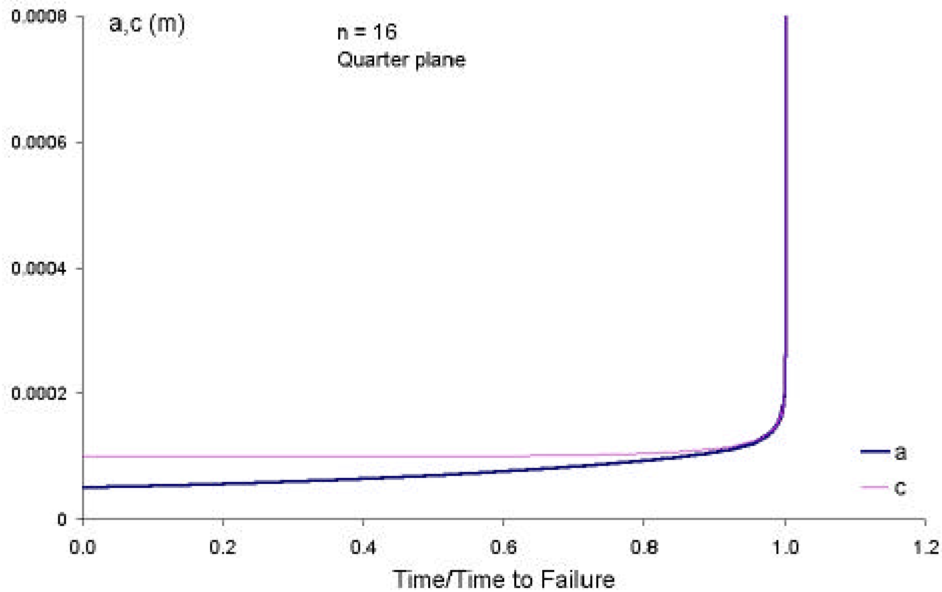

Figure 3.6a Crack size history

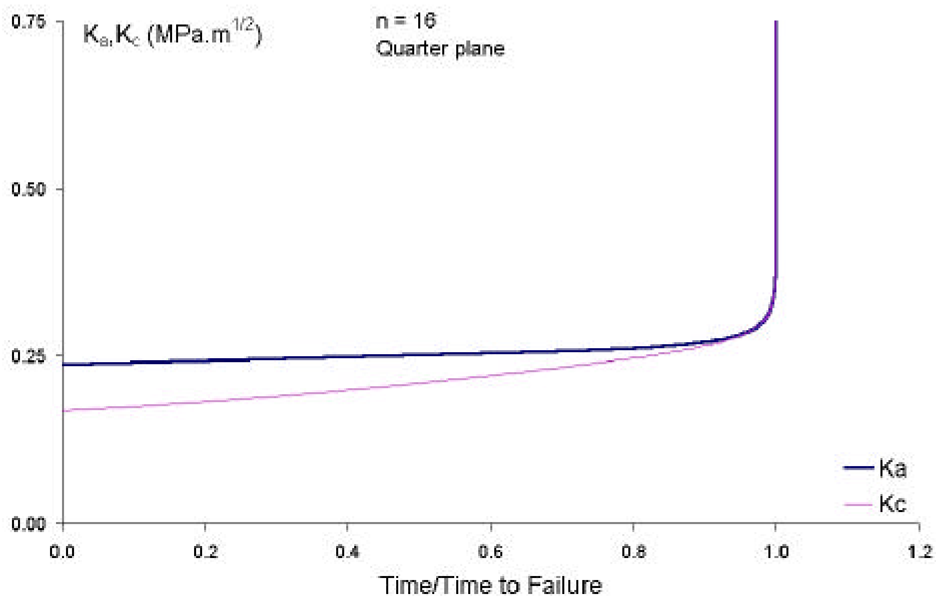

Figure 3.6b Stress intensity factor history

3.3.1 Effect of finite thickness

The introduction of a finite third boundary to the quarter plane idealisation affects the stress intensity factors around the crack. The plate thickness parameter was included in Newman & Raju's work to allow for this effect and therefore may be easily incorporated into the model being used here. Figure 3.7 gives a number of crack aspect ratio histories for a crack, but in each case with a different plate thickness. The figure shows that as the plate thickness reduces the crack propagates to a ratio less than 1. It is important to note that for these cases the final aspect ratio is still one that equalises the stress intensity factors at each end of the crack, but due to the new free boundary this point occurs for a different aspect ratio.

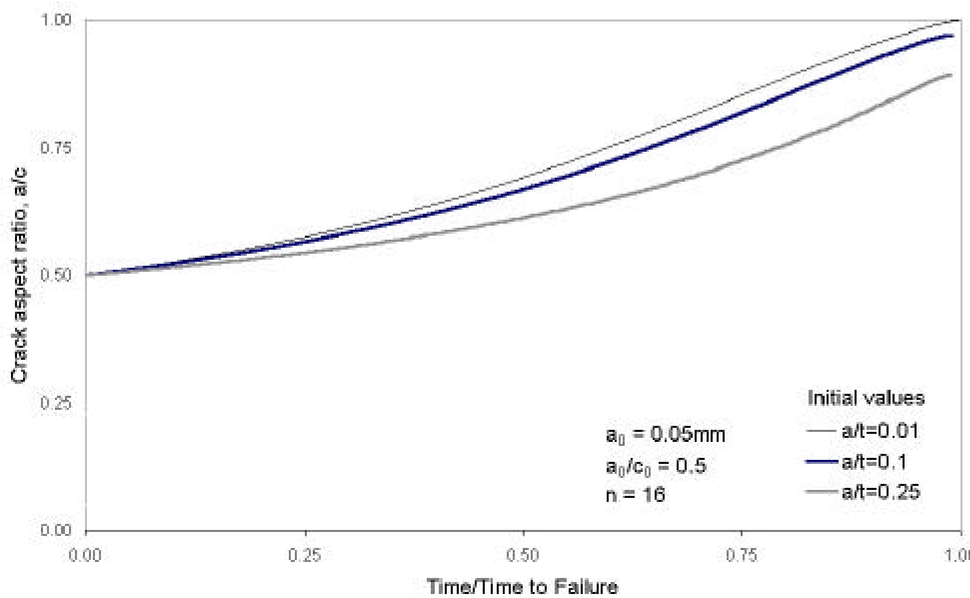

Figure 3.7 Effect of finite thickness on the crack aspect ratio history

3.3.2 Effect of *n*

It has been discussed earlier that the progression towards an aspect ratio of unity is based on the different speeds of crack growth at either end of the crack when the stress intensity factors are unequal. Crack growth speed is dependent on *n*, as given in equation (3.1). Figure 3.8 shows the effect that different values of *n* have on the aspect ratio history of a crack. The values of 12 and 20 are the typical limits encountered for *n* in glass design. The figure demonstrates that these values of *n* are all sufficiently large to result in a migration towards a quarter circle profile.

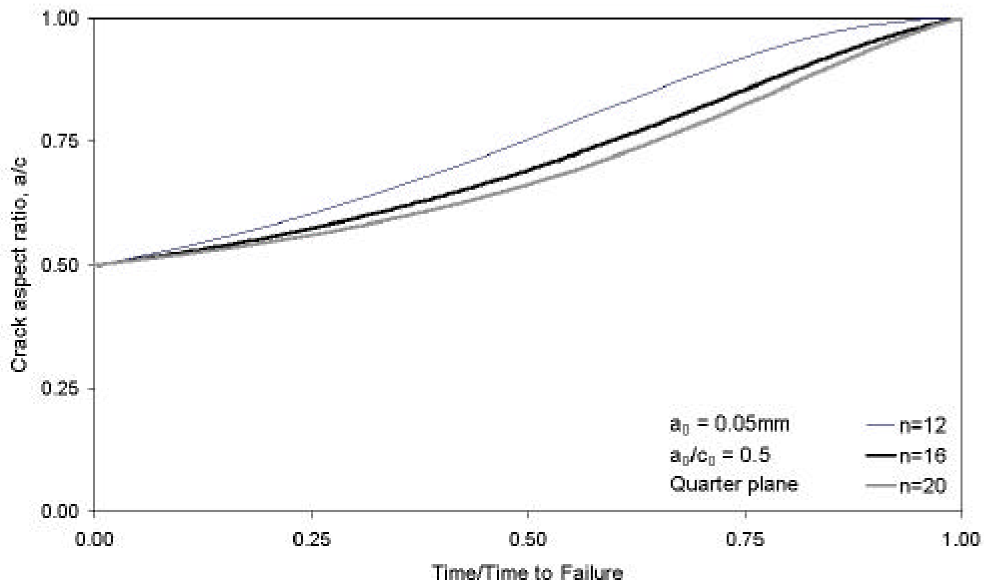

Figure 3.8 Effect of *n* on the crack aspect ratio history

3.4 Proposed design modelling method

The behaviour of corner cracks as they grow, determined in the previous sections, is summarised diagrammatically in Figure 3.9. It shows there to be three basic termination conditions for the analysis. In case (a) the initial conditions result in a stress intensity factor at one end of the crack which is sufficiently high to cause failure after minimal slow crack growth. This corresponds to a short failure time, generally on the scale of seconds. Since structural engineering projects are required to last many decades, this condition is not relevant to design. In cases (b) and (c) the initial stress intensity factors are sufficiently low that significant slow crack growth occurs with time. In the latter case, (c), it is noted that the corner crack may extend the whole way across the glass plate thickness, invalidating the assumed geometry of the current analysis. However, it was given in section 3.1 that the corner cracks encountered in practice are rarely larger than 15% of the glass thickness, implying that this termination condition will be encountered rarely in design situations. Finally, (b) represents the case where the corner crack grows to equalise the stress intensity factors at either end of the crack, and this corresponds to a final crack aspect ratio approaching unity.

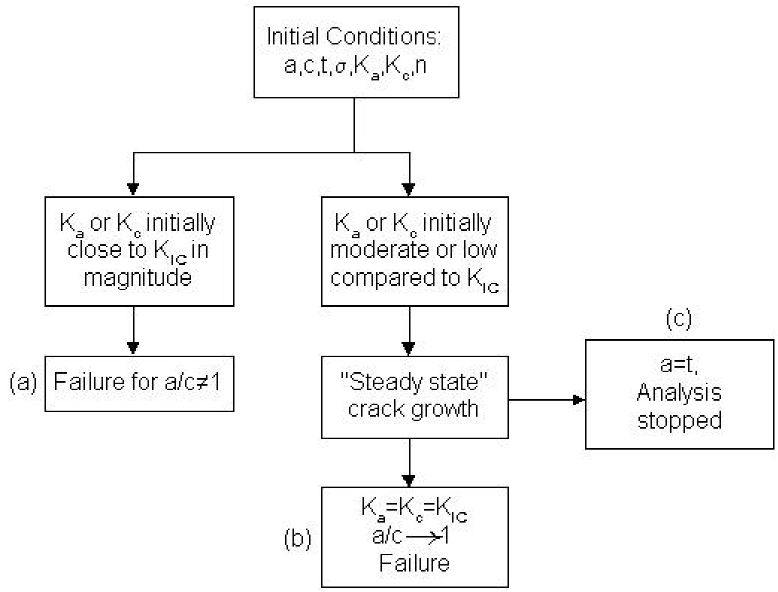

Figure 3.9 Diagrammatic representation of the corner crack growth process

It has been discussed earlier that material strength testing is not able to provide sufficient information to determine both dimensions *a* and *c* of corner cracks in glass. However, it has been shown that, regardless of the initial aspect ratio, the crack will propagate so that it approaches a quarter ellipse, or more precisely a quarter circle, for general structural glass applications. It is proposed here that a design corner crack be assumed which initially has a quarter circular profile, and that it grows maintaining this shape. This assumption is based on the above observation that cracks usually approach this profile. Only one dimension needs to be considered, that is the radius. The short term strength data can therefore be used to calculate an equivalent crack radius. Design then continues as described in the initial Crack Size Design method of Chapter 2 where the crack dimension being analysed is the radius rather than the through thickness depth.

The accuracy of the design that can be achieved with this approximation is addressed in the remaining sections of this chapter.

The assumption of a quarter circle, and therefore a fixed aspect ratio, uncouples the dependence between the aspect ratio and crack growth rate which resulted from substituting the Newman & Raju functions into equation (3.1). The stress intensity factor can now be described in the standard form, $K_I = Ys\sqrt{pa}$, where Y becomes 0.722.

The remainder of this chapter is concerned with investigating the accuracy of the proposed model via a series of numerical analyses of glass members with quarter elliptical cracks (of different aspect ratios) and their corresponding quarter circle design crack equivalents.

3.5 Initial conditions

It is necessary to determine how to calculate the initial size of this design crack for the new design method. This will be done using information provided by the short term failure stress test. In standard testing methods glass is loaded with a linearly increasing tensile stress (see, for example, Williams & McKenzie (1997) or Ritter *et al.* (1985)). The rate of stress increase might range from 0.5 to 5 MPa/s. It is well established that slower rates of stress increase result in lower failure stresses, as there is a longer time for subcritical crack growth to occur. Hence, although the failure stress results are recorded for short time periods they do not represent an instantaneous failure stress.

The equivalent quarter circle design crack size used in this work is one that would grow to fail at the same stress after the same duration of loading as the crack which leads to failure in the short term test, as shown in Figure 3.10. To determine the initial crack size the time to failure and stress rate from the test are required. For a quarter circle crack in an infinite quarter plane, the fracture mechanics equations of Newman & Raju (1984) and the slow crack growth equations of Chapter 2 can be manipulated to give,

$$a_f = \left[\frac{2-n}{2(n+1)} v_0 \left(\frac{Ys_{rate}\sqrt{p}}{K_{IC}} \right)^n \left(t_f^{n+1} - \left(\frac{K_{I0}}{Ys_{rate}\sqrt{pa_0}} \right)^{n+1} \right) + a_0^{\frac{2-n}{n}} \right]^{\frac{2}{2-n}} \tag{3.2}$$

where a_f = crack size at failure = $\frac{1}{p}\left(\frac{K_{IC}}{Ys_{rate}t_f}\right)^2$

s_{rate} = the rate of stress increase from the short term test

t_f = time to failure of the test specimen

K_{I0} = threshold stress intensity factor below which no slow crack growth occurs

a_0 = initial crack size

Equation (3.2) gives the final crack size at failure and may be used to find the equivalent initial crack size which led to that failure. This initial equivalent crack is then the one that defines the size of the design crack at the start of the life of the glass member and it is the modelling of the subsequent growth of this crack which is the basis of Crack Size Design.

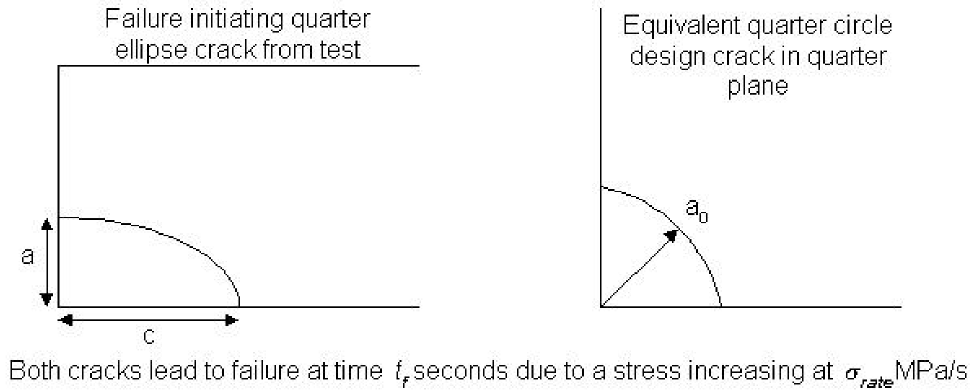

Figure 3.10 The quarter ellipse crack in a finite thickness plate (left) and the equivalent quarter circle crack in a quarter plane which is used for design (right)

3.6 Effect of thickness on design

In earlier sections it was shown that, even with finite width, the assumption of progression towards an aspect ratio of 1 was still reasonably accurate. However, the third edge also has an impact on the stress at which failure occurs. Figure 3.11 shows the stress degradation curve for a series of simulated glass members. Each has the same initial crack size, but the glass plate thickness varies. The figure shows a general but slight trend of decreasing strength with increasing crack to thickness ratio.

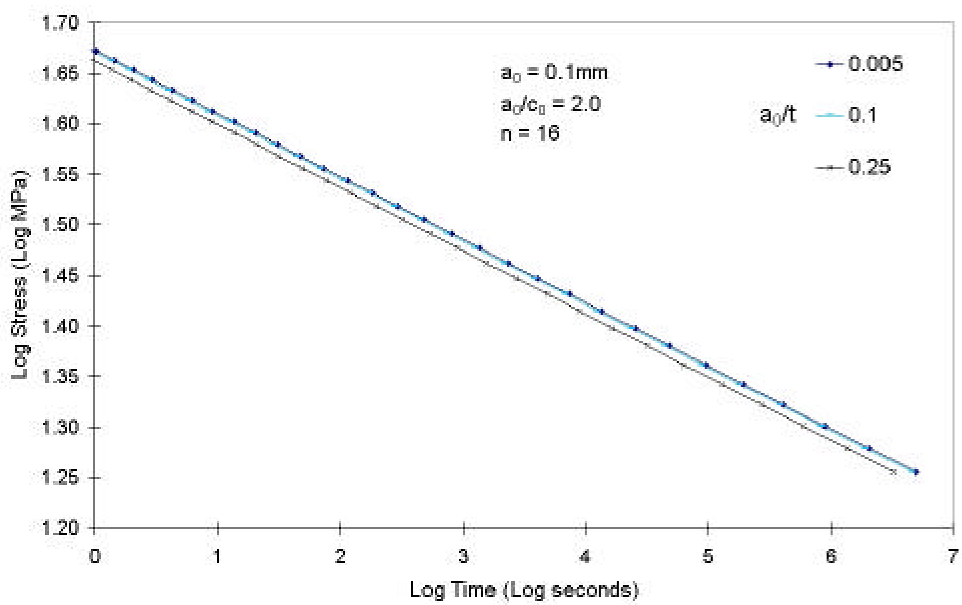

Figure 3.11 Static Fatigue curves for glass specimens with varying thickness

The question is now whether the proposed modelling technique can account for the loss of strength with thickness. In the simulations the elliptically-cracked, finite thickness plate member was modelled by a circular crack in an infinite quarter plane. The initial crack size for the quarter circle crack in a quarter plane is determined from the short term failure characteristics of the quarter ellipse crack in a plate of finite thickness. Figure 3.12 shows a typical set of stress degradation curves comparing the behaviour of a series of design cracks, each with initial crack size based on a different material test stress increase rate in the short term test, with the quarter-elliptical, finite thickness original. Even though the crack to thickness ratio of $a/t=0.25$ is larger than would normally be encountered, the difference between the two cases is still remarkably small. Extensive simulation revealed that errors of less than 1% (for $n=16$) were standard for most of the lifetime of the member, although larger errors were found near the subcritical growth threshold limit. Hence the proposed model can be easily applied to finite thickness glass members, and the thickness itself does not need to be accounted for explicitly.

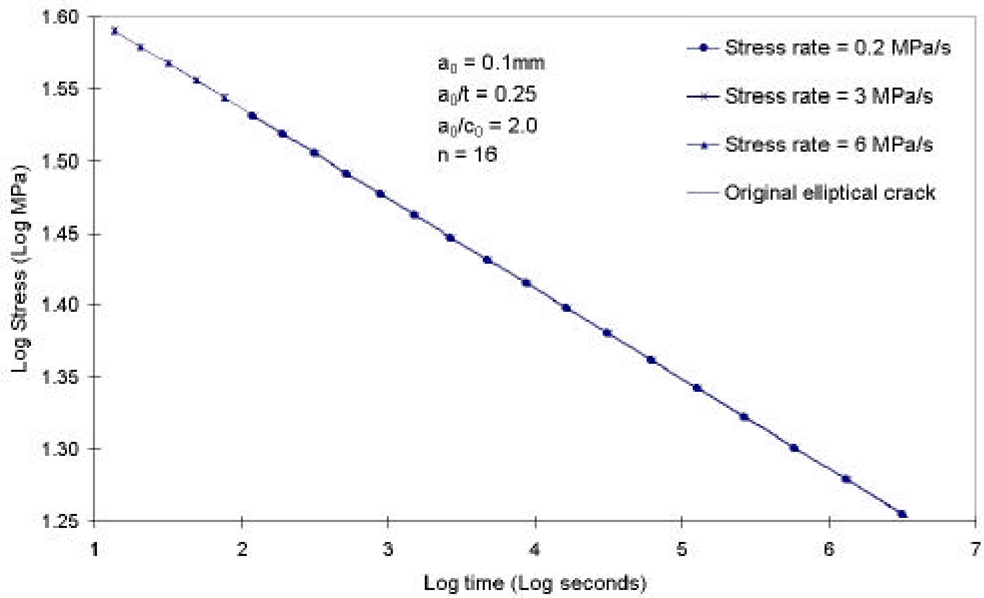

Figure 3.12 Static fatigue plots for crack with initial size based on different stressing rates

3.7 Effect of n on design

In a similar way to the variation in thickness, the variation in n results in different failure stresses, even though the cracks still propagate to an aspect ratio of 1. Typical values for n range from 12 to 20. Previous results given in this chapter have been for n=16. Figure 3.13 shows the percentage errors between the times to failure for the design model and for the original crack for a range of values of n. For a high n there is very little error between the elliptical crack and the circular design equivalent since the high n accentuates the difference in crack speeds for different stress intensity factors. Errors of less than 0.1% are easily achievable if n is 20. Decreasing n reduces the accuracy. This is demonstrated by the larger scatter in Figure 3.13. For the lower limit of 12 for n there is an error of roughly 5% in some cases, which is still acceptable. The lack of smoothness in the curves of Figure 3.13 is a result of the numerical modelling.

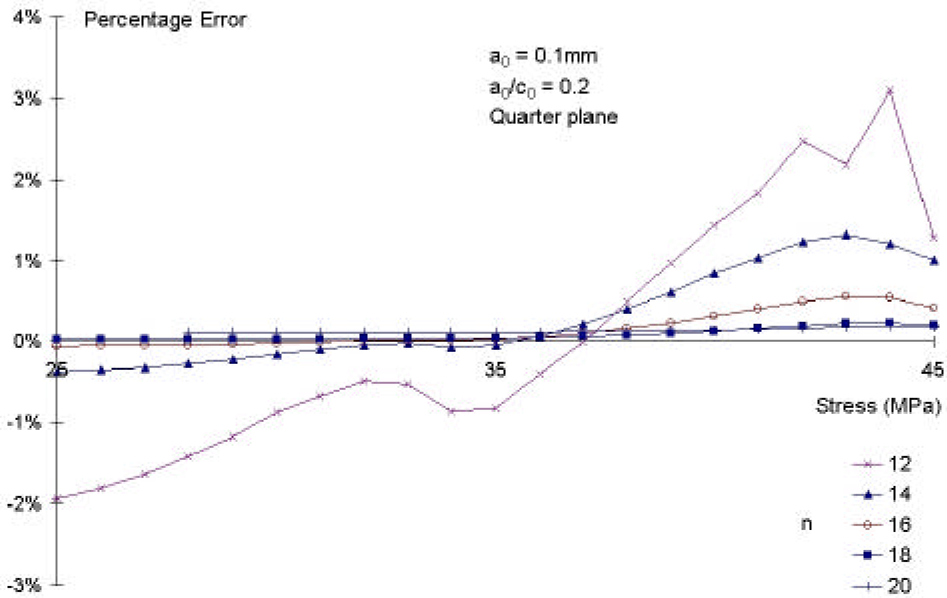

Figure 3.13 Percentage error for various values of *n*

3.8 Subcritical threshold

It has been noted that an asymmetrical crack has different stress intensity factors at each end. Since the design crack is an "average" of this crack, the stress intensity factor in this circular equivalent will probably be between the values at each end of the original crack (although for large ratios of *a/t* this may not always be the case). There is an implication here that the modelled crack will start growing at a different stress to its design crack equivalent. It is important to investigate this problem, as it may lead to the designer assuming safety below the threshold stress intensity factor when in fact the crack is growing, and therefore heading towards failure.

Figure 3.14 shows the percentage error between the stress at which the original elliptical crack would start growing compared to that of its circular equivalent. The results are given for a range of aspect and crack size to thickness ratios. Trends between the plots are not easily visible as there is not necessarily a dimensionless constant common between them. However, it can be see that the errors are small, and all less than 10%. It is suggested that in design the capacity reduction factor for threshold stress intensity factor (ϕ, from equation (2.8)) be scaled down by this margin, in addition to allowing for uncertainty in measurement.

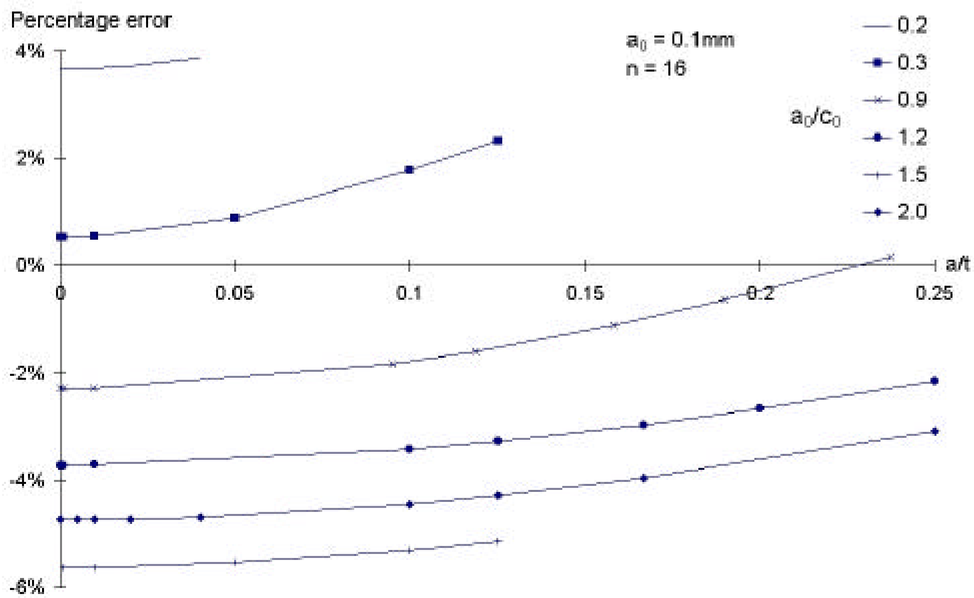

Figure 3.14 Error between subcritical threshold stress for elliptical and equivalent circular cracks

Chapter 4

Compression Loading of Glass

4.1 Introduction

The compressive strength of glass is rarely mentioned in the literature. Usually it is stated that the compressive strength is very high and unlikely to be exceeded in structural design applications. However, as the uses of structural glass become more varied, the compressive requirements on glass increase. In particular, as glass columns become more popular and the loads they carry increase, it will be essential to have a clear understanding of the compression capacity of glass. In this chapter an attempt is made to understand compressive failure of glass and then incorporate it into the Crack Size Design method outlined in Chapter 2. Again it is edge cracks which are of interest, as these are generally critical in structural glass design.

The problem of compression cracking in infinite planes of brittle material has been well researched in the material sciences. In the experiments of Hoek & Bieniawski (1965) plates of glass with initial central macroscopic cracks were loaded in biaxial compression. It was found that standard cracking patterns developed, as shown in Figure 4.1. "Wing cracks" develop from the end of the initial crack and grow to align themselves parallel to the direction of maximum compression. In contrast to cracks in far field tension zones, compression cracks do not necessarily lead to sudden failure. Once a crack has grown to a certain extent in a given compressive stress field, it stops and requires a variation in the applied stress to cause it to grow further. Hence, even though a given load may lead to propagation of individual cracks, it need not lead to global failure of the member. This behaviour under compressive loading has been observed by many experimenters, such as Hoek & Bieniawski (1965), Brace & Bombolakis (1963), Nemat-Nasser & Horii (1982) and Horii & Nemat-Nasser (1986).

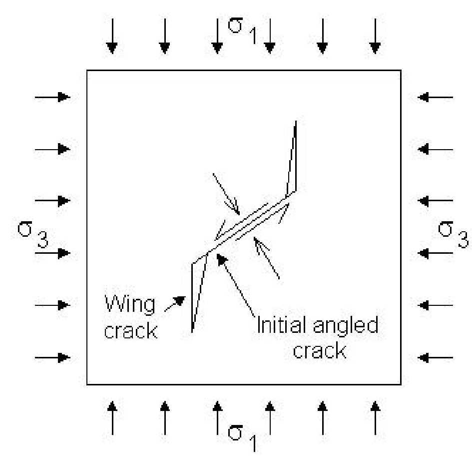

Fig 4.1. Crack pattern due to compression loading where $s_1 > s_3$

The initiation of wing cracks has been explained through fracture mechanical principles (Asbhy & Hallam (1986), Vaughan (1998)). Prior to propagation there is a mode II stress intensity factor at the tip of the initiating crack. This is a result of the shearing actions across the crack, as shown in Figure 4.1. Since the applied stress field is compressive everywhere, the crack is closed along its length, and therefore there is no mode I stress intensity factor at the crack tip. The singular stress field for a mode II stress intensity factor is given in Figure 4.2. It can be seen that the hoop stress, s_{qq}, is positive for $0 \leq q \leq 180$. It is this tension which leads to the formation of the wing crack. The tensile stresses cause a mode I stress intensity factor to develop on an infinitesimally small wing crack located in such a field. A number of authors (Asbhy & Hallam (1986), Vaughan (1998)) have quantified the relationship between the initiating mode II stress intensity factor, K_{II}, and the resulting mode I stress intensity factor on an exceedingly small wing crack, K_I^*, as follows

$$K_I^* = \frac{2}{\sqrt{3}} K_{II} \tag{4.1}$$

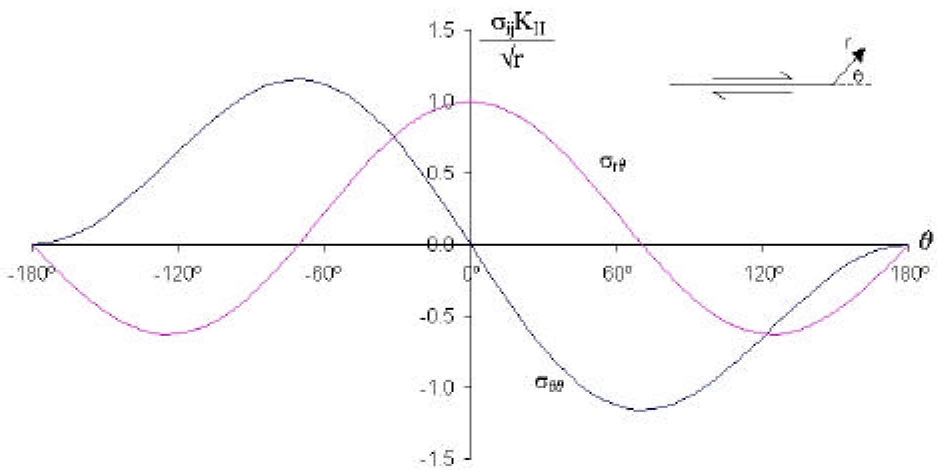

Figure 4.2 Singular stress field for a mode II stress intensity factor

In his experiments on tubular glass columns, Wren (1998) found that the crushing load of glass is widely variable. This can be explained through an understanding of the compressive crack growth mechanisms, as shown in Figure 4.1. When a crack grows under compression, it reaches a certain length, and then arrests. If this crack happens to be close to another crack, which has also grown, then it is possible that the two will connect, forming a larger crack, which is subsequently weaker and may grow under the given compression conditions. Fig 4.3 shows an experimental simulation of such behaviour, from Horii & Nemat-Nasser (1986).

Various authors, such as Hoek & Bieniawski (1965), Nemat-Nasser & Horii (1982), Horii & Nemat-Nasser (1986), and Ashby & Hallam (1986), have shown that this mechanism of inter-connecting wing cracks results in the variable ultimate compressive strength of a brittle member. Although many of the experiments were conducted on glass plates, the practical application was directed at failure in brittle rock. The results and behaviour for glass found in the experiments agree with the practical outcomes for rock.

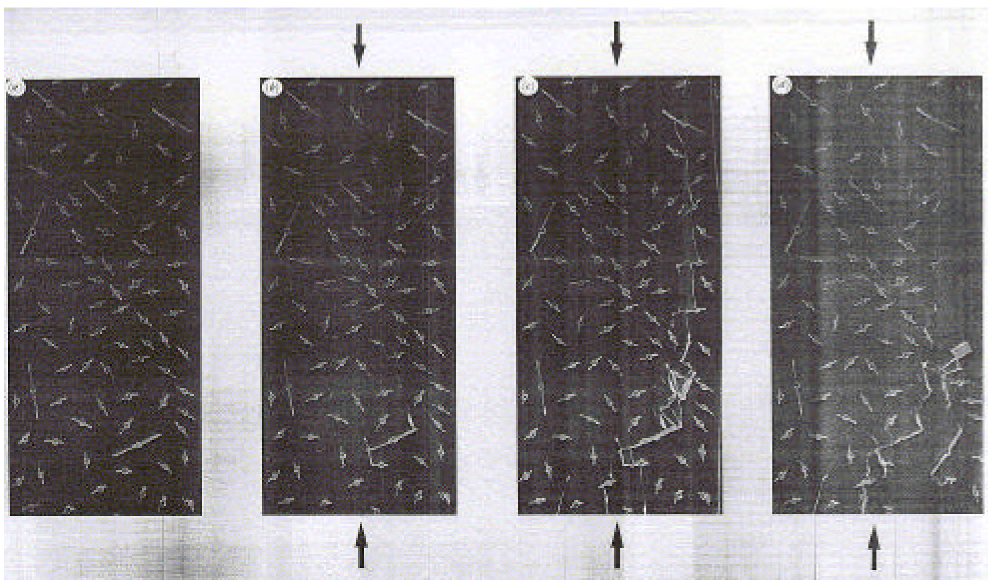

Fig 4.3 Crack growth leading to global failure as cracks combine

The work discussed above shows that failure of a brittle material in a bulk compressive field is both possible, observable and describable. However, all published studies have focused on cracks in an infinite plane. In this chapter the case of an edge crack in a uniform compressive field is investigated, as shown in Figure 4.4. This has direct relevance to a glass column whose largest cracks are located along its edges, due to edge grinding processes, as described in Chapter 2.

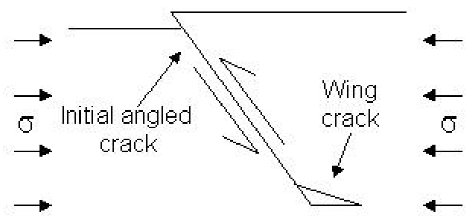

Figure 4.4 Inclined edge crack under compressive loading

4.2 Determination of the mode II stress intensity factors for an inclined edge crack in a compressive field

The initiation of a wing crack is strongly dependent on the mode II stress intensity factor at a crack tip. Therefore, in this section, K_{II} for an edge crack in a compressive field is investigated. The solution is capable of dealing with the case where the crack is at a shallow angle to the surface; a notoriously difficult problem to solve accurately. The method developed here produces an accurate solution in a numerically efficient manner, and has other practical applications, for example to the solution of squat defects in rail-heads.

For brevity, only uniform far field compression will be considered in the formulation. However, the technique is also appropriate for a varying stress field, and shall be applied accordingly in subsequent chapters. The solution is two dimensional in nature and valid for both plane stress and strain.

4.2.1 Formulation

Figure 4.5 shows the geometry of the problem being considered: a half plane of elastic material containing a single edge crack of length a, inclined at an angle θ to the surface normal. The coefficient of friction between the crack faces is f.

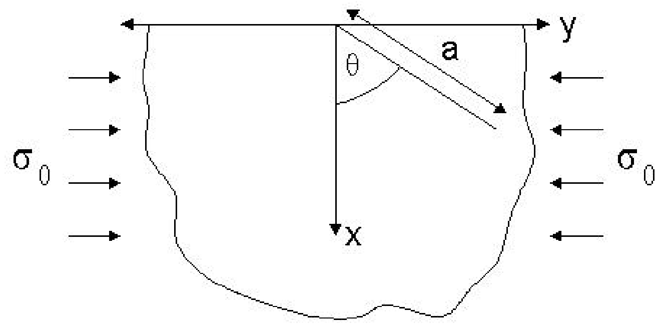

Figure 4.5 The geometry being considered

The solution is based on the distributed dislocation method (see, for example, Nowell & Hills (1987) or Hills *et al.* (1996)). The fundamental strategy is to determine the stress field along the line of the crack, in its absence, and to introduce dislocations to relieve these stresses as appropriate to simulate the presence of the crack. Here, because the crack is closed throughout its length, the direct traction (compression) is sustained everywhere, and the perturbation provided by the dislocations needs only to permit a shear displacement between the crack faces. Hence only local 'glide' dislocations are needed.

4.2.1.1 Preliminaries

A far-field bulk compression, of magnitude σ_0, generates tractions everywhere along the line of the crack, in its absence, of

$$\sigma_N / |\sigma_0| = -\cos^2\theta \qquad (4.2a)$$

$$\sigma_S / |\sigma_0| = -\sin\theta \cos\theta \qquad (4.2b)$$

where σ_S and σ_N are the shear and normal stresses respectively, expressed in the local coordinate set of the crack (see Figure 4.6). The strategy followed here is to distribute strain nuclei, in the form of dislocations, along the line of the crack, so as to restore the Coulomb friction law, imposed in a point-wise sense. That is, a slip displacement is permitted between the two crack faces, such that, at each point, $|s_S/s_N| = f$, where f is the coefficient of friction. In order to do this, the stress state expressed in a coordinate set coincident with the crack orientation, due to an edge dislocation whose Burgers vector also lies in the local slip direction is required, Figure 4.6. The stress state expressed in the global coordinate set, due to a dislocation whose Burgers vectors are also expressed in the global set was given in Nowell & Hills (1987). It is then necessary to resolve the Burgers vector and transform the traction components of stress into local coordinates. In this way we define a set of functions, $G_{\hat{i}\hat{y}}(\hat{x},\hat{c})$, relating the stress state at point $(\hat{x},0)$ to the strength of a dislocation, $b_{\hat{x}}(\hat{c})$, shown in Figure 4.6.

$$\tilde{s}_{\hat{i}\hat{y}} = \frac{m}{p\,(k+1)} b_{\hat{x}}(\hat{c}) G_{\hat{i}\hat{y}}(\hat{x},\hat{c}) \tag{4.3}$$

where m = modulus of rigidity

$k = (3\text{-}4n)$ in plane strain

n = Poisson's ratio

$i = \hat{x}, \hat{y}$

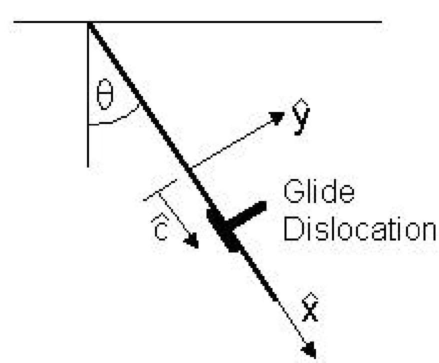

Figure 4.6 Dislocation arrangement

4.2.2 Solution technique

It is now possible to write down the value of the shear traction, *S(x)*, at any point along the crack. This has a contribution from the bilateral stress field (equation (4.2)), together with the effect of a distribution of glide dislocations, of unknown density, $B_{\hat{x}}(u)$, and may be represented by the following integral:

$$S(x) = s_S(x) + \int_{-a/2}^{a/2} B_{\hat{x}}(u) G_{\hat{x}\hat{y}}(\hat{x}, u) du \tag{4.4}$$

where $B_{\hat{x}}(u) = \dfrac{\mathrm{d}b_{\hat{x}}}{\mathrm{d}u}$

Similarly, the direct traction, *N(x)*, may also be written down as the sum of the bilateral stress field, together with a contribution from the dislocations, i.e.

$$N(x) = s_N(x) + \int_{-a/2}^{a/2} B_{\hat{x}}(u) G_{\hat{y}\hat{y}}(\hat{x}, u) du \,. \tag{4.5}$$

It can then be seen that if the crack is slipping at every point along its length, the direct and shear tractions are related by

$$S(x) = \pm f \left| N(x) \right| . \tag{4.5a}$$

Substituting the two integrals into this equation then leads to the following integral equation for the unknown dislocation density, $B_{\hat{x}}(u)$

$$\int_{-a/2}^{a/2} B_{\hat{x}}(u)\left(G_{\hat{x}\hat{y}}(\hat{x},u) \pm fG_{\hat{y}\hat{y}}(\hat{x},u)\right)du = -\left(s_S(\hat{x}) \mp fs_N(\hat{x})\right). \tag{4.6}$$

4.2.3 Numerical Solution

The typical way of solving equation (4.6) is to use the standard Gauss-Chebyshev numerical quadrature (Nowell & Hills, 1987). Strictly speaking, this approach is valid only when the integral has a true Cauchy kernel. Here, it is of the generalised type and this has an important effect on the convergence of the solution. In the case of an open, surface breaking crack, the Gauss-Chebyshev quadrature forces the dislocation density at the crack mouth to be zero, and hence the crack faces to remain parallel, which is an artificial constraint. The problem is particularly severe, and affects the quality of the solution, when the crack is at a very shallow angle to the surface. A similar phenomenon is experienced with shearing displacements. A modification to the quadrature, developed by Dewynne *et al.* (1992), was employed. This method allows for a finite value of the Burgers vector at the surface. This is achieved by introducing an additional triangle of Burgers vectors over the crack, whose value is zero at the crack tip and finite ($B_{\hat{x}}^{-1}$) at the surface.

The details of the procedure adopted are as follows: first, the coordinates are normalised with respect to the crack half length, so that the interval of integration of equation (4.6) becomes [-1,1]. Since the dislocation density is bounded and finite at the surface and singular at the crack tip, the dislocation density $B_{\hat{x}}(u)$ can be expressed as the product of an unknown bounded function, $f(u)$, and a fundamental function (Erdogan *et al.*, 1973) together with a term to account for the triangle of Burgers vectors, thus

$$B_{\hat{x}}(u) = f(u)(1-u)^{-1/2}(1+u)^{1/2} + B_{\hat{x}}^{-1} g(u) \quad \text{for } -1 \le u \le 1 \tag{4.7}$$

where

$$g(u) = \frac{1}{2}(1-u)\ .$$

Applying the integration scheme of Erdogan *et al.* (1973) to equation (4.6) leads to the following set of simultaneous equations.

$$\sum_{j=1}^{N} \frac{2p\,(1+u_j)}{2N+1} K(v_k, u_j) f(u_j) + G(v_k) B_{\hat{x}}^{-1} = -\frac{p\,(k+1)}{m}\left[s_S(v_k) \mp \left| f s_N(v_k) \right|\right] \tag{4.8}$$

where

$$u_j = \cos\left(\frac{2j-1}{2N+1}p\right), v_k = \cos\left(\frac{2k}{2N+1}p\right) \qquad \text{for } k=1,..,N$$

$$K(v_k, u_j) = G_{\hat{x}\hat{y}}(\hat{x}, u) \pm f G_{\hat{y}\hat{y}}(\hat{x}, u)$$

$$G(v) = \int_{-1}^{1} g(u) K(v,u)\, du \tag{4.9}$$

Note that for uniform far field compression, $s_S(v_k)$ and $s_N(v_k)$ are constants, as defined by equation (4.2). However, varying stress fields can be easily incorporated into this solution method by evaluating the stresses at the points v_k.

The $\mp$ sign is incorporated into equation (4.8) as q, Figure 4.5, may be of either sign, and the magnitude of the shear traction is always reduced by friction. Additionally, the coefficient of friction must not be so high that adhesion occurs.

The set of simultaneous equations described in equation (4.8) consists of *N+1* unknowns in *N* equations. The final equation is given by Dewynne *et al*. (1992), who show that the consistency condition of $f(-1) = 0$ is required for this solution method. The quantity $f(-1)$ is evaluated using Krenk's formula (Krenk, 1975).

$$f(-1) = \sum_{j=1}^{N} f(u_{n+1-j}) \sin\left(\frac{2N-1}{2N+1} pj\right) \Big/ \sin\left(\frac{p}{2N+1} j\right) \tag{4.10}$$

The set of simultaneous equations is easily solved using computer library routines. Upon solution the stress intensity factor may be found from the following (Nowell & Hills, 1987):

$$K_{II} = 2\sqrt{2}\sqrt{pa}\,\frac{m}{k+1} f(1) \tag{4.11}$$

where

$$f(1) = \sum_{j=1}^{N} f(u_j) \sin\left(\frac{2N-1}{2N+1} pj\right) \Big/ \sin\left(\frac{p}{2N+1} j\right). \tag{4.12}$$

4.2.4 Results for an edge crack in a uniform compressive field

Figure 4.7 displays the mode II stress intensity factor for a wide range of coefficients of friction and for crack inclinations from 0 to 90 . Values were obtained up to $q = 85^\circ$, with N set to 250. The shape of the frictionless curve (*f=0*) mirrors the behaviour of s_S, having a maximum at about $q = 45^\circ$. Note, however, that for finite friction the K_{II} maximum is slightly offset from 45 due to the presence of the free surface and its effect on the dislocations.

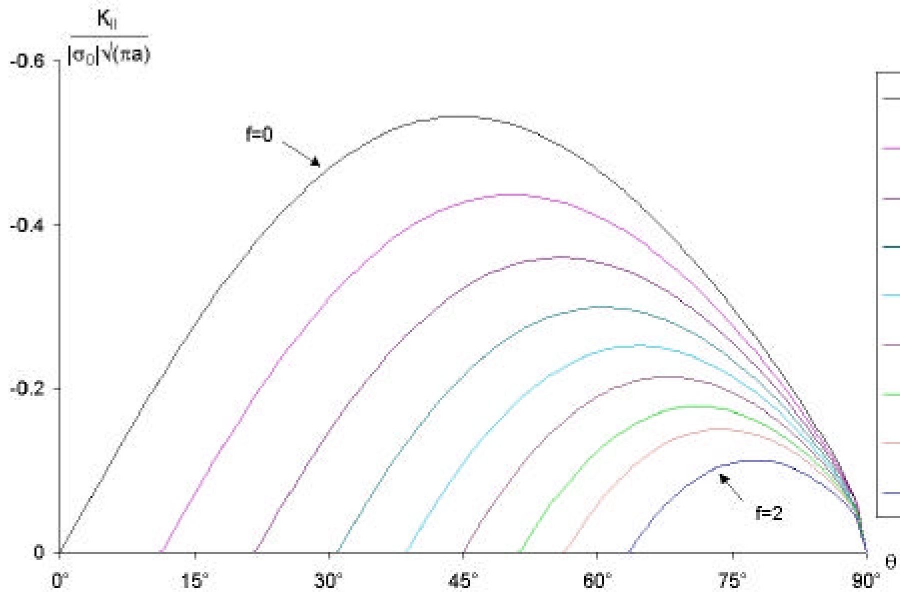

Figure 4.7 K_{II} versus θ for various coefficients of friction, *f*

Friction on the crack faces reduces the resultant shearing traction, which drives the magnitude of the mode II stress intensity factor. Also, for low inclinations the normal stress is high compared to the nominal shear stress, so that the frictional reduction of the shearing stress is sufficient to annul it completely. The crack therefore "sticks" for low inclinations, giving $K_{II} = 0$.

The results of Figure 4.7 may be summarised in a different way. Figure 4.8 shows the angles below which there is no K_{II}, and the angles where K_{II} is a maximum, for a given coefficient of friction. Note that the line defining the conditions where K_{II} vanishes may also be obtained from the bilateral stresses. It is defined by the points where $fs = t$, ie.

$$f_{\min} = \frac{t}{s} = \frac{-\sin q \, \cos q}{-\cos^2 q} = \tan q \ . \tag{4.13}$$

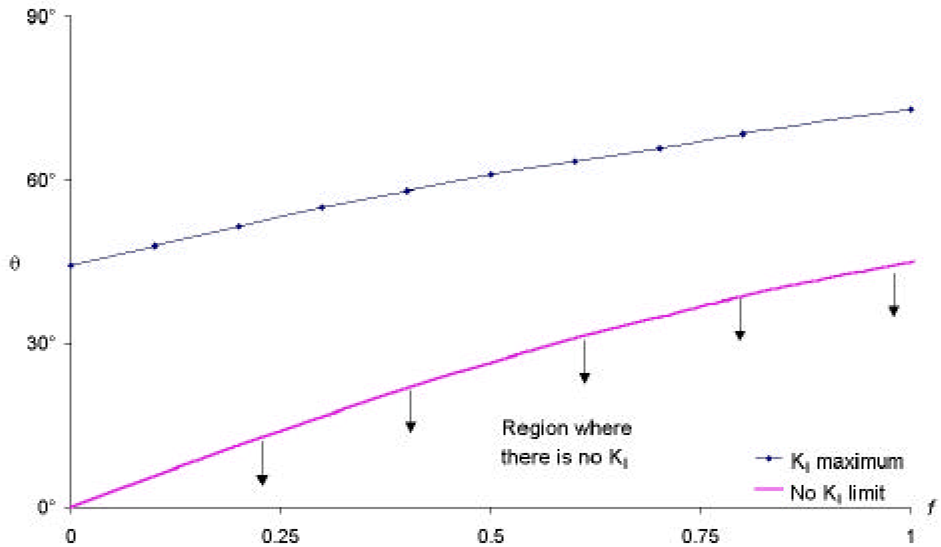

Figure 4.8 Conditions for $K_{II} \rightarrow 0$ and $K_{II}^{\max}$ as a function of inclination angles and the coefficient of friction

Figure 4.9 explicitly gives the maximum K_{II} that can be expected for a given coefficient of friction.

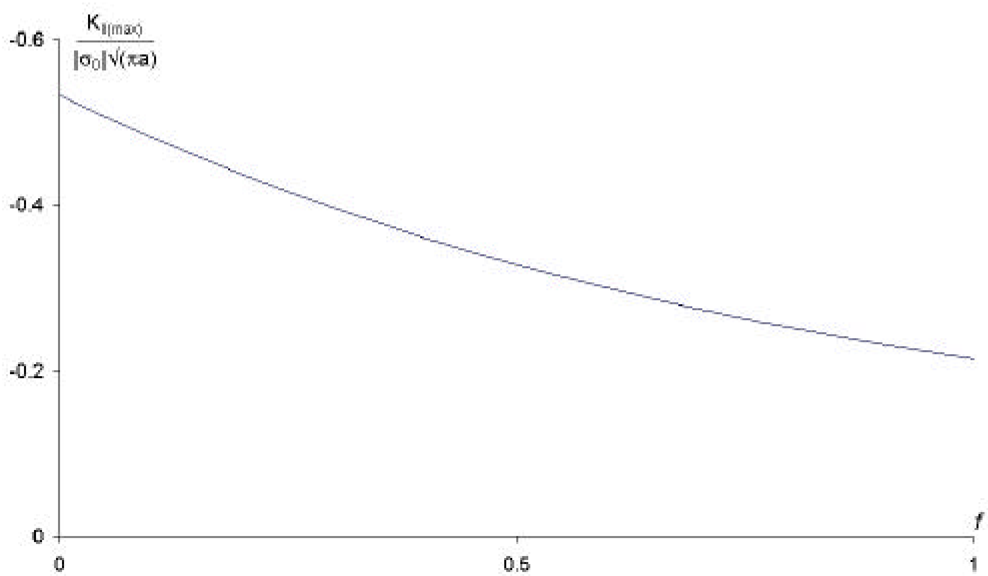

Figure 4.9 Maximum K_{II} versus coefficient of friction

4.3 Wing crack growth in a bulk compressive stress field

In section 4.1 the mechanism of wing crack propagation was introduced. It was shown that wing crack initiation was dominated by the magnitude of the mode II stress intensity factor at the tip of the pre-existing crack (ie at the point which becomes the kink). In section 4.2 this stress intensity factor was evaluated for an edge crack in a uniform compressive field. In the current section the propagation of the wing crack is investigated analytically. Similar methods to those used in section 4.2 are employed here to calculate the stress intensity factors at the end of the wing crack. Issues of propagation are then considered as the wing crack length increases.

In this section the wing crack is considered to be straight. Experimental work (for example, Hoek & Bieniawski (1965), Brace & Bombolakis (1963), Nemat-Nasser & Horii (1982) and Horii & Nemat-Nasser (1986)) shows that the wing crack curves as it extends. However, for small wing crack lengths the results presented here will be realistic. Also, the emphasis in this analysis is to determine *whether* the half plane edge crack will propagate in a similar way to the infinite plane crack, rather than *how* this occurs for long wing cracks. The assumption of a straight wing crack also simplifies the mathematical formulation, which is appropriate as this chapter constitutes the first attempt at a solution for this half plane edge crack formulation in the literature.

4.3.1 Formulation

The geometry of the problem is defined in Figure 4.10. The pre-existing crack (segment 1) is present in the half plane $x \geq 0$, and is inclined at an angle θ_1 to the surface normal. The wing crack (segment 2) is inclined at θ_2 to the surface normal. The segments are of lengths a_1 and a_2 respectively.

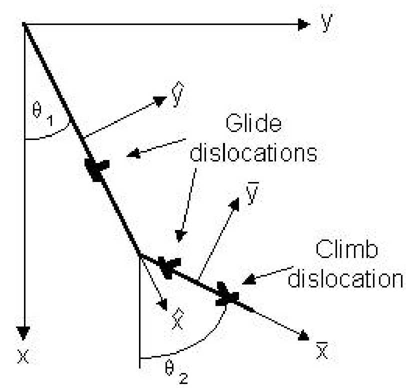

Figure 4.10 Details of the kinked crack geometry

As the main crack is assumed to be closed throughout its length, only glide dislocations having a Burgers vector $b_{\hat{x}}$ are introduced on segment 1 to relieve the shear stresses. In the absence of segment 2 the segment 1 glide dislocations will generate a mode II stress intensity factor at the segment 1 tip (ie at what becomes the kink). Now segment 2 is introduced which is subject to both shear and tensile stresses, as discussed earlier. Therefore glide and climb dislocations $(b_{\hat{x}}, b_{\hat{y}})$ are introduced along segment 2 to relieve both shear and direct tractions.

Further details of the orientation of the dislocations are given in Figure 4.10. The segment 1 glide dislocations *must* be oriented at θ_1, so that no opening displacements are induced. For ease of calculation, the dislocations in segment 2 are also oriented at this same inclination, so that continuity conditions at the kink may be evaluated in the one axis set. Note that, in the local coordinate set of segment 2 $(\bar{x}, \bar{y})$, each dislocation will therefore have both glide and climb components.

It is now necessary to define the stress state, in either local coordinate set $((\hat{x}, \hat{y}), (\bar{x}, \bar{y}))$, resulting from the dislocations inclined at θ_1. The stress state expressed in the global coordinate set *(x,y)*, due to a dislocation whose Burgers vectors are also expressed in the global set was given in Nowell & Hills (1987). The Burgers vector and traction components of stress are then transformed into the local coordinates of segment 1, $(\hat{x}, \hat{y})$. In this way we define a set of functions, $G_{\hat{i}\hat{j}\hat{k}}(x, y, c)$, relating the stress state, $\tilde{s}_{\hat{i}\hat{j}}$, at point (x, y) to the strength of the dislocations, $b_{\hat{x}}(c)$ and $b_{\hat{y}}(c)$, giving

$$\tilde{s}_{\hat{i}\hat{j}\hat{x}} = \frac{m}{p(k+1)} b_{\hat{x}}(c) G_{\hat{i}\hat{j}\hat{x}}(x, y, c)$$
$$\tilde{s}_{\hat{i}\hat{j}\hat{y}} = \frac{m}{p(k+1)} b_{\hat{y}}(c) G_{\hat{i}\hat{j}\hat{y}}(x, y, c) \qquad (4.14)$$

where $i,j = x$ or y

m = modulus of rigidity

$k = (3\text{-}4n)$ in plane strain

n = Poisson's ratio

The stress state in the segment 2 coordinate set, $\tilde{s}_{\bar{i}\bar{j}}$, may be easily determined through a rotation of the stresses already expressed in the segment 1 inclination from equation (4.14).

Note that all points of interest in this solution lie along the lines of one of the crack segments. Hence, the point (x, y) may be described simply by the local "x" coordinate, ie $\hat{x}$ or $\bar{x}$. Similarly, the dislocations lie on the lines of either segment 1 or 2, and are therefore specified simply through the coordinates $\hat{c}_1$ or $\bar{c}_2$. The procedure outlined above allows the calculation of the stresses resulting from a glide or climb dislocation inclined at q_1 to the vertical axis, expressed in the coordinate set of either segment of the crack. An influence function, K, is then defined which gives the normal (N) or shear (S) stress at a point on segment 1 or 2, resulting from a glide ($\hat{x}$) or climb ($\hat{y}$) dislocation on either segment, for a unit dislocation strength. For example, $K^{N1}_{x2}(\hat{x}, \bar{c}_2)$ is the normal stress on a specified point in segment 1 resulting from a glide dislocation in segment 2 of unit strength.

For a continuous distribution of dislocations, of densities $B_{\hat{x}1}$, $B_{\hat{x}2}$ and $B_{\hat{y}2}$, the shear (S) and normal (N) tractions on the crack segments are:

$$S_1(\hat{x}) = s_{\hat{x}\hat{y}}(\hat{x}) + l\begin{Bmatrix} \int_{-a_1/2}^{a_1/2} B_{\hat{x}1}(\hat{c}_1)K^{S1}_{\hat{x}1}(\hat{x},\hat{c}_1)d\hat{c}_1 + \\ \int_{-a_2/2}^{a_2/2} B_{\hat{x}2}(\bar{c}_2)K^{S1}_{\hat{x}2}(\hat{x},\bar{c}_2)d\bar{c}_2 + \int_{-a_2/2}^{a_2/2} B_{\hat{y}2}(\bar{c}_2)K^{S1}_{\hat{y}2}(\hat{x},\bar{c}_2)d\bar{c}_2 \end{Bmatrix} \tag{4.15}$$

$$S_2(\bar{x}) = s_{\overline{xy}}(\bar{x}) + l\begin{Bmatrix} \int_{-a_1/2}^{a_1/2} B_{\hat{x}1}(\hat{c}_1)K^{S2}_{\hat{x}1}(\bar{x},\hat{c}_1)d\hat{c}_1 + \\ \int_{-a_2/2}^{a_2/2} B_{\hat{x}2}(\bar{c}_2)K^{S2}_{\hat{x}2}(\bar{x},\bar{c}_2)dc_2 + \int_{-a_2/2}^{a_2/2} B_{\hat{y}2}(\bar{c}_2)K^{S2}_{\hat{y}2}(\bar{x},\bar{c}_2)d\bar{c}_2 \end{Bmatrix} \tag{4.16}$$

$$N_2(\bar{x}) = s_{\overline{yy}}(\bar{x}) + l\begin{Bmatrix} \int_{-a_1/2}^{a_1/2} B_{\hat{x}1}(\hat{c}_1)K^{N2}_{\hat{x}1}(\bar{x},\hat{c}_1)d\hat{c}_1 + \\ \int_{-a_2/2}^{a_2/2} B_{\hat{x}2}(\bar{c}_2)K^{N2}_{\hat{x}2}(\bar{x},\bar{c}_2)d\bar{c}_2 + \int_{-a_2/2}^{a_2/2} B_{\hat{y}2}(\bar{c}_2)K^{N2}_{\hat{y}2}(\bar{x},\bar{c}_2)d\bar{c}_2 \end{Bmatrix}$$

(4.17)

where $B_{\hat{x}1}(\hat{c}_1) = \dfrac{\mathrm{d}b_{\hat{x}1}}{\mathrm{d}\hat{x}}$

and $B_{\hat{i}2}(\bar{c}_2) = \dfrac{\mathrm{d}b_{\hat{i}2}}{\mathrm{d}\bar{x}}$

$\hat{i} = \hat{x}, \hat{y}$

The problem requires that segment 1 be cleared of shear tractions, and segment 2 be cleared of both shear and normal tractions.

$$S_1(\hat{x}) = 0 \text{ for } -a_1/2 \le \hat{x} \le a_1/2 \tag{4.18}$$

$$S_2(\bar{x}) = N_2(\bar{x}) = 0 \text{ for } -a_2/2 \le \bar{x} \le a_2/2 \tag{4.19}$$

Conditions (4.18) and (4.19) together with equations (4.15), (4.16) and (4.17) give three simultaneous integral equations in the unknown dislocation densities. These must be solved numerically. First, the coordinates are normalised with respect to the segment lengths, so that the intervals of integration become [-1,1].

$$u_i = 2c_i / a_i \tag{4.20a}$$

$$v_i = 2x_i / a_i \tag{4.20b}$$

where $i = 1,2$

The integral equations are now given by

$$l\begin{Bmatrix}\int_{-1}^{1} B_{\hat{x}1}(u_1)K_{\hat{x}1}^{S1}(v_1,u_1)du_1 + \\ \int_{-1}^{1} B_{\hat{x}2}(u_2)K_{\hat{x}2}^{S1}(v_1,u_2)du_2 + \int_{-1}^{1} B_{\hat{y}2}(u_2)K_{\hat{y}2}^{S1}(v_1,u_2)du_2\end{Bmatrix} = -s_{\hat{x}\hat{y}}(v_1) \tag{4.21}$$

$$l\begin{Bmatrix}\int_{-1}^{1} B_{\hat{x}1}(u_1)K_{\hat{x}1}^{S2}(v_1,u_1)du_1 + \\ \int_{-1}^{1} B_{\hat{x}2}(u_2)K_{\hat{x}2}^{S2}(v_1,u_2)du_2 + \int_{-1}^{1} B_{\hat{y}2}(u_2)K_{\hat{y}2}^{S2}(v_1,u_2)du_2\end{Bmatrix} = -s_{\overline{xy}}(v_2) \tag{4.22}$$

$$l\begin{Bmatrix}\int_{-1}^{1} B_{\hat{x}1}(u_1)K_{\hat{x}1}^{N2}(v_1,u_1)du_1 + \\ \int_{-1}^{1} B_{\hat{x}2}(u_2)K_{\hat{x}2}^{N2}(v_1,u_2)du_2 + \int_{-1}^{1} B_{\hat{y}2}(u_2)K_{\hat{y}2}^{N2}(v_1,u_2)du_2\end{Bmatrix} = -s_{\overline{yy}}(v_2) \tag{4.23}$$

4.3.2 Solution technique

The solution technique follows, with some modification, that of Yingzhi & Hills (1990), who investigated a kinked crack which was open along both segments. A numerical integration scheme is employed in which the unknown Burgers vector distributions, $B_{\hat{i}j}$, are expressed as products of unknown functions, $f_{\hat{i}j}$, and fundamental functions. The forms of the fundamental functions are determined by the combination of bounded or singular conditions at the crack segment ends. The kinked crack may be considered as the sum of an edge and a buried crack, with continuity conditions at the kink: the Burgers vectors for segment 1 should be bounded at the surface and singular at the kink, while the segment 2 distributions should be singular at both ends. The traditional formulation for such a case is,

$$B_{\hat{x}1} = f_{\hat{x}1}(u_{G1})(1-u_{G1})^{-1/2}(1+u_{G1})^{1/2} \tag{4.24}$$

$$B_{\hat{x}2} = f_{\hat{x}2}(u_{G2})(1-u_{G2}^2)^{-1/2} \tag{4.25}$$

$$B_{\hat{y}2} = f_{\hat{y}2}(u_{C2})(1-u_{C2}^2)^{-1/2} \tag{4.26}$$

where the subscript C or G indicates climb or glide dislocations, and a subscript of 1 indicates the dimension along the $\hat{x}$ axis, and 2 along the $\bar{x}$ axis.

Equation (4.24) implies that at the crack mouth ($u_{G1} = -1$), $B_{\hat{x}1} = 0$. It has been shown previously by Dewynne *et al.* (1992), that this inherent assumption is not valid, and is particularly troublesome as the crack inclination approaches 90º. The rigorous condition is for the Burgers vector distribution to be bounded and *non*-zero at the crack mouth. To achieve this an additional term is introduced into equation (4.24) which produces a finite value of $B_{\hat{x}1}$ at the crack mouth while tending to zero at the kink. Dewynne *et al.* (1992) showed that a triangular distribution was acceptable for this purpose. Hence, equation (4.24) may be re-written as

$$B_{\hat{x}1} = B_{-1}g(u_{G1}) + f_{\hat{x}1}(u_{G1})(1-u_{G1})^{-1/2}(1+u_{G1})^{1/2} \tag{4.26a}$$

where B_{-1} is an unknown constant

$$g(u) = \frac{1}{2}(1-u)$$

Dewynne also showed that the side condition for the formulation given here is

$$f_{\hat{x}1}(-1) = 0 \tag{4.27}$$

A Gauss-Chebyshev quadrature is used for the numerical integration, as described in detail in Erdogan *et al.* (1973). The integration points are

$$u_{G1i} = \cos\left(\frac{2i-1}{2n+1}p\right) \text{ for i=1,…,n} \tag{4.28a}$$

$$u_{G2i} = u_{C2i} = \cos\left(\frac{2i-1}{2n}p\right) \text{ for i=1,…,n} \tag{4.28b}$$

and the collocation points are given by

$$v_{G1k} = \cos\left(\frac{2k}{2n+1}p\right) \text{ for k=1,…,n} \tag{4.28c}$$

$$v_{G2k} = v_{C2k} = \cos\left(\frac{k}{n}p\right) \text{ for k=1,…,n-1} \tag{4.28d}$$

The discretised integral equations become

$$l\left[\begin{array}{l} \displaystyle\sum_{i=1}^{n}\frac{2p(1+u_{G1i})}{2n+1}K_{\hat{x}1}^{S1}(v_{G1k},u_{G1i})f_{\hat{x}1}(u_{G1i})+\frac{p}{n}K_{\hat{x}2}^{S1}(v_{G1k},u_{G2i})f_{\hat{x}1}(u_{G2i}) \\ \displaystyle +\frac{p}{n}K_{\hat{y}2}^{S1}(v_{G1k},u_{C2i})f_{\hat{x}1}(u_{C2i})+B_{-1}\int_{-1}^{1}g(x)K_{\hat{x}1}^{S1}(v_{G1k},x)dx \end{array}\right] = -s_{\hat{x}\hat{y}}(v_{G1k})$$

for k=1,…,n (4.29)

$$l\left[\begin{array}{l} \displaystyle\sum_{i=1}^{n}\frac{2p(1+u_{G1i})}{2n+1}K_{\hat{x}1}^{S2}(v_{G2k},u_{G1i})f_{\hat{x}1}(u_{G1i})+\frac{p}{n}K_{\hat{x}2}^{S2}(v_{G2k},u_{G2i})f_{\hat{x}1}(u_{G2i}) \\ \displaystyle +\frac{p}{n}K_{\hat{y}2}^{S2}(v_{G2k},u_{C2i})f_{\hat{x}1}(u_{C2i})+B_{-1}\int_{-1}^{1}g(x)K_{\hat{x}1}^{S2}(v_{G2k},x)dx \end{array}\right] = -s_{\overline{xy}}(v_{G2k})$$

for k=1,…,n-1 (4.30)

$$
l\left[\begin{array}{l}\sum_{i=1}^{n}\frac{2p(1+u_{G1i})}{2n+1}K_{\hat{x}1}^{N2}(v_{C2k},u_{G1i})f_{\hat{x}1}(u_{G1i})+\frac{p}{n}K_{\hat{x}2}^{N2}(v_{C2k},u_{G2i})f_{\hat{x}1}(u_{G2i})\\ +\frac{p}{n}K_{\hat{y}2}^{N2}(v_{C2k},u_{C2i})f_{\hat{x}1}(u_{C2i})+B_{-1}\int_{-1}^{1}g(x)K_{\hat{x}1}^{N2}(v_{C2k},x)\,dx\end{array}\right]=-s_{\overline{yy}}(v_{G2k})
$$

for k=1,…,n-1 (4.31)

The right hand sides of the above equations represent the bilateral stress field from equation (4.2). Rapidly varying stress fields, such as those induced by contact loading, may therefore be analysed without any further complexity in calculation.

Equations (4.29) – (4.31) provide *3n-2* equations in *3n+1* unknowns. The side condition of equation (4.27) provides one extra equation. In order to implement it we use Krenk's formula (Krenk, 1975) to evaluate $f_{\hat{x}1}(-1)$, giving

$$
f_{\hat{x}1}(-1)=\sum_{i=1}^{N}f_{\hat{x}1}(u_{n+1-i})\sin\left(\frac{2N-1}{2N+1}pi\right)\Big/\sin\left(\frac{p}{2N+1}i\right) \qquad (4.32)
$$

The two remaining side conditions necessary are obtained from the continuity requirement at the crack kink, illustrated in Figure 4.11. This figure highlights that the predominant displacement at the kink is along the $\hat{x}$ axis. The displacement along the $\hat{y}$ axis at this point is zero. At the crack tip the displacement is also zero, indicating that there should be no net displacement over segment 2 in the $\hat{y}$ direction. This condition is enforced by requiring that

$$
\sum_{i=1}^{n}\frac{p}{n}f_{\hat{y}2}(u_{C2i})=0 \qquad (4.33)
$$

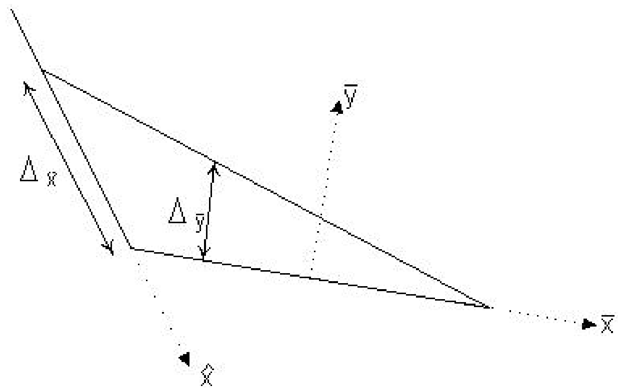

Figure 4.11 Detail of the kink and displacements

Lastly, the *rate of change* of the displacements in the $\hat{x}$ direction is the same in each segment at the kink, and this condition may be enforced in the solution. This rate of change is given by the Burgers vector density, so that

$$\lim(u_{G1} \to 1),\, B_{\hat{x}1}(u_{G1}) = \lim(u_{G2} \to -1),\, B_{\hat{x}2}(u_{G2}) \tag{4.34}$$

$$B_{\hat{x}1} \to f_{\hat{x}1}(1)(1-1)^{-1/2}(1+1)^{1/2} = f_{\hat{x}1}(1)\sqrt{2} \times 0^{-1/2} \tag{4.35a}$$

$$B_{\hat{x}2} \to f_{\hat{x}2}(-1)(1-1)^{-1/2} = f_{\hat{x}2}(1) \times 0^{-1/2} \tag{4.35b}$$

Therefore,

$$\sqrt{2} f_{\hat{x}1}(1) = f_{\hat{x}2}(-1) \tag{4.36}$$

In order to determine $f_{\hat{x}i}$ at the end points, Krenk interpolation is required, as in equation (4.32). For $f_{\hat{x}1}$, where one end is bounded and the other singular,

$$f_{\hat{x}1}(1) = \frac{2}{2n+1} \sum_{i=1}^{n} \cot\left(\frac{2i-1}{2n+1} \frac{p}{2} \right) \sin\left(\frac{n}{2n+1}(2i-1)p \right) f_{\hat{x}1}(u_i) \tag{4.37}$$

When both ends are singular, as for $f_{\hat{x}2}$ and $f_{\hat{y}2}$, then

$$f_{\hat{i}2}(-1) = \frac{1}{n}\sum_{i=1}^{n} f_{\hat{i}2}(u_{n+1-i}) \sin\left(\frac{2n-1}{4n}(2i-1)p\right) \Big/ \sin\left(\frac{2i-1}{4n}p\right) \qquad (4.38a)$$

$$f_{\hat{i}2}(1) = \frac{1}{n}\sum_{i=1}^{n} f_{\hat{i}2}(u_i) \sin\left(\frac{2n-1}{4n}(2i-1)p\right) \Big/ \sin\left(\frac{2i-1}{4n}p\right) \qquad (4.38b)$$

There are now *3n+1* equations in *3n+1* unknowns, allowing solution. Upon solving the stress intensity factors are easily determined, as given in Yingzhi & Hills (1990).

$$\hat{K}_I = \frac{2m}{1+k}\sqrt{pa_2}\, f_{\hat{y}2}(1) \qquad (4.39a)$$

$$\hat{K}_{II} = \frac{2m}{1+k}\sqrt{pa_2}\, f_{\hat{x}2}(1) \qquad (4.39b)$$

Equations (4.39a) and (4.39b) give stress intensity factors oriented with respect to segment 1, each of which provides a mixed contribution to the opening and shearing loading of segment 2. It is more appropriate to express them in the coordinate set of segment 2, as given by the vector transformation of equations (4.40a) and (4.40b), so that they have their conventional meaning.

$$\overline{K}_I = \cos(q_2 - q_1)\hat{K}_I + \sin(q_2 - q_1)\hat{K}_{II} \qquad (4.40a)$$

$$\overline{K}_{II} = -\sin(q_2 - q_1)\hat{K}_I + \cos(q_2 - q_1)\hat{K}_{II} \qquad (4.40b)$$

4.3.3 Results for a kinked crack in a uniform compressive field

The results for a kinked crack located in a uniform compression field, as shown in Figure 4.4, are presented first. Figure 4.12 shows the variation of K_I and K_{II} at the crack tip as a function of kink angle (θ_2-θ_1). In the cases where a_2 is small, the plots follow the same shape as the direct and shear stress curves for a mode II stress intensity factor singular field, as given in Figure 4.2. This demonstrates that as $a_2 \rightarrow 0$ the wing crack behaviour becomes dominated by the singular mode II stress field present at the tip of segment 1. Very small segment 2 lengths $(a_2/a_1 << 0.01)$ were found to be difficult to compute, due to the steep gradient in the singular field at the end of segment 1. Figure 4.12 also shows that as the wing crack propagates, the mode I stress intensity factor at its tip reduces. This implies that, for further propagation, the magnitude of the applied compressive field would have to be increased. This has been found experimentally for the infinite plane problem.

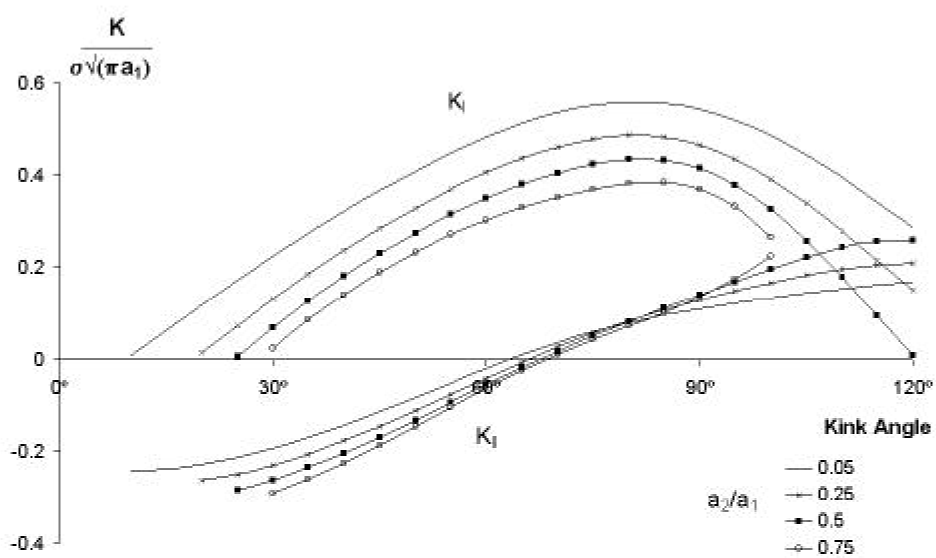

Figure 4.12 Stress intensity factors for a kinked crack in a uniform compression field

The curves in Figure 4.12 terminate when the mode I stress intensity factor falls to zero. This corresponds to the closure of the wing crack at its tip. The formulation presented here cannot take into account closure of segment 2. Figure 4.12 shows that longer cracks are more prone to closure. This is because, as the crack extends, the relative influence of the compressive far field to the local mode II field increases.

By integrating the Burgers vector distribution, the displacements at any point along the crack may be calculated. Figure 4.13 shows a typical displaced shape of the wing crack, confirming the wedge-like opening behaviour predicted.

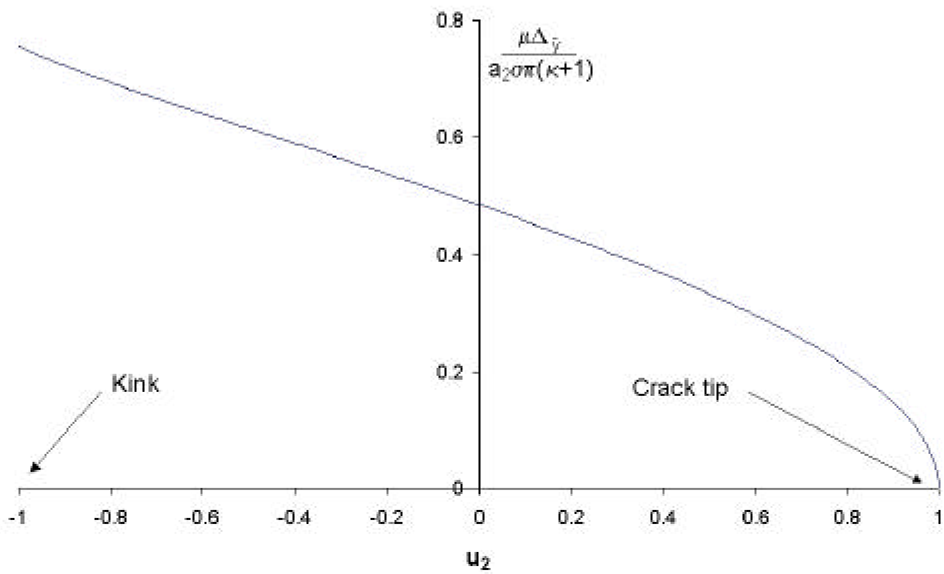

Figure 4.13 Displacements of the wing crack

Each K_I curve of Figure 4.12 has a maximum for a kink angle of approximately 80º. In Figure 4.14 these maxima have been plotted against the segment 2 crack lengths for which they occur. Various sources in the literature (for example, Ashby & Hallam (1986) and Vaughan (1998)) have proposed a theoretical value for K_I as $a_2 \to 0$, given in equation (4.1). This point has been plotted on the graph as the y axis intercept. It can be seen that this point fits extremely well with the numerical results.

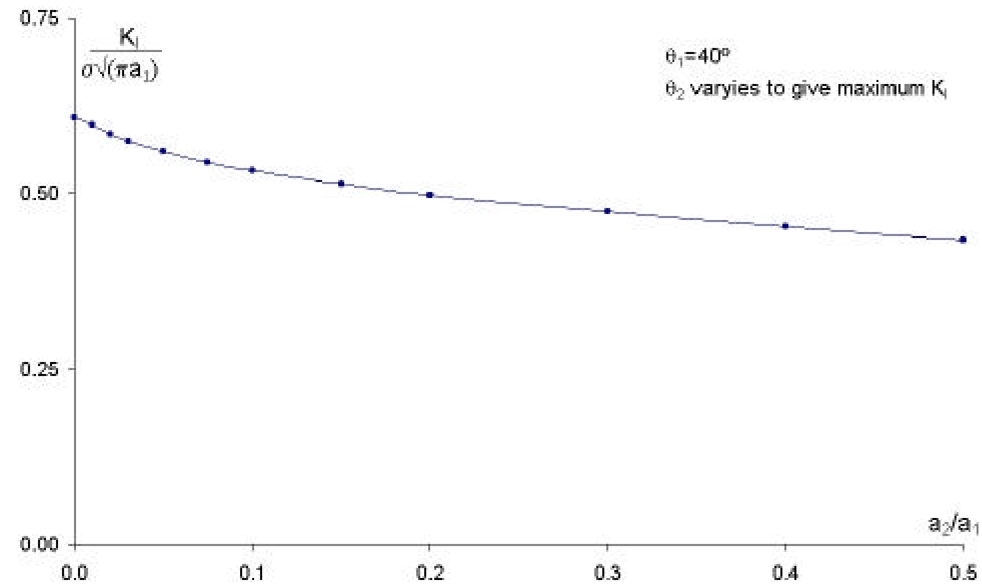

Figure 4.14 Maximum K_I with wing crack length

Figure 4.15 gives the stress intensity factor plots for a series of segment 1 crack inclinations. It can be seen that K_I increases as the inclination approaches 45 , as this is the inclination at which the driving shear stress from segment 1 is maximised.

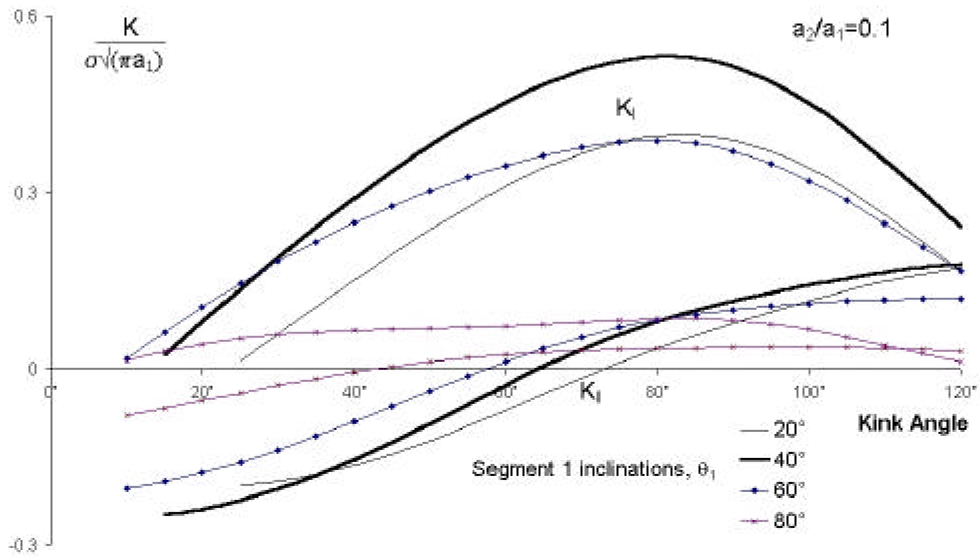

Figure 4.15 Stress intensity plots for various segment 1 inclinations

4.4 Slow crack growth under compression loading

Figure 4.14 shows that as the wing crack length is increased the stress intensity factor reduces. The conclusion drawn is that the crack would therefore self-arrest. In the special case where propagation occurs *only* when $K_I = K_{IC}$, this conclusion is correct. However, Chapter 2 showed that glass is subject to slow crack growth, resulting in increases in crack length at stress intensities inferior to the critical value. In this section the effect of slow crack growth on the compressive bading situation shown in Figure 4.4 is considered.

Recall, from Chapter 2, the equation describing slow crack growth in glass, equation (2.2).

$$v = v_0 \left(\frac{K_I}{K_{IC}} \right)^n \qquad \text{…. (2.2)}$$

An incremental procedure is followed whereby K_I is found from the wing crack results (Figure 4.14), the crack speed determined from equation (2.2), and a new wing crack length calculated for a small time step. The procedure is repeated to generate a crack length profile with time.

Figure 4.16 shows the results of slow crack growth in a particular physical case, the details of which are provided in the figure. The applied stress is that required to cause initial wing crack propagation, that is, the stress at which $K_I = K_{IC}$ for $a_2 = 0$. The figure clearly demonstrates a continued propagation of the wing crack with time, despite the fact that the stress intensity factor, as given in Figure 4.14, is falling. It is also evident that the propagation occurs rapidly, with the wing crack become half the length of the initiating crack in 1 second. The calculation was only performed over the domain of a_2/a_1 given in Figure 4.14, which corresponds to that for which the calculation of K_I for the kinked crack problem is accurate. Although the calculation of wing crack propagation must be truncated by such considerations, the general process of propagation in a traditional self-arresting environment must be taken into account in design. In fact, the only way for self-arrest to occur in the situation described here is for the stress intensity factor to reduce sufficiently so that $K_I = K_{I0}$.

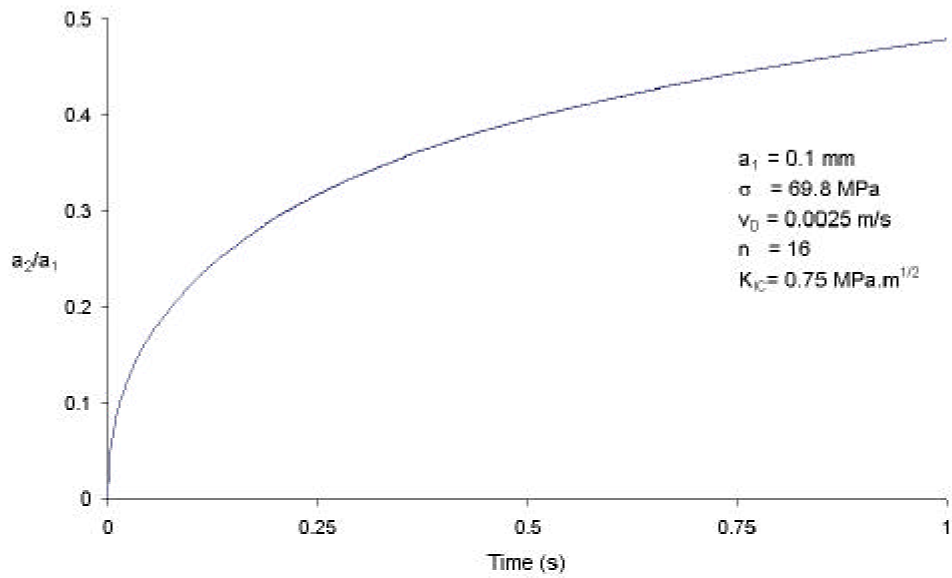

Figure 4.16 Wing crack extension with time due to slow crack growth

4.5 Application of the Crack Size Design method to compression loading

It has been demonstrated that the failure of glass under compression loading is a result of the behaviour of cracks on its surface. The Crack Size Design method proposed in Chapter 2 was tailored to this form of failure. Hence, in this section, the newly proposed method is applied to the case of uniform compression loading.

First the properties of failure in a uniform compressive field are summarised.

1) The maximum value of K_{II} for an edge crack, prior to the formation of a wing crack, is $\left|\frac{K_{II}}{s\sqrt{pa}}\right| = 0.53$, and occurs at an inclination of approximately 45 to the surface normal, assuming zero friction between the crack faces.
2) Under compressive loading, wing cracks form. The mode I stress intensity factor at the end of the exceedingly short wing crack, $K_{I,wing}$,

can be expressed in terms of the mode II stress intensity factor of the initiating edge crack in the absence of the wing crack, K_{II}, as $K_{I,wing} = \frac{2}{\sqrt{3}} K_{II}$.

3) After the initial wing crack formation, the mode I stress intensity factor at the wing crack tip reduces as the wing crack length increases. Due to slow crack growth in glass, the wing crack continues to propagate despite the reduction in $K_{I,wing}$ from K_{IC}. However, once the wing crack has reached a sufficient length this slow crack growth becomes insignificant and the crack self-arrests.
4) To increase the length of the wing crack further the applied load must be increased.
5) Global failure of the glass member is a result of the inter-connection of wing cracks, which then form larger, weaker cracks, which propagate further under the applied load.
6) The dependence of global failure on randomly arranged existing cracks results in a seemingly random ultimate member strength. In general, when this type of failure occurs it is sudden and complete.

Point (6) above is particularly problematic for the designer accustomed to the traditional allowable stress approach. In the case of tensile loading, the random element is solely the perpendicular depth of the edge cracks. For compression, additional degrees of uncertainty are introduced by the orientation and proximity of these cracks to each other. Hence, the process used to determine an allowable stress for compressive design must be even more conservative than that employed for tension. Even though the application of the Crack Size Design method to compression will also need to be inherently more conservative than the tensile design, it is based on fracture mechanical observations particular to glass, and therefore the result is a more rigorous, less conservative, design.

To commence a Crack Size Design analysis an initial crack size is required. In the derivation for tension (section 2.5.2.1), the cracks were assumed to be perpendicular to the edge, and it was shown that, even for inclined cracks, this was reasonable. In the compressive case, a perpendicular edge crack has no stress intensity factor, of either mode, at its tip and would lead to a conclusion that compressive failure of glass never occurs. This is obviously not desirable in a model which seeks to account for compressive failure. The initial crack size defined for the design method must therefore include a crack length *and* an inclination. There is no work in the literature detailing typical crack inclinations for structural glass applications. Various assumptions therefore need to be made to continue with the design process. It is assumed that the predominant orientation of cracks is perpendicular to the edge. The tensile loading material test results, used to generate the strength/probability curve of Figure 2.9, can therefore be manipulated to provide meaningful information about the distribution of crack sizes, as in section 2.5.2.1. Next it can be assumed that there is a small percentage of the cracks which have a random inclination to the surface, and that this type of crack is sufficiently rare for it not greatly to affect the tensile strength results. Under such conditions, the design crack size should be the same as that for tension, from equation (2.5), and its orientation should be such that it maximises the stress intensity factor, that is at 45 . This method will result in a conservative design crack, but, in the absence of detailed data about typical crack orientations, it is difficult to justify anything less so.

The discussion above leads to a definition of the design crack size and inclination. Using points (1) and (2) from the start of this section, it is possible to determine the mode I stress intensity factor at the initiation of the wing crack, $K_{I,wing}$, and by equating this with the critical stress intensity factor, the stress at which wing cracks appear (in the design case) can be determined. In the original formulation of Chapter 2, achievement of the critical stress intensity factor was to be avoided, as it led to sudden failure. For compression loading this is not the case. Points (5) and (6) stated that global failure occurs at some random period after wing crack initiation, due to inter-connection of cracks. This is fortuitous for design, as it provides some degree of "post-critical" capacity, even though global failure is still random and sudden. As in Chapter 2, it is proposed here that the design capacity for glass be based on the stress intensity factor. In the case of compression, equation (2.8) is revised to become

$$K^*_{I,wing} \leq f_{comp} K_{IC} \tag{4.41}$$

where $K^*_{I,wing}$ is the stress intensity factor for the design crack oriented at 45 , under the applied stress and f_{comp} is a capacity reduction factor for compression.

Consider, now, slow crack growth in compression design. Even though the design stress intensity factor may not have reached the critical value, slow crack growth will cause a sub-critical extension of the wing crack. Figure 4.17 shows two cases based on the same initial design crack. On the left the primary design crack is yet to develop wing cracks, and on the right the wing crack has grown some distance due to slow crack growth or a period of high loading in the past. The respective stresses applied to each case are s_1 and s_2. To cause crack (a) to propagate, the applied stress, s_1, must attain the critical value, s_C, corresponding to the achievement of the critical stress intensity factor on an un-propagated crack. Earlier, point (4) stated that subsequent wing crack growth required a larger applied load. Hence, for crack (b) to extend, the applied load must be greater than s_C. Also, for sub-critical stresses, where $s_1 = s_2 < s_C$, the stress intensity factor for crack (a) is greater, as demonstrated in Figure 4.17. Therefore, there is a tendency for crack (a) to grow to the state of crack (b), with the rate of growth decreasing all the time with wing crack length.

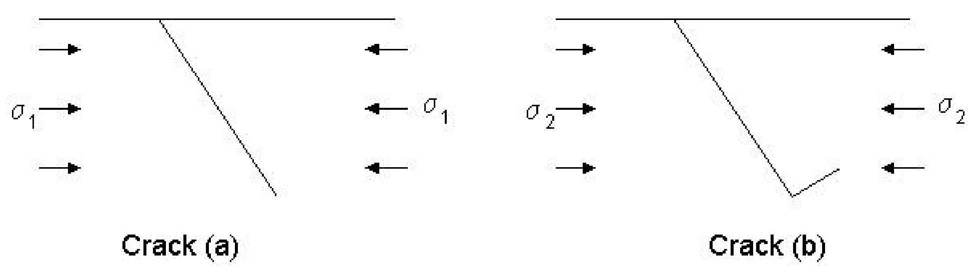

Figure 4.17 Two states of wing crack growth from the same initiating design crack

The behaviour described above indicates that the lowest load to cause propagation is that required to produce the initial wing crack on crack (a). That is, when $s_1 = s_C$. As the crack grows, the applied stress required increases. Therefore, it is proposed here that the applied stress be limited to this value over the whole life of the structure. This can be expressed alternatively by saying that $K^*_{I,wing}$ in equation (4.41) refers to the stress intensity factor of the un-kinked crack, rather than being a continually varying value as the wing crack extends. The advantage here is that the design stress then becomes constant for the whole structural lifetime, and does not vary with load history, as it did for the tension case. The result is that the general principle of glass being stronger in compression than tension is maintained, as the slow crack growth under tension leads to much smaller design stresses than the constant value used in compression.

The one consideration omitted in the discussion above is one associated with the proximity of kinked cracks to each other. If the stress is maintained below the critical value, s_C, as explained above, then a crack will never propagate through the stress intensity factor reaching the critical value. Therefore, wing cracks will only form through slow crack growth mechanisms. However, there has been no allowance for the inter-connection of wing cracks. This is because the discussion so far has been focused on the fracture mechanics of the problem, while inter-connection is a probabilistic concern. As such, it is proposed that it be accounted for in the choice of f_{comp}. The exact determination of this factor relies on a more detailed account of the typical distribution of cracks in structural glass, and will therefore not be considered in detail here.

Chapter 5

Complete contact between a rigid punch and an elastic layer attached to a dissimilar substrate with interfacial friction

5.1 Introduction

The preceding chapters of this thesis have been concerned with the design of glass for bulk member stresses, such as the tension on the bottom face of glass beams. The remainder of the thesis describes investigations of the stresses developed under contact zones, which have rapidly varying stress fields with generally large stress concentrations. In particular, the case of a "bearing pad" is considered (see Figure 1.4).

Classical bearing design methods frequently used in civil engineering, based on either an elastic limit design or a plastic limit state approach, are inappropriate for use with glass, as the severity of the stress state as quantified by a yield parameter is unimportant. The crucial quantity for truly brittle materials like glass is the presence of a mode I stress intensity factor, generally generated by the presence of tension. Even under conditions where, *prima facie,* all the principal stresses are negative or zero, such as the loading developed beneath a punch, tension may develop as a result of the effect of interfacial frictional shear. The intention in this chapter is to quantify these effects, for the case where a thin, linear elastic interlayer is present. Although regions of tension may appear at many locations throughout a structural element it is the neighbourhood adjacent to contact loading which suffers the severest stress gradients, with the potential for local regions of high tension.

This chapter is targeted at linear elastic interlayer materials, such as stiff rubbers. Note that, in fact, few materials are perfectly linear elastic, but may be assumed to be so to simplify the analysis. The case being investigated is shown in Figure 5.1. In more general terms it may be specified as the analysis of the contact pressure distribution for a square ended rigid punch, pressing normally onto an elastic layer, itself attached to an elastically dissimilar half plane, under plane deformation.

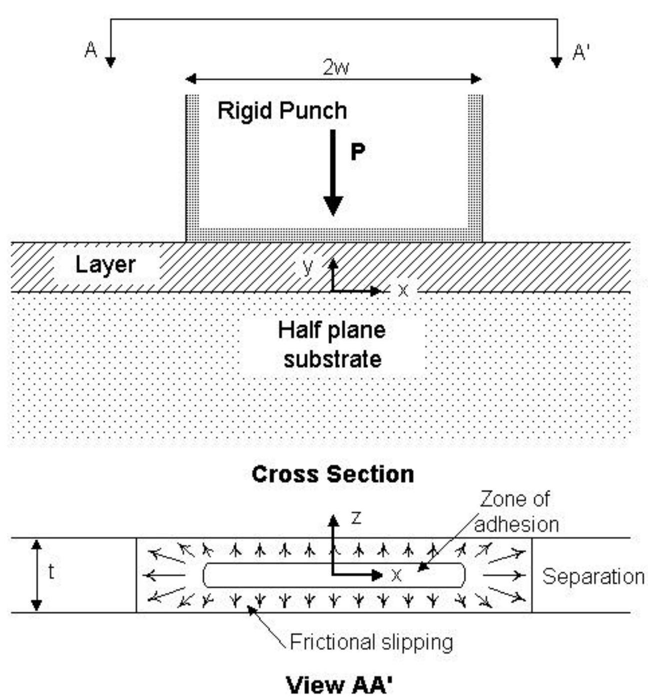

Figure 5.1 Geometry of the problem

In the first stage of the analysis, the interlayer is assumed to be either perfectly adhered or fully lubricated along its upper and lower surfaces. Solutions are provided for all four possible combinations of adhesion and lubrication. The second phase of the solution then considers finite friction along the interlayer/half plane interface. Finally, the presence of an edge crack in the half plane is considered, and the possibility of propagation is investigated.

The solution produced is valid for both plane strain and plane stress conditions. It is worth discussing, here, which of the two is more applicable to the edge loading of plate glass, as shown in Figure 5.1. Section AA' of Figure 5.1 shows that there is frictional slipping in every direction in the xz plane of the interface. If the plate thickness, t, were infinite, there would only be displacements in the x direction, and plane strain conditions would result. If, on the other hand, t was sufficiently small that displacements in the x direction were minimal, then a plane stress analysis would be most appropriate. It was shown in section 2.3 that the predominant cracks found on the edges of structural glass members extended *across* the width of the glass edge. Such cracks are most susceptible to stresses in the xy plane. A plane stress analysis assumes negligible displacements in the x direction, and therefore will produce small stresses in the critical xy plane. Therefore, a plane strain analysis is most appropriate for design, as it maximises the calculated stresses critical to the crack, and therefore to failure. It should be noted that this implies that the results will be an upper bound, and lead to a conservative design.

5.2 Formulation for the rigid punch

The technique to be used here is the standard Fourier transform principle (see Sneddon, 1951), which has been applied by several authors to plane contact problems, for example Jaffar (1989) and Bentall & Johnson (1968). The innovations included here are, first, that the problem is cast as a true boundary value problem of the second kind, with an unknown contact pressure distribution to be found in order to achieve uniform displacement. This has been done before, for example by Bentall & Johnson (1968) and Nowell & Hills (1988), but only for *incomplete* contacts. This raises the issue of how the anticipated singular points of contact pressure expected at the corners of the punch should be treated, which takes us to the second innovation, viz. that the solution is cast as a perturbation of the half plane solution, and which therefore includes the singular dominant term in the solution: hence only a modest modification is needed for interlayer pads of realistic thickness.

The general form of the problem to be solved is shown in Figure 5.1. If there is no interlayer present the contact pressure distribution, $p(x)$, under the punch is of the classical Flamant half plane solution form, $p \propto w \big/ \sqrt{w^2 - x^2}$ (Hills *et al.*, 1993), where w is the punch half-width. Equally, if the interlayer is thick, ie. the ratio b/w becomes large, where b is the thickness of the interlayer, this would be expected to be the asymptotic form of the contact pressure. This therefore forms the first element of the solution, and the first task is to find the surface normal displacement, produced by this pressure distribution, within the elastic interlayer. Further, regardless of the aspect ratio of the pad, the form of the local asymptotic solution will be the same in the neighbourhood of the corner (Williams, 1952). It is the intention here to superimpose on this contact pressure a further, unknown distribution, represented by a series of overlapping triangles, as shown schematically in Figure 5.2. These triangles form a piecewise linear approximation to the corrective term, and this is well behaved and finite. The second phase of the solution is therefore to find the surface displacement given by an arbitrary triangle of pressure.

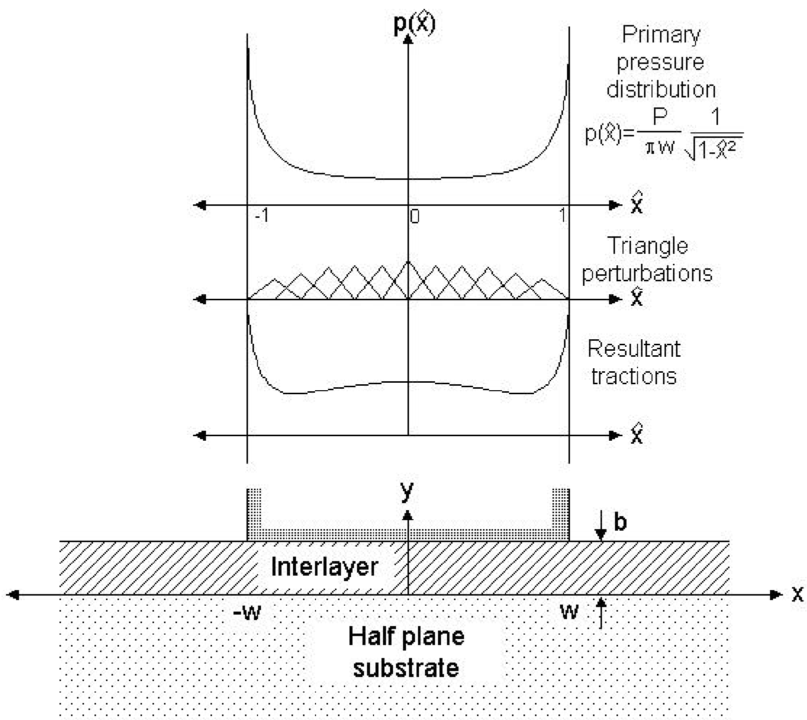

Figure 5.2 Primary pressure and perturbation

5.2.1 The Fourier transform

The solution technique used here to find stresses and displacements in the interlayer and half plane follows the Fourier transform method, given in detail in a report by Kelly *et al*. (1993). For a general description of the Fourier transform method, the book by Sneddon (1951) should be consulted. A synopsis of the full method is given in Appendix C. The cosine Fourier transform of a normal load, $p(x)$, applied to the upper surface of the interlayer, is given by

$$\tilde{p}_c(l) = \int_0^\infty p(x)\cos(lx)dx\,. \tag{5.1}$$

This will be applied both to the fundamental pressure distribution, and to the perturbation. For the remainder of this chapter the coordinate system is normalised with respect to *w*, the punch half-width, so that $\hat{x} = x/w$, $\hat{y} = y/w$ and $\hat{b} = b/w$. The magnitude of the pressure distribution found beneath a square ended punch resting on a half plane is normalised with respect to the load (*P/wp*), so that

$$\frac{wp}{P}p(\hat{x}) = \frac{1}{\sqrt{1-\hat{x}^2}} \text{ on the interval } -1 \le \hat{x} \le 1\,. \tag{5.2}$$

If this is substituted into equation (5.1) with the normalised variables and the integral evaluated, it may be shown that

$$\frac{wp}{P}\tilde{p}_c = w\frac{p}{2}J_0(l) \tag{5.3}$$

where J_0 is the Bessel function of the first kind, of order zero.

Consider, now, a triangular element of pressure, of height p_0, and of half-width w_{tri} with a pressure distribution as expressed below. The element width is also normalised with respect to the punch half-width, giving $\hat{w}_{tri} = w_{tri}/w$.

$$\begin{aligned} p(\hat{x}) &= 0 && \hat{x} \le -\hat{w}_{tri},\ \hat{x} \ge \hat{w}_{tri} \\ p(\hat{x}) &= \frac{p_0}{\hat{w}_{tri}}(\hat{w}_{tri} + \hat{x}) && -\hat{w}_{tri} \le \hat{x} \le 0 \\ p(\hat{x}) &= \frac{p_0}{\hat{w}_{tri}}(\hat{w}_{tri} - \hat{x}) && 0 \le \hat{x} \le \hat{w}_{tri} \end{aligned} \tag{5.4}$$

If equations (5.4) are substituted into equation (5.1), the following emerges from the integral as the cosine Fourier transform of the triangle of pressure.

$$\frac{\tilde{p}_c}{p_0} = \frac{-(\cos(\hat{w}_{tri}\, l) - 1)}{\hat{w}_{tri}\, l^2} w \qquad (5.5)$$

The next step is to determine the surface normal displacements associated with the transformed contact pressure. These may be found using standard procedures, as given in Appendix C, which also account for the shear traction conditions along both surfaces of the interlayer. Appendix D summarises the results for the four combinations of frictionless and full adhesion conditions along each surface. The results are also given in a general form to allow for both transverse plane strain and plane stress. It should be noted that the results are given in terms of $\tilde{p}_c$ and so apply to each of the transformed loads in equations (5.3) and (5.4).

5.2.2 Use of influence functions

The surface normal displacement arising on the surface of the layer of thickness b (= $0.4w$) is shown in Figure 5.3 assuming the half plane pressure distribution, ie. $wpp(\hat{x})/P = 1/\sqrt{1-\hat{x}^2}$. It may be seen that, within the intended contact region, the surface displacement is far from constant. To make the displacement constant, which it will be if the punch is rigid, a series of triangles of normal pressure is added over the contact, as shown in Figure 5.2. This forms a corrective, piecewise linear pressure distribution which falls to zero at the edges of the contact, so that the singularity of the primary half plane pressure distribution of equation (5.2) is preserved. The surface displacement due to a single triangle is used as an influence function to build up the corrective solution.

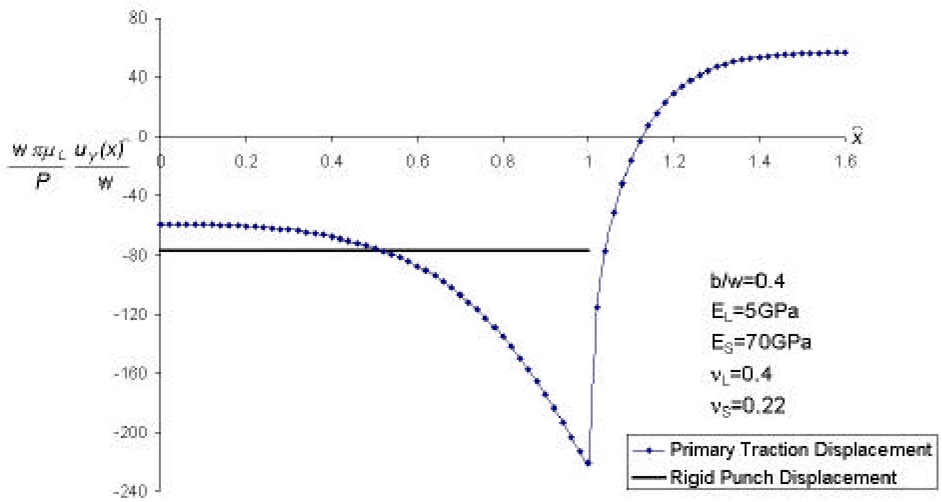

Figure 5.3 Surface normal displacements for rigid punch and pressure of the form $wpp(\hat{x})/P = 1/\sqrt{1-\hat{x}^2}$ relative to the origin

First, equation (5.5) is substituted into Appendix D equation (D.7) to give the vertical displacement (u_y) due to a triangle of pressure centred on the origin, of height p_0. The displacement field relative to the origin is of the form

$$u_y(\hat{x},\hat{y}) = K(\hat{x},\hat{y})\,p_0\,. \tag{5.6}$$

In particular, the displacement of the upper surface of the interlayer due to a centrally located triangle, relative to the origin, is therefore

$$u_{\hat{b}}(\hat{x}) = K(\hat{x},\hat{b})\,p_0\,. \tag{5.7}$$

and similarly, the displacement of the top of the glass half plane, relative to the origin, is

$$u_0(\hat{x}) = K(\hat{x},0)\,p_0. \tag{5.8}$$

The influence function (u_{tri}) required for the solution gives the displacement of the interlayer upper surface relative to the origin due to a triangle centred on the point $\hat{x} = x$.

$$u_{tri}(\hat{x},x) = u_b(\hat{x}-x) + u_0(-x) \tag{5.9}$$

The base of the punch is divided into *2n* equal sections, with *2n-1* triangles of pressure superimposed over this width. The width of each triangle is therefore $w_{tri} = w/2n$. Having determined the influence function for a single triangular element of unit height, it is required to find the altitudes of the superimposed triangles ($p_0(i)$) such that, together with the fundamental half plane solution ($u_{primary}$), a constant displacement results over the punch width (u_f). As the loading is symmetric about the origin there are *n* unknown triangle heights to be found (the central triangle is the only unpaired one). The final displacement of the punch (found relative to the origin) is also unknown, therefore giving rise to *n+1* unknowns. The *n+1* equations for the solution come from setting the origin and the *n* points to one side of it equal to the unknown final punch displacement. Equation (5.10) gives the set of equations to be solved.

$$u_{tri}(\hat{x},0)\,p_0(1)+\left\{\sum_{j=2}^{n}\left[u_{tri}(\hat{x},x)+u_{tri}(\hat{x},-x)\right]p_0(j)\right\}-u_f=-u_{primary}(\hat{x}) \quad (5.10)$$

where

$$\hat{x}=\frac{i-1}{n} \qquad \text{for } 1\le i\le n+1$$

$$x=\frac{j-1}{n} \qquad \text{for } 2\le j\le n$$

Figure 5.3 shows, in the curve denoted by diamonds, the surface normal displacement ($u_{primary}$) produced by the underlying load distribution $p(\hat{x})=1\big/\sqrt{1-\hat{x}^2}$. The modified solution is then formed by adding load such that it gives the same maximum displacement: the load is then scaled back, and the constant displacement produced by the same applied load is found. This is included on Figure 5.3, and gives information about the compliance of the contact.

Once the set of simultaneous equations described above has been solved to give a rigid punch pressure distribution for the layered problem, the stresses in the layer may be found. Equations (D1), (D2) and (D3) of Appendix D are used to combine the stresses resulting from the primary traction of equation (5.2) together with those arising from the triangles, giving the net stress fields in the layer, as described in the following section.

5.3 Rigid punch results

Figure 5.4 shows the corrective contact pressure distribution, that is the combined heights of all the triangles of pressure, as described above, for various interlayer thickness/width aspect ratios, for the case where the punch/interlayer interface is frictionless, and the interlayer/half plane interface is fully adhered. If the corrective contribution is now combined with the primary solution, the pressure distributions shown in Figure 5.5 are obtained. The results have been scaled so that each represents the stress profile under the same net bad. It is evident from the figure that the pressure distributions vary only slightly over the range of layer aspect ratios investigated.

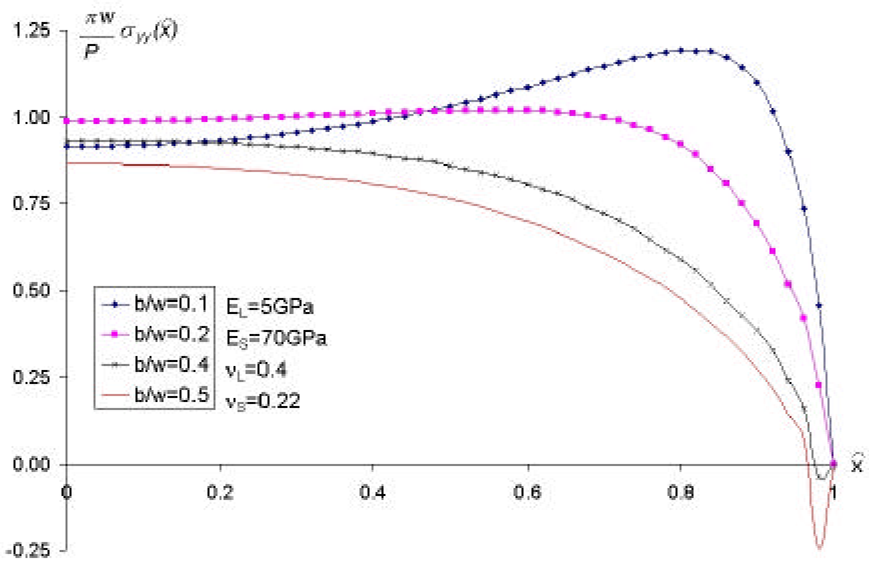

Figure 5.4 Corrective Pressure Distributions

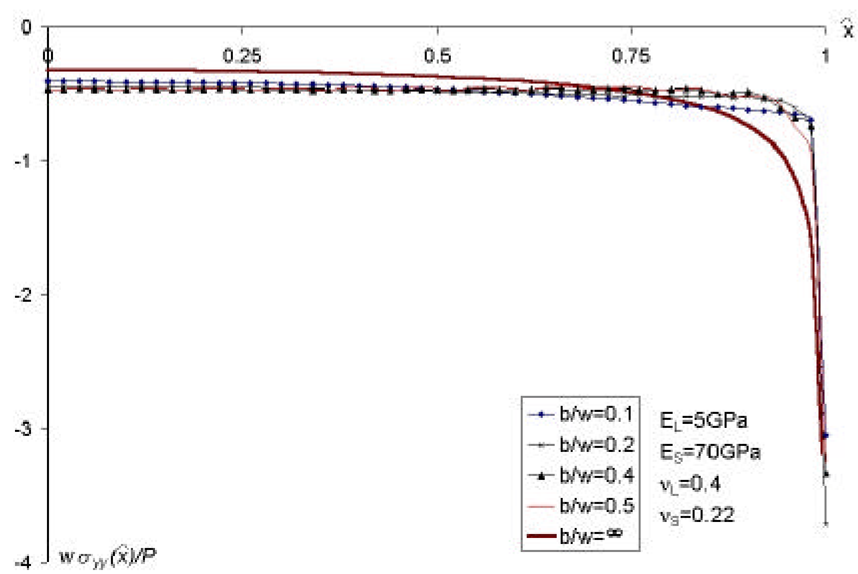

Figure 5.5 Comparison of resultant pressure distribution for various layer thicknesses

Figure 5.6 takes a single layer aspect ratio, $b=0.1w$, and provides a comparison of the contact pressure distribution for the four cases corresponding to all combinations of fully adhesive and frictionless conditions along the two surfaces. It can be seen that the variation in the pressure distribution is only very weakly dependent on the interfacial shearing tractions, at least for this particular aspect ratio. The same result was found for all the aspect ratios listed in Figure 5.5.

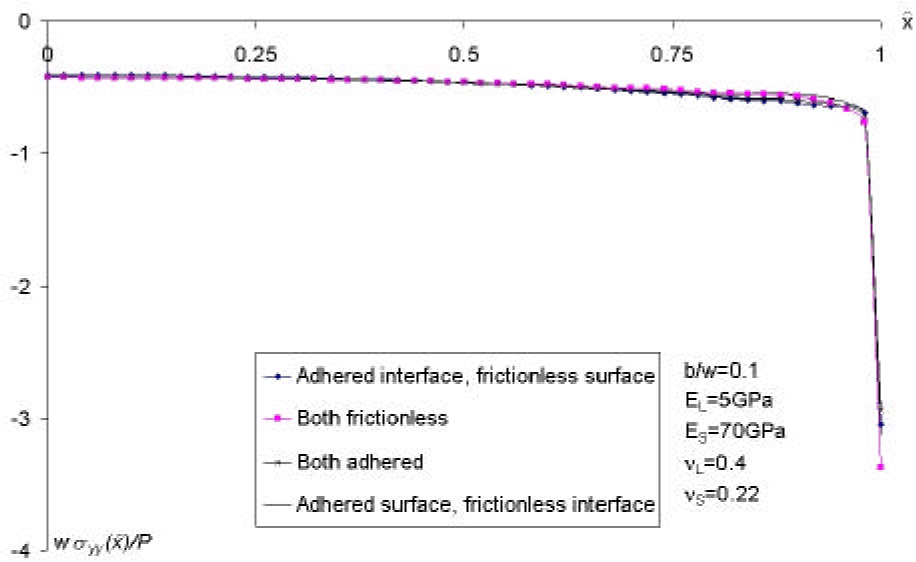

Figure 5.6 Pressure distributions for the four frictional cases

When the interlayer/half plane interface is frictionless, no shear tractions arise on the surface of the half plane. However, in the cases where it is assumed that this interface is perfectly bonded, it is clear that shear tractions must arise, and they are determined as part of the solution. A series of results is given in Figure 5.7 for different pad aspect ratios for the case of zero friction under the punch and full adhesion between the interlayer and substrate. The method is, in fact, able to generate a stress field for the whole half plane, but for brevity these results are not developed here.

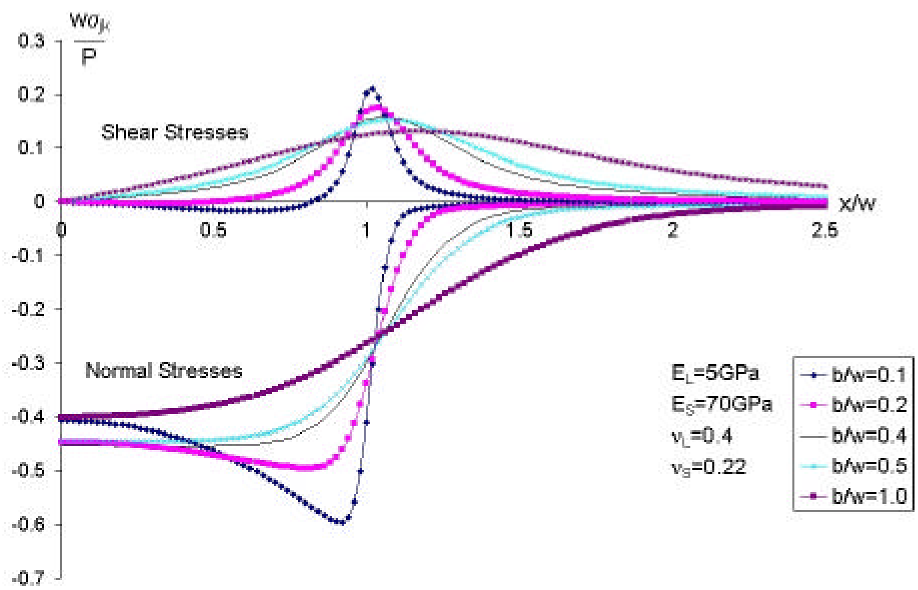

Figure 5.7 Interface tractions for full adhesion and an interlayer of infinite width

5.4 Formulation for finite interlayer/substrate interfacial friction

The solution given above is complete providing that (a) the interlayer is glued to the substrate, and hence is capable of transmitting direct tractions of either sign, and (b), the interface is capable of transmitting shear tractions of any magnitude. This could be sustained by glue, or, if the coefficient of friction is sufficiently high, by frictional effects where the interfacial contact pressure is compressive everywhere. In practice these conditions are not usually met, and hence the relevant tractions must be relaxed out in a meaningful way, by allowing for slip and separation regions, as sketched in Figure 5.8. An attempt was made to incorporate finite friction into the Fourier transform method used in previous sections. Appendix E gives the formulation for such a case. It shows the resulting equations to be difficult to solve, and the approach was therefore abandoned in favour of a distributed dislocation technique.

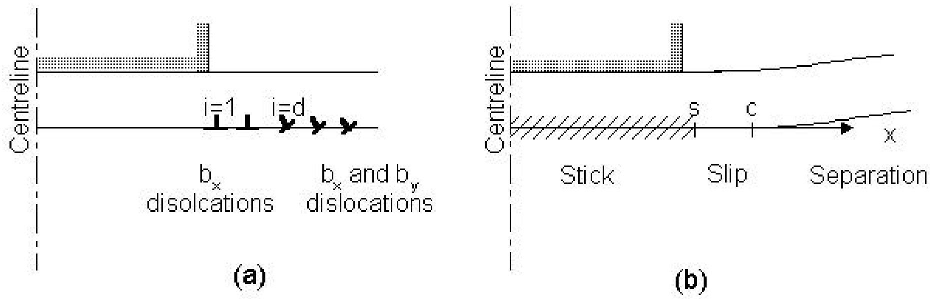

Figure 5.8 Schematic of the interface (a) Dislocations used in model (b) Interface zones (stick, slip, separation).

It has been shown in Figure 5.6 that the interfacial shearing conditions have only a very weak effect on the distribution of *contact pressure* (that is, σ_{yy}). However, the relaxation of an adhered contact in regions where the limiting friction is exceeded does have a major effect on the local stress state in the half plane, and it is the intention here to show how the presence of slip and separation may be incorporated into a model assuming complete adhesion. As it has been shown that the shear traction distribution has an infinitesimal effect on the contact pressure, it is acceptable to split the problem up so as to uncouple the effects of separation and slip on the contact problem itself.

The basic strategy to be used is as follows: it is assumed that the contact problem has already been solved, with the assumption that the interlayer/substrate interface is completely adhered (while either fully adhesive or fully lubricated conditions could be included for the upper interlayer face). Separately, the solution is found for the stress state induced by a single dislocation, present at a point along the interlayer/substrate interface. When this has been done, it follows that any number of dislocations may be distributed anywhere within the components, without violating any boundary conditions on the *upper* interface of the interlayer, Figure 5.8(a). Of particular interest here is the effect of the dislocations on the traction components of stress arising along the interface. They are installed so that the unilateral boundary conditions demanded by a simply supported interlayer may be achieved. Once the modified surface traction distribution along the interlayer/substrate interface has been found, the internal stress state may be calculated using Muskhelishvili potential methods.

Dislocations having a Burgers vector in the *y*-direction will be needed to model the effects of separation, and dislocations having a Burgers vector in the *x*-direction will be needed both to model slip in regions where there is normal compression, insufficient to sustain adhesion, and also in regions of separation, where tangential relative slip is present. The formulation for determining the stress state associated with these dislocations was given by Comninou & Dundurs (1983). For a dislocation located at the origin, the relevant components of stress, along the interface, are given by

1. Climb dislocation

$$s_{yy}(x,0) = \frac{m_S(1+a)b_y}{p(k_S+1)(1-b^2)}\left[\frac{2}{x} - \frac{1-a}{b}\int_0^\infty \frac{N_{11}}{D} e^{-t} \sin\frac{xt}{b}\,dt\right] \tag{5.11}$$

$$t_{xy}(x,0) = \frac{m_S(1+a)b_y}{p(k_S+1)(1-b^2)}\left[2pbd(x) - \frac{1-a}{b}\int_0^\infty \frac{N_{12}}{D} e^{-t} \cos\frac{xt}{b}\,dt\right] \tag{5.12}$$

2. Glide dislocation

$$s_{yy}(x,0) = \frac{m_S(1+a)b_x}{p(k_S+1)(1-b^2)}\left[-2pbd(x) + \frac{1-a}{b}\int_0^\infty \frac{N_{22}}{D} e^{-t} \cos\frac{xt}{b}\,dt\right] \tag{5.13}$$

$$t_{xy}(x,0) = \frac{m_S(1+a)b_x}{p(k_S+1)(1-b^2)}\left[\frac{2}{x} - \frac{1-a}{b}\int_0^\infty \frac{N_{22}}{D} e^{-t}\cos\frac{xt}{b}\,dt\right] \tag{5.14}$$

where

$$a = \frac{m_L(k_S+1) - m_L(k_L+1)}{m_L(k_S+1) + m_L(k_L-1)}$$

$$b = \frac{m_L(k_S-1) - m_L(k_L-1)}{m_L(k_S+1) + m_L(k_L-1)}$$

$$D = (1-b^2)e^{2t} + (a^2 - b^2)e^{-2t} - 4(1+b)(a-b)t^2 - 2(a-b^2)$$

$$N_{12} = 4[(1+b^2)t^2 + b]e^t - 2b(1+a)e^{-t}$$

$$N_{11} = 2\{2(1+b)[(1+b)t + 1 - b]t + 1 + b^2\}e^t - 2(a+b^2)e^{-t}$$

$$N_{22} = 2\{2(1+b)[(1+b)t - (1-b)]t + 1 + b^2\}e^t - 2(a+b^2)e^{-t}$$

μ_i = the modulus of rigidity of component i

$d(x)$ = the Dirac delta function.

It is worth plotting out these stresses to enable their characteristics to be visualised, and they are depicted in Figure 5.9. Note that, for a climb dislocation, s_{yy} is anti-symmetric and t_{xy} is symmetric, whilst, for a glide dislocation, the reverse is true.

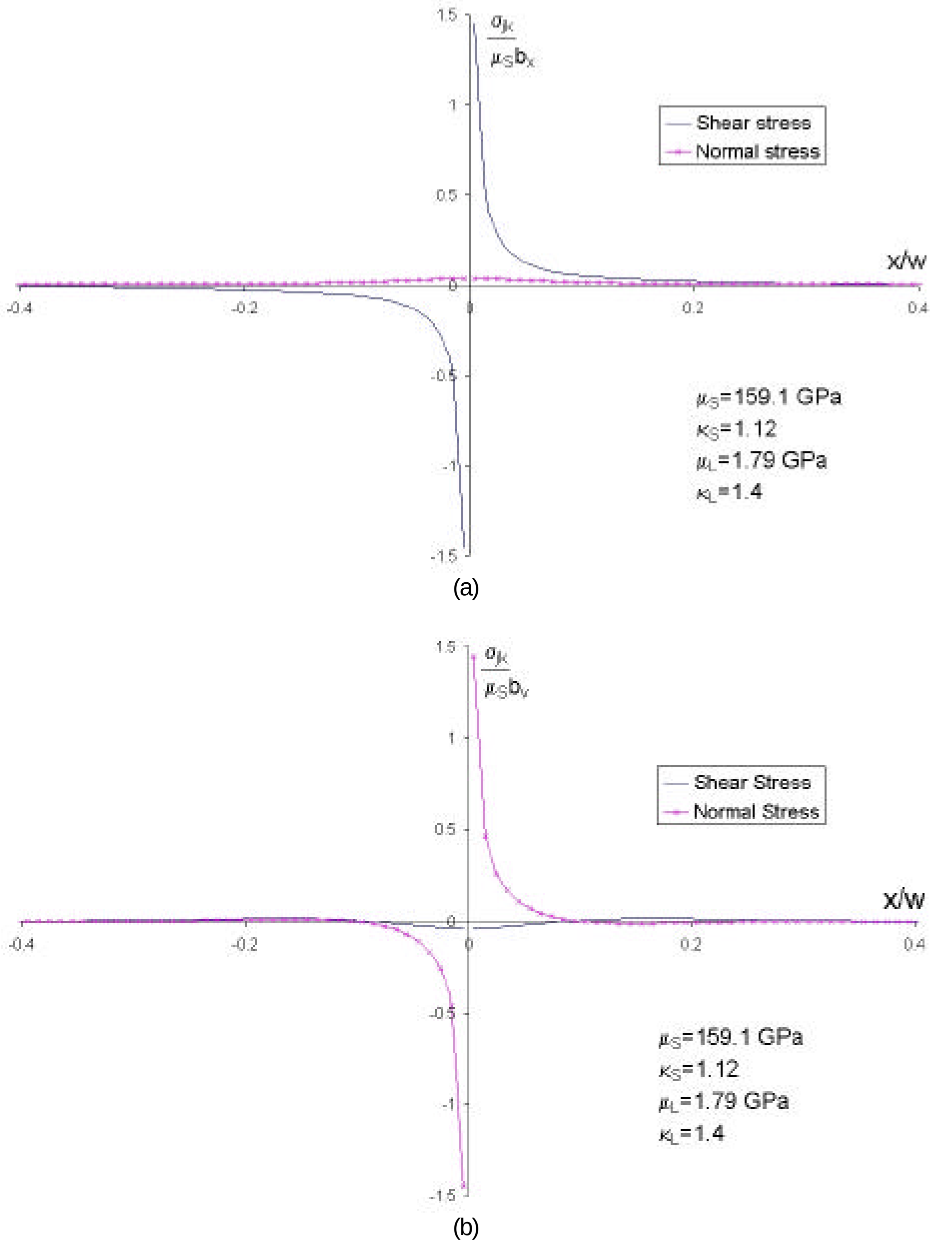

Figure 5.9 Stresses arising from a single dislocation. (a) for glide type, (b) climb type

Consider, now, the use of these dislocations in modifying the interfacial conditions in the prototypical problem. As the problem has inherent symmetry, only one half of it ($x \geq 0$) will be studied. However, it must be borne in mind that a dislocation installed along the half-line $x < 0$ will have an effect on the half-line $x > 0$, and so, these too, must be taken into account. From considerations of symmetry and anti-symmetry, it is seen that b_x (glide) dislocations must be installed symmetrically, and b_y (climb) dislocations anti-symmetrically. Formally, a continuous distribution of dislocations, of each type, must be distributed. However, it is well known that, in problems of this kind, where dislocations are present along an interface, difficulties can arise in the nature of the stress state present at the gap/closure and stick/slip transition points (Comninou, 1977). In the present solution, therefore, it was decided that a satisfactory solution could be obtained by installing an array of *discrete* dislocations. One reason for this approximation being acceptable is that the region of interest is immediately beneath the punch itself, whereas the regions in which dislocations are to be employed are well to either side. In any event, it was found that using an array of discrete dislocations was computationally efficient, there were no convergence problems, and a smooth corrective solution was readily found.

The solution was developed in stages. It is clear that, beneath the punch, there is both closure of the interface, and adhesion. The first refinement to be added was therefore to choose a coefficient of friction, f, and to install glide dislocations where necessary to restore the slip condition $|\tau_{xy}| = -f\ \sigma_{yy}$. This provides a worthwhile improvement in accuracy, but also both highlights and exacerbates the problem of large regions of moderately tensile contact 'pressure' developing further from the punch.

In order to correct this, climb dislocations are installed over the region of tension, in order to obtain the boundary condition $t_{xy} = s_{yy} = 0$ in regions of separation. It should be noted that there is coupling between the effects of the glide dislocations (which affect the direct traction as well as the shear component), and the climb dislocations (which affect the shear traction as well as the direct component). Further, the stick/slip transition points and gap/closure points are unknowns of the problem, and do *not* correspond to the points where the slip condition and non-positive direct traction conditions arise in the bilateral solution. A satisfactory solution is reached when the transition points are found such that there are no violations of any of the inequalities. These are:

Stick zone: $|t_{xy}| < -f\ s_{yy}$ $\quad$ $dg/dx=0$ $\quad$ (5.15)

Slip zone: $|t_{xy}| = -f\ s_{yy}$ $\quad$ $sgn(dg/dx) = sgn(t_{xy})$ $\quad$ (5.16)

Contact region: $s_{yy}<0$ $\quad$ $dh/dx=0$ $\quad$ (5.17)

Separation region: $s_{yy}=0$ $\quad$ $dh/dx>0$ $\quad$ (5.18)

where $h(x)$ is the relative surface normal displacement and $g(x)$ is the relative surface tangential displacement.

Thus, in addition to the equations stated earlier, the separation of the two components must be positive exterior to the closure point, and the slip direction must be consistent with the slip direction within the slip regions.

5.5 Numerical implementation for interfacial slip and separation

The problem is coded so that the strength of n sets each of climb and glide dislocations may be determined. In principle both sets of dislocations have to be distributed over infinite domains either side of the punch, but in practice it is found that truncating the distance to $5w$ gives results of sufficient numerical accuracy.

Schematics of the arrangement of dislocations and zones of stick, slip and separation are shown in Figure 5.8. It is assumed in the figure, and in the full solution, that separation will occur, but as a precursor to this full solution the case where separation is ignored, i.e. where the presence of moderate amounts of interfacial tension are tolerated, was considered. The bilateral solution implies significant zones where the limiting friction condition is exceeded, and that the normal contact pressure is negative almost everywhere in the neighbourhood of the punch, but with remote regions where small tensile tractions are present. This therefore suggests that a simplified model incorporating slip, but without attempting to model separation will be sufficient to produce a consistent solution. Here, therefore, there are only two distinct zones: stick and slip.

To model the slip with dislocations the following implementation of equation (5.16) is used,

$$\sum_{i=1}^{n} K_{xygi}(x,x)b_{xi} = -t_{xy}(x) \pm f\left[s_{yy}(x) \pm \sum_{i=1}^{n} K_{yygi}(x,x)b_{xi} \right] \qquad (5.19a)$$

where $K_{jkgi}(x,x)$ is the contribution to the stress σ_{jk} induced at point x by the i^{th} glide dislocation, which is at a distance ξ from *x*. The kernels may be derived from equations (5.11)-(5.14). Note that the effect of the corresponding mirror image dislocations have been included, and that g implies glide dislocations.

The semi-extent of the stick zone is denoted by s and the separation transition point by *c*. Both are unknowns of the problem, and their values are coupled in the full solution. In the first part of the numerical solution the possibility of separation is ignored, and the problem therefore reduces to one in which there is a central stick region with slip zones, of opposite sign, extending indefinitely on either side. Equations (5.19a) therefore constitute a set of *n* equations in *n+1* unknowns, since s is unknown. The additional piece of information required is supplied by the inequality and sign requirement, equations (5.15) and (5.16), paying particular attention to regions adjacent to the stick-slip transition point. A value of *s/w* was therefore guessed, a solution was found, and the side conditions were checked. If either was violated the guessed value of s was adjusted, and a new solution found. This procedure was repeated until an internally consistent solution was discovered. This simplified solution leads to the introduction of zones of moderate tension, which were previously absent, arising along the surface. A separation zone was therefore added in the full model.

To model separation it is necessary to introduce climb dislocations into the system, as shown in Figure 5.8a. The relaxation of normal stresses in the region $x > c$ is achieved through the following equation, which is a numerical implementation of equation (5.18) with kernels given by equation (5.11) and (5.12).

$$\sum_{i=d}^{n} K_{yygi}(x,x)b_{xi} + \sum_{i=d}^{n} K_{yyci}(x,x)b_{yi} = -s_{yy}(x) \tag{5.20}$$

where the subscript c denotes a climb dislocation, and in addition, the following full form of equation (5.19a), allowing for the presence of climb dislocations, is now required.

$$\begin{aligned}\sum_{i=1}^{n} K_{xygi}(x,x)b_{xi} + \sum_{i=1}^{n} K_{xyci}(x,x)b_{yi} = \\ -t_{xy} \pm f\left[s_{yy}(x) \pm \left(\sum_{i=1}^{n} K_{yygi}(x,x)b_{xi} + \sum_{i=1}^{n} K_{yyci}(x,x)b_{yi}\right)\right]\end{aligned} \tag{5.19b}$$

Equations (5.19b) and (5.20) provide $2n$ equations for the climb dislocations (b_{yi}), and glide dislocations (b_{xi}). Additional side conditions needed to establish the point of separation are given by equations (5.17) and (5.18).

The final phase of the solution is to determine the internal stress state within the half plane. As the interfacial shearing traction is now known this is readily achieved by considering the half plane problem *in isolation*, and taking the interfacial traction distributions just found. Piecewise linear approximations to both the direct and shear tractions are found and sets of overlapping triangles used to model these, as was done for the primary contact problem. The Muskhelshivili potential associated with a triangle of traction is known, and hence the total internal stress state is found by superposition.

5.6 Interfacial slip and separation results

Figure 5.10 shows the traction distribution arising along the interface for three aspect ratios of the interlayer, and a coefficient of friction of 0.5. The stick/slip transition point is the discontinuity in slope in the shear traction distribution lines. It can be seen that this occurs a little way inside the edge of the punch, and that as the interlayer becomes thinner, the stick zone extends over a greater region. This is to be expected, as qualitatively the pressure distribution becomes more localised towards the punch corner.

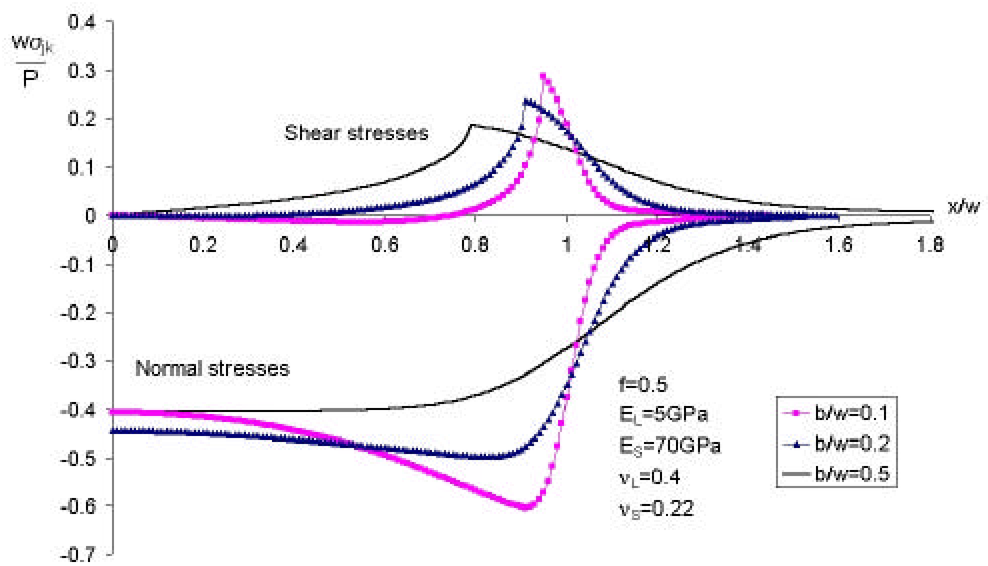

Figure 5.10 Traction distributions for various layer thicknesses

Figure 5.11 gives the results for the tractions along the substrate surface for a constant interlayer aspect ratio, but with varying degrees of interfacial friction. The contact pressure distribution is little affected by the shear traction distribution, as expected from section 5.3. The shear traction distribution for full adhesion is included for comparison with those where friction limits its magnitude. The form of the shear traction distributions calls for comment, as it seems, *prima facie*, that the shear traction is *higher* when slip is present than in the adhesive case. A set of lines is shown on the figure which plots the ratio of the shear to direct traction. It can be seen that, for the adhered case, this ratio becomes unbounded as the contact pressure becomes very small, and the separation region is approached. Some slip is therefore inevitable, and this causes a re-distribution of the shear traction, towards the region in which the contact pressure is rising. It follows that the friction-limited traction does indeed have a higher absolute value than the adhered case, and it may be seen that the traction ratio correctly equals the coefficient of friction in the slip zone (the ordinate of the graph should be interpreted as dimensionless for this family of lines).

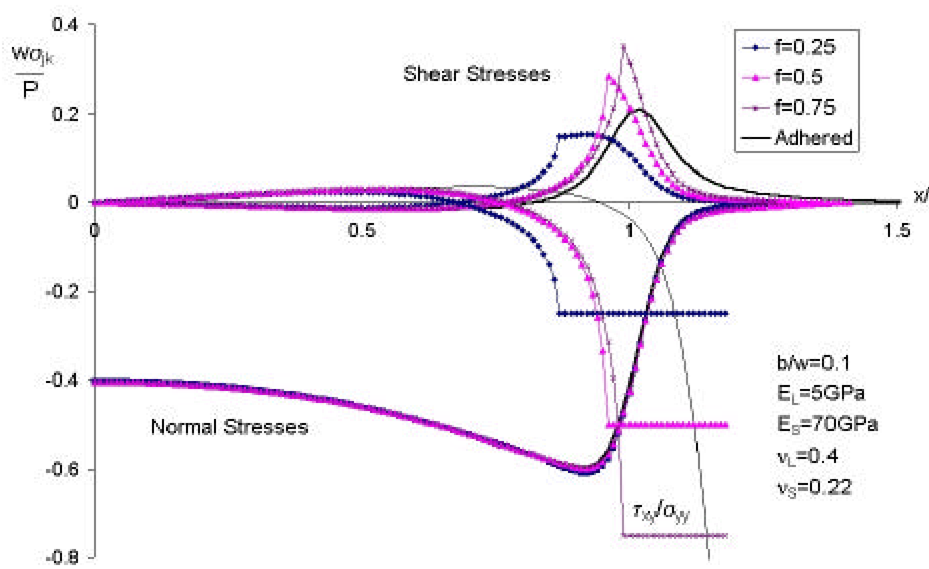

Figure 5.11 Traction distributions for several coefficients of friction

Figure 5.12 gives a more complete picture of the surface stress state arising on the surface of the half plane. First, note that the direct stress, s_{yy}, is the same as the contact pressure, and that, if we consider this as an imposed traction problem, from Way's theorem (Way, 1940) the stress parallel with the free surface, s_{xx}, must be equal in magnitude and of the same sign as the contact pressure. The value of the same component of stress, but due to the *combined* contact pressure and frictional shearing traction, is included in the figure. It may be seen that this is slightly higher than the frictionless case within the contact, although still significantly compressive, and, indeed, it is slightly more compressive external to the contact. This is consistent with an intuitive consideration of the influence of the shearing traction, which tends to stretch material beneath the contact whilst compressing it externally.

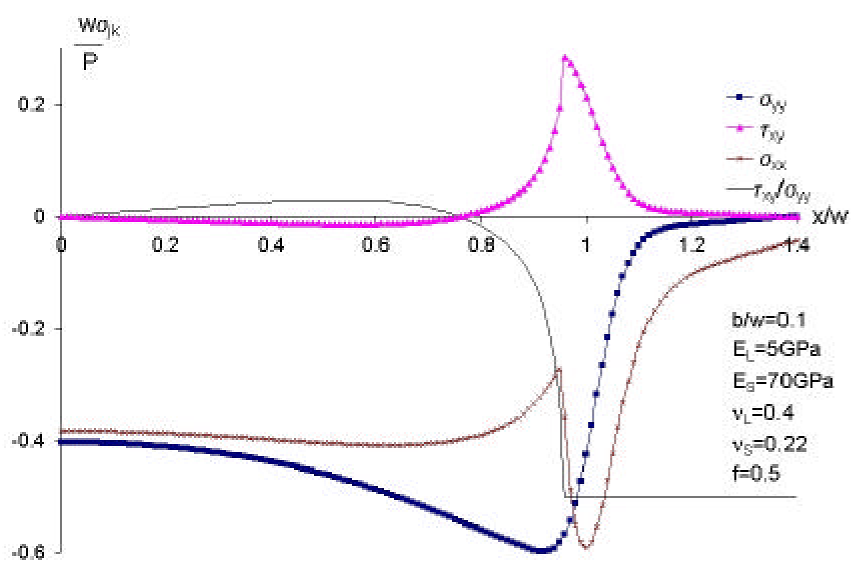

Figure 5.12 Half plane surface stresses

Figure 5.13 gives some indication of the full-field stress state developed beneath the contact. Figure 5.13(a) shows the biggest (most positive) principal stress obtained using the method described, and this may be compared with a plot of the same quantity found under frictionless interfacial conditions in Figure 5.13(c). The latter therefore corresponds to the results which would be found if the complex array of interfacial tractions just derived was ignored, and a simple 'bearing pressure' approach used. It may be noted that there is no region of tension, for this geometry, implied by either the simplified or corrected solution, and this is typical. Figure 5.13(b) gives a distribution of the maximum in-plane shear stress. This is important as it will also be responsible for propelling any potential cracks, under mode II loading, and, in ductile materials (clearly not glass), it will control the plastic strength of the contact, by Tresca's criterion.

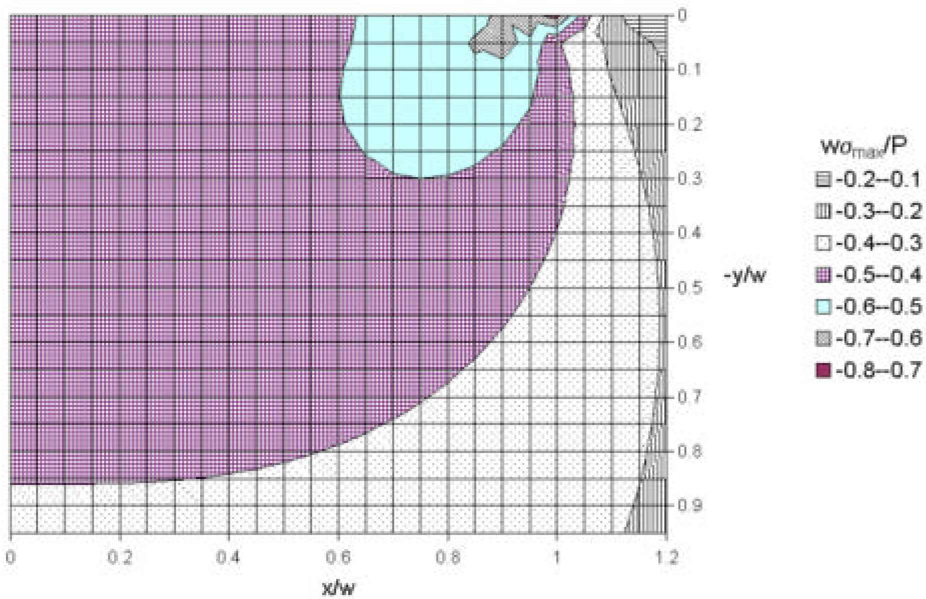

(a)

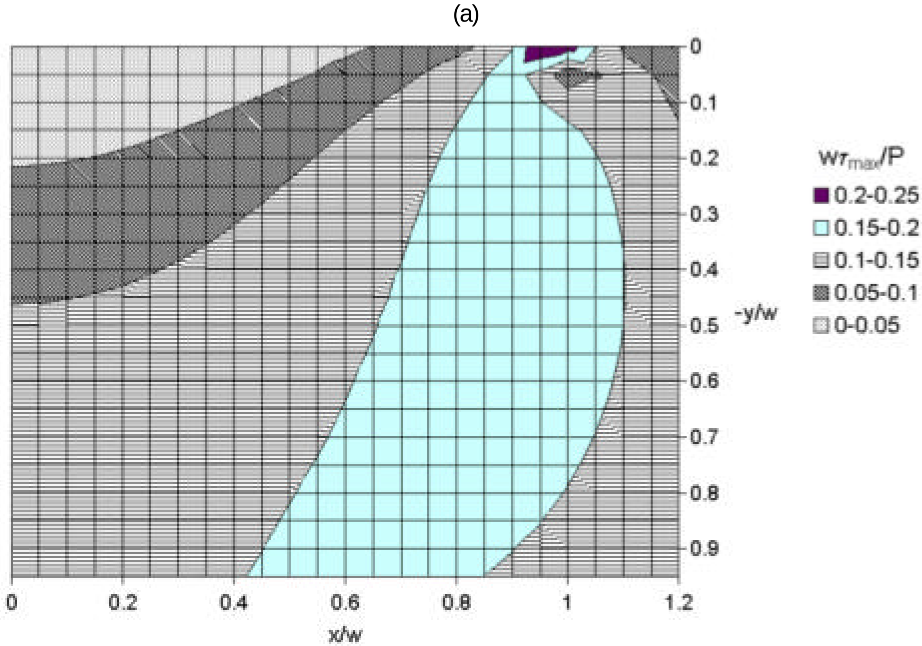

(b)

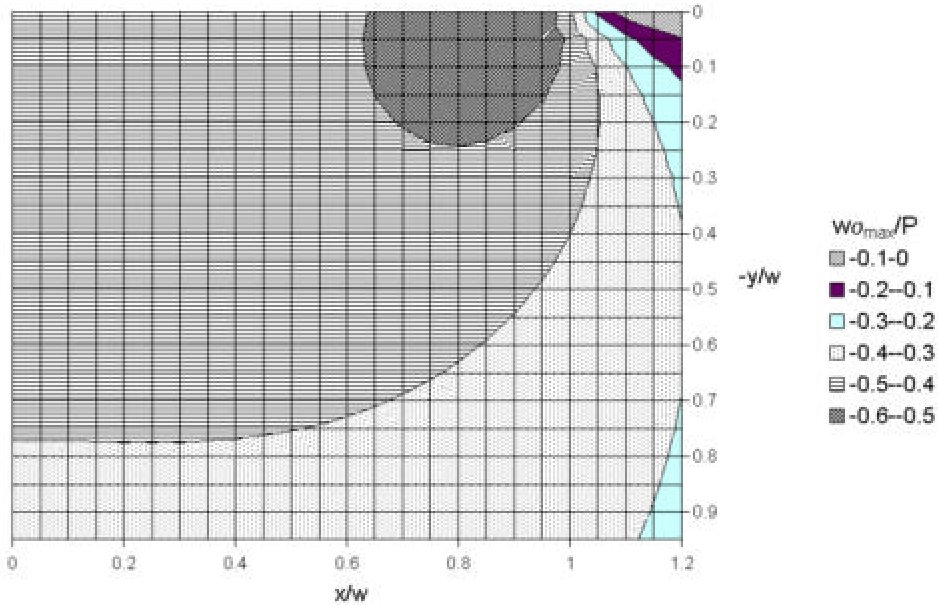

(c)

Figure 5.13 Half plane stresses: (a) s_{max} and (b) t_{max} for the frictional case and (c) s_{max} for the fully lubricated case.

5.7 Mode II stress intensity factors for an edge crack under rigid punch loading

The previous sections have shown that the stress state in the half plane below a rigid punch is compressive everywhere for any frictional condition along the interlayer/half plane interface. In Chapter 4 the possibility of crack propagation in a bulk compressive field was demonstrated, and it was shown that this mechanism was strongly dependent on the mode II stress intensity factor at the tip of an existing crack. In Chapter 4 the applied stress field was uniform and therefore required that the initiating crack be inclined in order for a K_{II} to be induced. Under the contact loading of the rigid punch, non-zero shear stresses are generated along the line of the surface normal ($q_1=0$), and may therefore result in a mode II stress intensity factor at the tip of a crack aligned perpendicular to the surface. As this is thought to be the predominant orientation of edge cracks in structural glass members, this case may be critical to design. Therefore, in this section the mode II stress intensity factor produced at the tip of an edge crack under the contact loading conditions described in the previous section is investigated.

The method used here to calculate K_{II} is the same as that of Chapter 4. The only modification to be made now is to allow for the varying stress gradient over the crack length due to the contact loading field. Therefore, in equation (4.8), the right hand side, which requires the shear stress along the line of the crack in its absence, is evaluated at the individual points, v_k, in the contact loading stress field, rather than being of constant value as it was for the uniform compression. Note that in this section the coefficient of friction between the crack faces in the half plane is assumed to be zero, as this has been shown to result in the maximum stress intensity factors.

It is worth mentioning here an implicit assumption which has been used throughout the development of this rigid punch solution in various forms. It was initially assumed that the shear and normal tractions on the surface of the half plane could be uncoupled, thus allowing the relaxation of shear stresses to simulate finite friction. It was then assumed that the resulting tractions could be applied, unaltered, to the half plane below. In this process there has been an implicit assumption that each stage of the development of the solution has a negligible effect on the preceding stages. That is, the vertical displacements under the rigid punch are still assumed to be constant, or truly reflective of rigid punch behaviour, even though the strict formulation, as such, has not been carried right through the calculation. This is done again here, as it is assumed that the region of slip introduced by the dislocations into the half plane, to model the presence of the crack, will have little effect on the prior parts of the solution, and in particular on the displacement along the top surface of the interlayer. This is justifiable in the present circumstances, as the width of the rigid punch and the depth of the interlayer are both much larger than the length of the introduced crack. However, it is prudent to note that for much larger relative crack sizes the effect of this uncoupled assumption may become much more significant.

Figure 5.14 shows the mode II stress intensity factors for a series of perpendicular edge cracks as function of their position along the top of the half plane. Comparing Figure 5.14 with the plot of the surface shear traction in Figure 5.12, shows the strong dependence of K_{II} on the applied shear stress. The similarity between the curves diminishes as the crack length increases, and is therefore subject to greater variability in shear stress over its length. The figure demonstrates that the mode II stress intensity factor is at its maximum towards the edge of the contact, concomitant with the maximum shearing traction on the half plane surface. Note that the coefficient of friction, f, displayed in the figure relates to the interlayer/half plane interface, not the crack faces, which are frictionless.

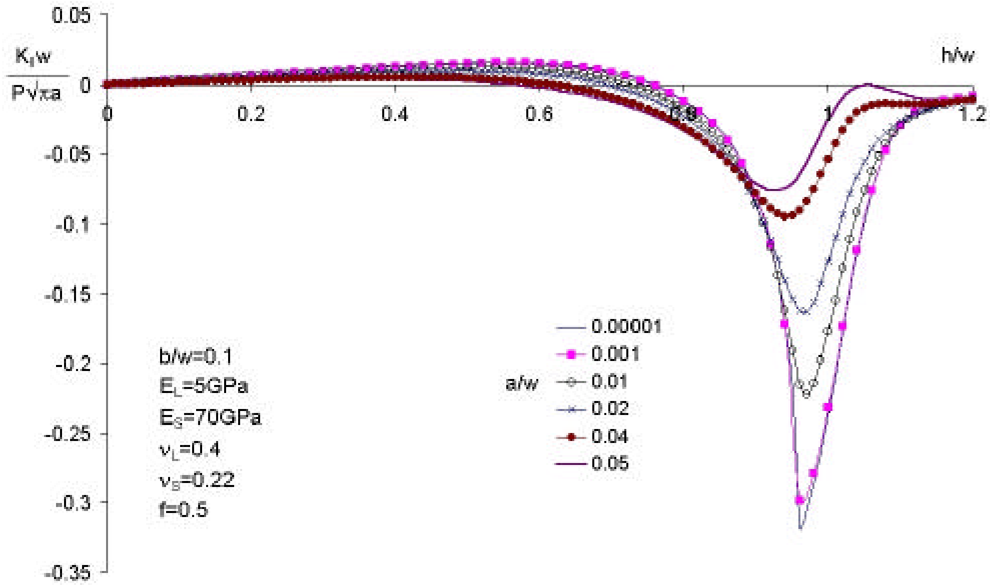

Figure 5.14 Variation in K_{II} with perpendicular crack location and depth

For the case described in Figure 5.14 the maximum surface shearing traction was located at *h/w=0.96*. Figure 5.15 shows the variation in K_{II} of a short crack as its inclination to the surface (θ_1) is varied.

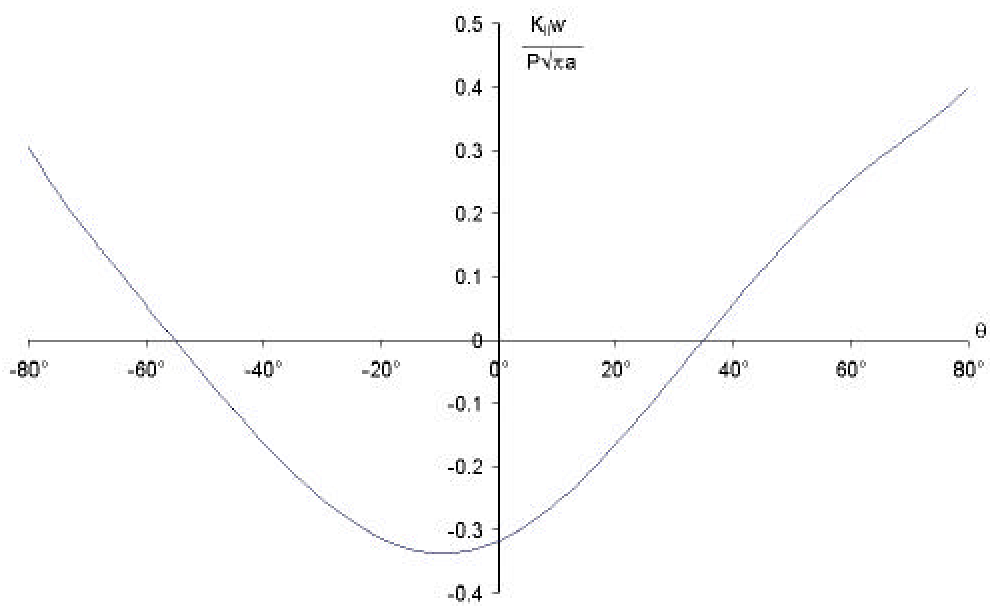

Figure 5.15 Variation of K_{II} with crack inclination

Figure 5.15 shows the maximum K_{II} occurring for a crack inclination of -9 for a short edge crack. The variation in stress intensity factor is now considered as the crack length increases. This is plotted in Figure 5.16 for cracks oriented at -9 and 0 to the surface normal. Note that in this plot the stress intensity factors are normalised with respect to the punch half width, so that comparisons between different length cracks may be made. Interestingly, the figure shows that there is a crack length for which K_{II} is locally maximised. This feature is exploited in the following section, in which the propagation of the initial crack by the kinking mechanism outlined in Chapter 4 is investigated.

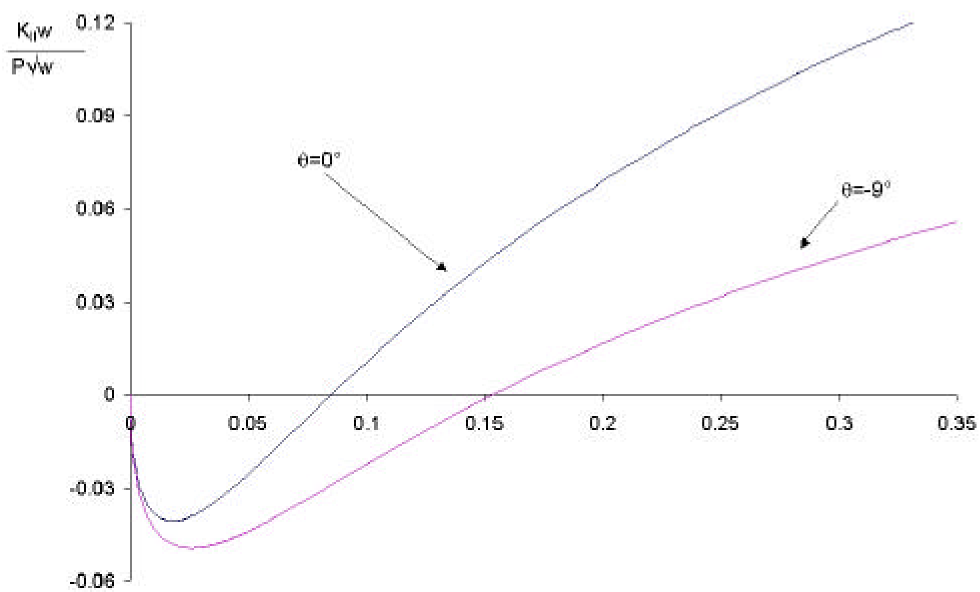

Figure 5.16 Variation in K_{II} as the crack length increases

5.8 Propagation by kinking of an edge crack under rigid punch loading

In Chapter 4 it was established that an edge crack in a compressive stress field could propagate by the mechanism of kinking at the crack tip. In this section this kinking process will be investigated for an edge crack located under a rigid punch which is loading the half plane via an elastic interlayer. The stress state generated for such a case has been developed earlier in this chapter.

It has been established earlier that when a wing crack is small its propagation is dominated by the mode II singular stress field. Hence, the orientation which maximises K_{II} for the straight crack is used as segment 1 for the kinked crack. For the stress state considered in the previous section, Figure 5.16 showed this maximum orientation to be for a straight crack, of length $a_1/w=0.0265$, oriented at –9 to the vertical, located at $h/w=0.96$ from the centreline of the rigid punch. With this crack arrangement set as segment 1 (refer to Figure 4.10 for geometry), the addition of segment 2 is now considered.

The calculation of the stress intensity factors for the tip of the kinked crack (ie. at the end of segment 2) is based on the method outlined in section 4.3. The contact loading is accounted for by evaluating the contact stresses at specific individual points (v_{1k}, v_{2k}) and substituting them into equations (4.29) – (4.31). Results are then forthcoming, and do not require any further mathematical derivation other than that presented in Chapter 4.

Figure 5.17 shows the variation of the segment 2 crack tip stress intensity factors with kink angle, for a series of short cracks. As for the uniform compression case of Figure 4.12, the general form of the mode II singular stress field (given previously in Figure 4.2) broadly corresponds to that shown by the stress intensity factor curves. It is also shown that as the segment 2 length extends, K_I reduces, indicating self-arrest of the wing crack.

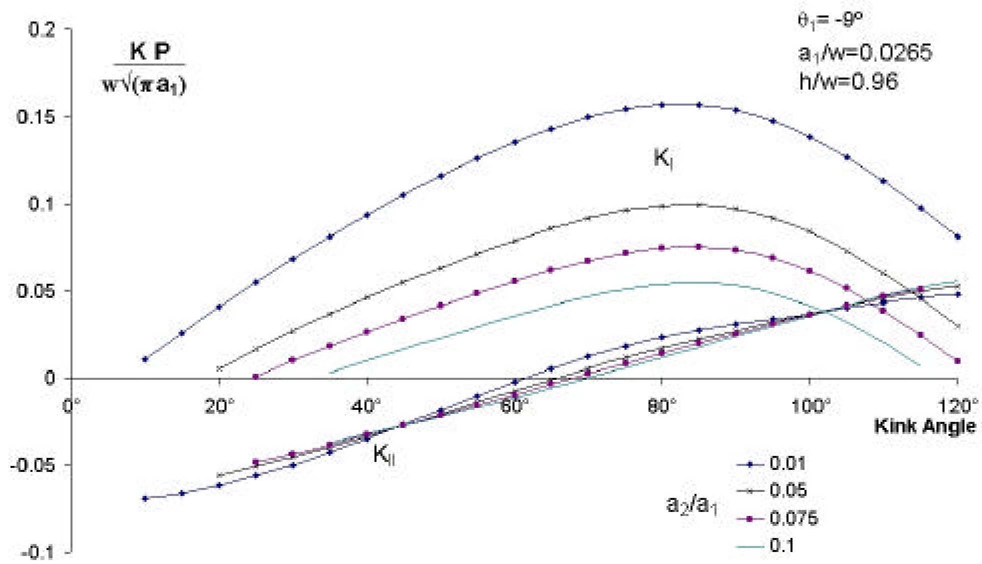

Figure 5.17 Stress intensities at kinked crack tip due to contact loading

Figure 5.18 presents the maximum mode I stress intensity factor with wing crack length. The magnitude of K_I decays more rapidly than in the case given in Figure 4.14, which gives the same plot, but for a uniform compressive applied stress field. This is due to the higher ratio of compressive to shearing stresses on the crack from the contact loading. The rapid variation in orientation of maximum direct and shearing stresses also implies that a kinked crack, in such a field, would be more susceptible to a curving. Hence, the results for the maximum stress intensity factor given in Figure 5.18 could be considered to be a lower bound as the wing crack length increases, and probably curves.

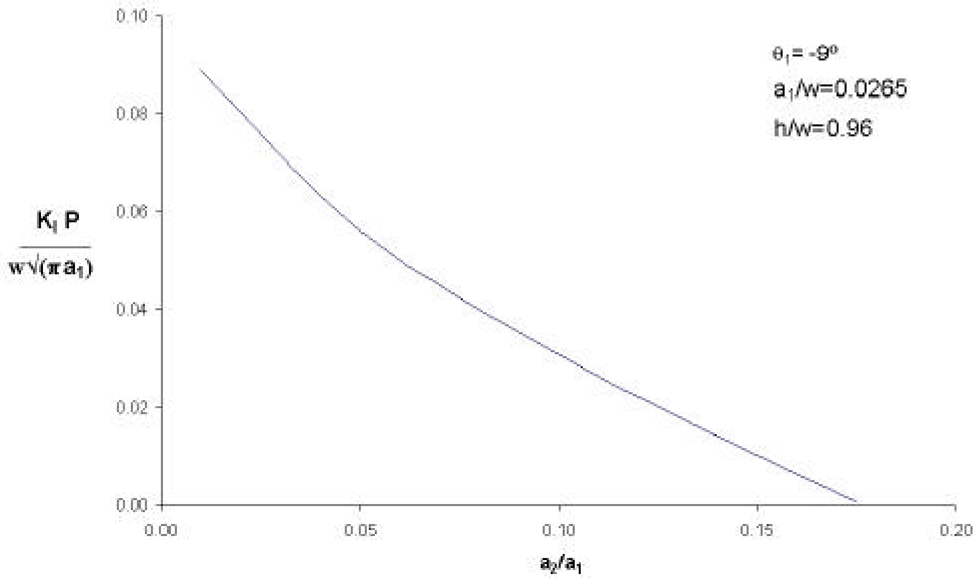

Figure 5.18 Maximum K_I for increasing segment 2 length

5.9 Application of the Crack Size Design method to contact loading

The investigation of contact loading presented in this chapter has shown that the expected zones of tension under the contact do not occur. Instead, it has been demonstrated that wing crack propagation is the probable failure mechanism. Therefore, when trying to fit contact loading of this sort into a Crack Size Design framework, it is more appropriate to base it on the compressive failure method of Chapter 4, rather than the bulk tensile stress approach of Chapter 2.

Figure 5.18 shows a decreasing mode I stress intensity factor with wing crack length, which was a feature found earlier for a kinked crack in a uniform compressive field (see Figure 4.14). In the contact loading case, however, it appears that K_I decays much more quickly with wing crack length. Therefore issues relating to slow crack growth will be less important in a contact loading environment than for uniform compression.

The similarity in kinked crack behaviour between the compression and contact cases means that the Crack Size Design method developed in section 4.5 for the former may be applied, virtually unchanged, to the latter. Therefore, design is carried out so that the stress intensity factor is maintained below that required to induce initial wing crack formation (see equation (4.1)). In fact, the only complexity for contact loading is the determination of the initiating design crack, or the length and inclination of segment 1 of the kinked crack. The inclination should be taken as the angle required to generate the greatest stress intensity factor for the unkinked, initiating crack: -9 in this case.

In the case of a straight crack in a uniform compression field, the mode II stress intensity factor increases with crack length. In design, therefore, a larger design crack implies a greater degree of safety. However, Figure 5.16 showed there to be a local maximum K_{II}, which then decreased with crack length, due to the varying contact stress field. Let us denote the length corresponding to this K_{II} maximum as $a_{contact}$.

In the Crack Size Design method an initial design crack is determined, of length a_0^*. In structural glass applications, the majority of cracks present along the glass edge are smaller than this length. Therefore, if $a_0^* > a_{contact}$ then there will be a higher number of cracks of length $a_{contact}$, all with a higher corresponding stress intensity factor. The design crack, a^*, used in design is therefore defined by the following conditions.

$$a^* = a_{contact}, \text{ if } a_0^* > a_{contact}$$
$$a^* = a_0^*, \text{ if } a_0^* < a_{contact} \tag{5.21}$$

It should be noted that the initiating crack length, a^*, is assumed to be small. Figure 5.16 showed a local maximum where K_{II} was negative, but also indicated an increasingly positive stress intensity factor with crack length. However, it is assumed that the length at which the positive K_{II} becomes equal in magnitude to the negative maximum is too long to be encountered in general structural glass applications.

Chapter 6

Contact between a rigid punch and a half plane via a thin, soft, rigid plastic interlayer

6.1 Introduction

In Chapter 5 the effect of using a linear elastic bearing pad between a rigid punch and a glass half plane substrate was investigated. This investigation was aimed at interlayer materials such as stiff rubbers. In this chapter the interlayer is considered to be rigid plastic, to account for other commonly used bearing materials, such as aluminium or lead.

Ductile materials, such as pure lead or aluminium, are often used in connections as interlayers to distribute contact loading benignly (Kelly *et al.*, 1992). The interlayer is designed to reach its limit state and flow plastically, so limiting the adjacent stress state in the half plane to a safe level. However, although such interlayers serve admirably the function of removing local stress raisers associated with imperfection in surface finish, they may introduce local shearing tractions consistent with plastic flow and the attainment of the limit state, and these, in turn, may induce important local tension.

In this chapter, cases of transverse plane strain and stress are investigated. The scenario of a glass block being loaded by a square column, shown in Figure 6.1(a), approximates a case of plane strain. It may be noted that on the centrelines of the column there will be no normal displacement, from symmetry, and therefore, the solution will hold approximately along planes containing these lines. A more general physical arrangement that results in plane strain conditions is given in Figure 6.1(b), where the components of the geometry are long in the *z*-direction. Note that in these cases of plane strain the glass substrate is a half space, rather than a half plane. In the analysis a two dimensional plane through the three dimensional geometry is considered, to provide a half plane formulation. Figure 6.1(b) shows that the geometric requirements for plane strain are not strictly applicable to structural glass applications, as the general form of construction is with plate glass elements. The plane strain solution, nevertheless, provides a rigorous solution to the contact problem, and a good insight into the nature of contact loading problems with ductile interlayer materials. The case of transverse plane stress, shown in Figure 6.1(c), is described later in the chapter.

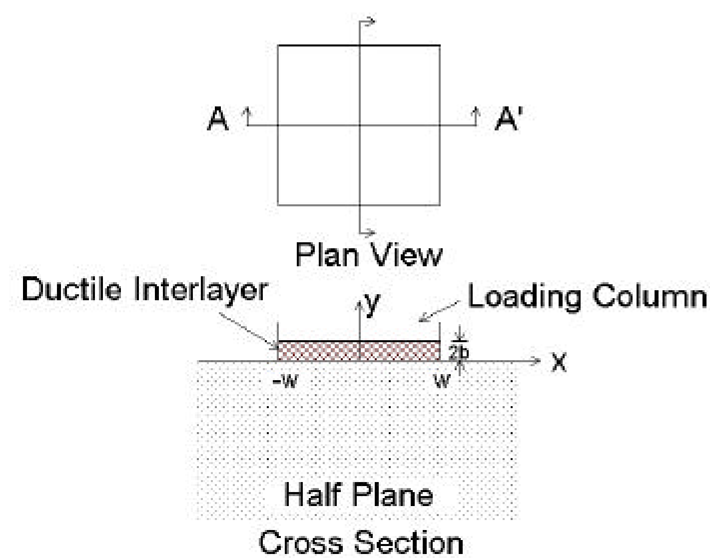

(a)

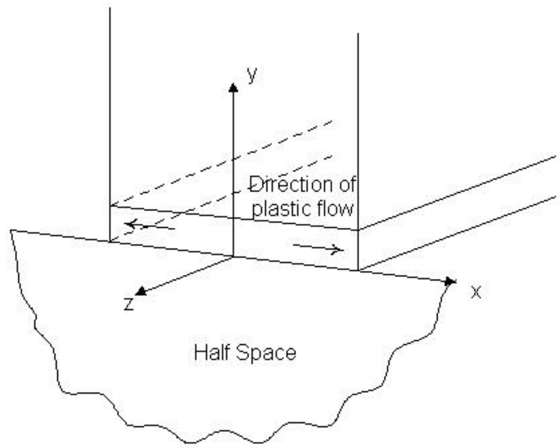

(b)

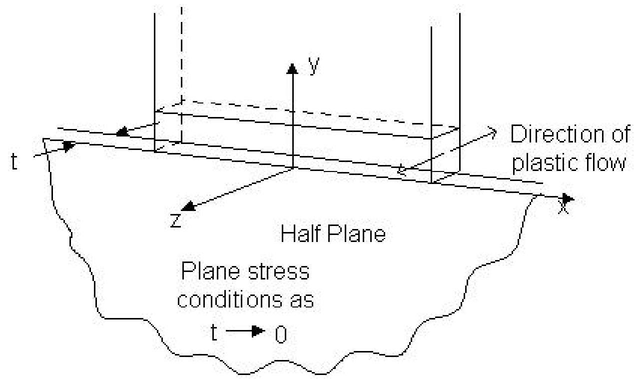

(c)

Figure 6.1 Geometry of the problem. (a) column, (b) plane strain, (c) plane stress

6.2 Formulation for plane strain: Slip line field

The solution developed here is for a half plane in the plane strain problem, such as for section AA' in Figure 6.1(a), or plane xy in Figure 6.1(b). It is assumed that the elastic half plane and punch are much stiffer than the ductile interlayer. This is easy to justify if they remain within the elastic regime, whilst the interlayer attains a limit state. The solution for the slip line field thus becomes the classical one of compression of a strip between two rigid platens (Johnson & Mellor, 1962).

If contact between the interlayer and adjacent contacting elements is frictionless, the contact pressure is simply limited to the uniaxial yield stress, as no direct stress develops parallel with the interface (x-direction, Figure 6.1(a)). However, in practice this is unlikely to be physically reasonable, as slip will arise, resisted by friction. Here, it will be assumed that the contact pressure and coefficient of friction are both sufficiently high for the yield condition to be attained at the interface before slipping occurs. If the coefficient of friction were modest, or in regions where the contact pressure is low, Coulomb friction may be the limiting factor, but this is not considered here. It is initially assumed that the interfaces are "perfectly rough" so that the shear yield strength of the interlayer, k, can be attained along the entire interface. The minimum normal contact pressure occurs at the edges of the contact, as will be shown later, and this is therefore the point where slipping between the interlayer and its contacting components occurs first. By taking the ratio of the shear to normal tractions at the edge of the contact, the minimum coefficient of friction, f, required to ensure full adhesion to develop may be found. It was given by Alexander (1955), and it can easily be shown, that this minimum is f=1/(1+π/2)=0.389. This is therefore the minimum value for which the solution to be developed is rigorous, and is a realistic figure which may normally be expected to arise under conditions of very high contact pressure, and with a soft material.

The contact pressure distribution was determined based on the method outlined by Johnson & Mellor (1962) and, as it is well known, only elements of the solution are given here. This is a piecewise step method, originally implemented using a graphical approach, which approximates a true slip line field by straight line segments. It relies on the systematic development of pseudo-squares between the two orthogonal families of slip lines, such that, along all free boundaries the zero traction or perfect stick conditions are met, and internally the net developed is the best approximation to a true, infinitesimal slip line field. Construction of the slip line approximation begins at the free edge of the pad, with a 45° fan being divided equally into n portions, as shown in Figure 6.2, which represents the top quarter of the interlayer. The higher the value of n, the greater the accuracy of the solution. In early texts, for example Johnson & Mellor (1962), where an actual graphical method is employed, n is often 5 or less, and so the ratio of the pad width ($2w$) to height ($2b$) which may be treated with confidence is also small, generally not exceeding 10. Automated methods of developing the net permit much larger values of n to be used, and therefore much larger values of w/b, or increasingly thin pads, to be treated accurately. Normal and tangential intersection of the two families of slip line with the 'platens' indicates full adhesion along this interface, while the 45° angle with the interlayer centreline indicates the absence of shear along this line. Up to $w/b=3.64$, denoted by the heavy line in Figure 6.2, the net is formed from the original fan. For higher values of w/b the net develops in a way which is very nearly self similar. The results displayed could, of course, be used for any value of w/b in the range $3.64 \leq w/b \leq 5.56$.

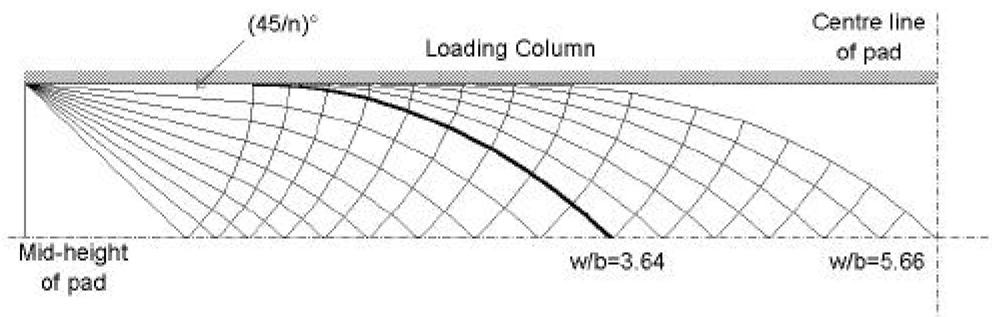

Figure 6.2 Slip line field for one quarter of the interlayer.

6.3 Plane strain results

6.3.1 Traction distribution

From the slip line field the contact pressure may be determined, using standard principles (Johnson & Mellor, 1962). Typical contact pressure distributions, for *3.64 £ w/b < 12.05* are given in Figure 6.3, and indicate the general form of the traction profile. The steps in the contact pressure, p/k, are $1+p/2$ at $x/w = \pm 1$, and about 1.1 adjacent to the central region. The central region of constant stress indicates a rigid portion of the interlayer, where the yield condition is not attained. The figure also indicates the shear traction distribution. This is limited to the yield stress in pure shear in the flow regions, whilst in the central region it is formally hyperstatic. However, the distribution clearly must be anti-symmetric, and since this hyperstatic region is small compared to the width of pad being considered, a linearly varying shear stress is assumed to be satisfactory.

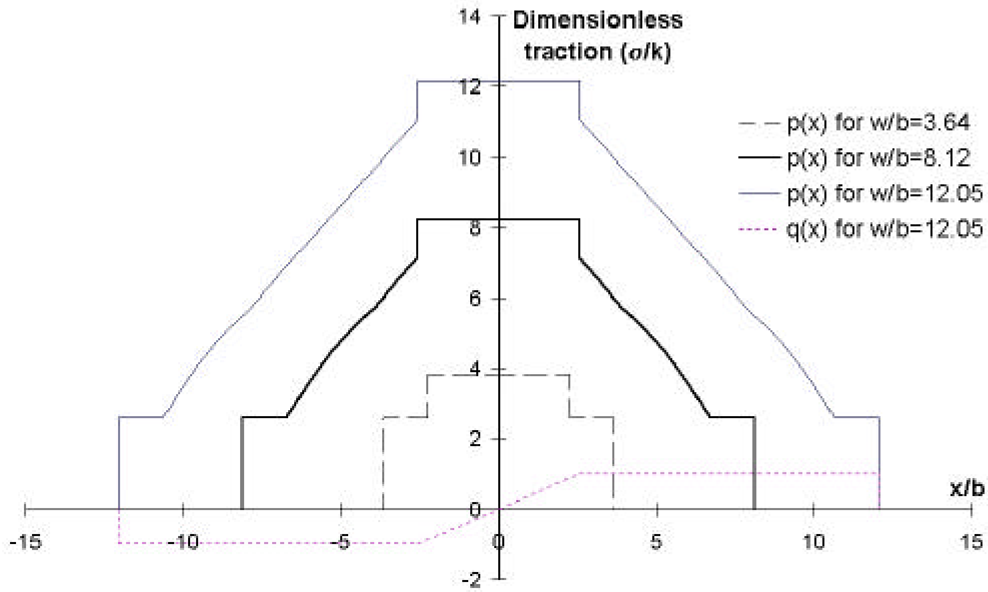

Figure 6.3 Contact traction distributions

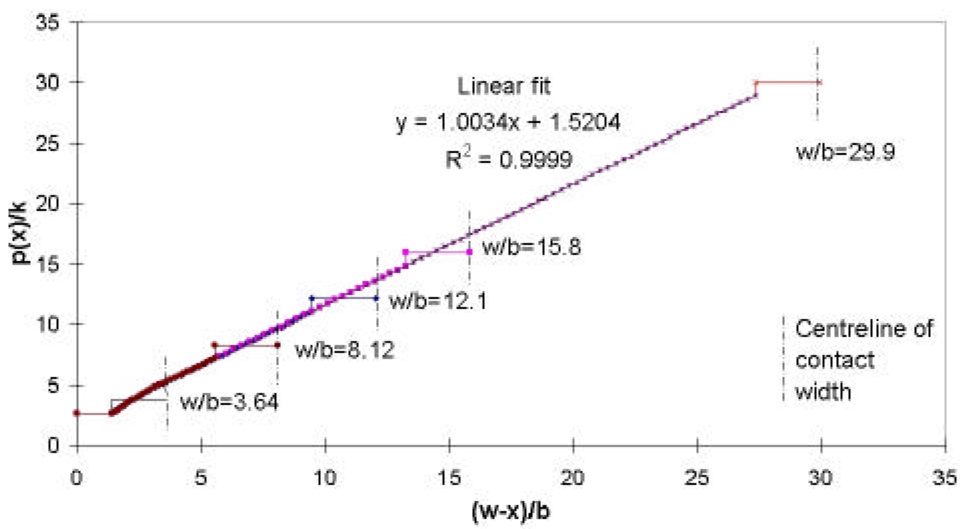

Figure 6.4 Summary of contact pressure distribution for any aspect ratio.

The contact pressures shown for representative cases in Figure 6.3 are summarised in Figure 6.4, in a form which enables the pressure for a wide range of interlayer aspect ratios to be found. The contact pressure distribution over the slip region is extremely close to a straight line, and a best-fit equation, which is more than adequate for practical purposes, is given on the figure. The length of the central rigid zone is constant, so that a simple closed-form expression for the contact pressure may be found:

$$
\begin{aligned}
\frac{p(\hat{x})}{k} &= -2.57 && \hat{w}-\sqrt{2} < |\hat{x}| \le \hat{w} \\
\frac{p(\hat{x})}{k} &= -[1.0034(\hat{x}+\hat{w})+1.5204] && -\hat{w}+\sqrt{2} \le \hat{x} \le -2.57 \\
\frac{p(\hat{x})}{k} &= -(1.0034\,\hat{w}+0.031662) && |\hat{x}| \le 2.57 \\
\frac{p(\hat{x})}{k} &= -[1.0034(\hat{w}-\hat{x})+1.5204] && 2.57 \le \hat{x} \le \hat{w}-\sqrt{2}
\end{aligned}
\qquad (6.1)
$$

where $\hat{x} = x/b$, $\hat{w} = w/b$ and k is the yield stress in pure shear.

The shear traction distribution over the interface is taken as

$$
\begin{aligned}
\frac{q(\hat{x})}{k} &= -1 && -\hat{w} \le \hat{x} \le -2.57 \\
\frac{q(\hat{x})}{k} &= \frac{\hat{x}}{2.57} && |\hat{x}| \le 2.57 \\
\frac{q(\hat{x})}{k} &= 1 && 2.57 \le \hat{x} \le \hat{w}
\end{aligned}
\qquad (6.2)
$$

The tractions given in equations (6.1) and (6.2) hold for $w/b \ge 3.61$. If $w/b < 3.61$ a completely different form of the slip line field arises, but this is not of practical relevance in the present context of a thin pad. Lastly, note that for higher ratios of *w/b*, the flat portions of the traction plot at the ends and centre of the contact become insignificant compared to the linear region and the pressure distribution takes on a triangular form.

6.3.2 Internal stress distribution

Whilst the interlayer is in a plastic limit state, the contacting material - the glass block in the present context - remains entirely elastic. As stated at the outset, the intention in the present study is to investigate the possibility of brittle fracture, and hence the internal stress state is needed in detail. This may be found by idealising the glass block as a half plane, and employing the well known Muskhelishvili potential method, as described by Hills *et al.* (1993). The potential is evaluated at any point in the half space, $\hat{z} = \hat{x} + i\hat{y}$, from the following

$$f(\hat{z}) = \frac{1}{2pi} \int_{contact} \frac{p(t) - iq(t)}{t - \hat{z}} dt \tag{6.3}$$

where t is a coordinate lying in the surface of the half plane, and $q(t)$ is the surface shear traction. Substituting the traction distributions of equations (6.1) and (6.2) into equation (6.3) gives the following explicit formula for the potential:

$$\begin{aligned} \frac{-2pi}{k} f(\hat{z}) = {} & 2.57\left[\ln\left(\frac{\hat{w} - \sqrt{2} + \hat{z}}{\hat{w} + \hat{z}}\right) + \ln\left(\frac{\hat{w} - \hat{z}}{\hat{w} - \sqrt{2} - \hat{z}}\right)\right] \\ & + (1.0034\hat{w} + 1.5204)\left[\ln\left(\frac{2.57 + \hat{z}}{\hat{w} - \sqrt{2} + \hat{z}}\right) + \ln\left(\frac{\hat{w} - \sqrt{2} - \hat{z}}{2.57 - \hat{z}}\right)\right] \\ & + 1.0034\hat{z}\left[\ln\left(\frac{2.57 + \hat{z}}{\hat{w} - \sqrt{2} + \hat{z}}\right) - \ln\left(\frac{\hat{w} - \sqrt{2} - \hat{z}}{2.57 - \hat{z}}\right)\right] \\ & + (1.0034\hat{w} + 0.031662)\ln\left(\frac{2.57 - \hat{z}}{-2.57 - \hat{z}}\right) \\ & + i\left[\ln\left(\frac{\hat{w} + \hat{z}}{2.57 + \hat{z}}\right) + \ln\left(\frac{\hat{w} - \hat{z}}{2.57 - \hat{z}}\right) + \frac{\hat{z}}{2.57}\ln\left(\frac{2.57 - \hat{z}}{-2.57 - \hat{z}}\right) + 2\right] \end{aligned} \tag{6.4}$$

Although this formula is lengthy, the explicit potential makes it possible to determine closed form expressions for the half plane stresses, and obviates the need for a numerical technique. It is therefore computationally efficient. Routine procedures, described explicitly by Hills *et al.* (1993), enable the internal stress state to be found.

6.3.3 Surface stress state

It has been shown in Chapter 2 that the critical cracks occurring in structural glass applications are located on the glass surface. Thus, although the Muskhelishvili potential may be used to determine the stress field for the entire half plane, attention is focused on the surface. The solution is split into two parts. First, the σ_{xx} stress associated with surface shear traction, given by the final term on the right hand side of equation (6.4), is shown in Figure 6.5, for two representative aspect ratios. The curves show an area of tension produced at the centre and confirm the assumption that the outward flow of material generates a local tension effect. As the contact width increases the magnitude of the central tensile stress also increases.

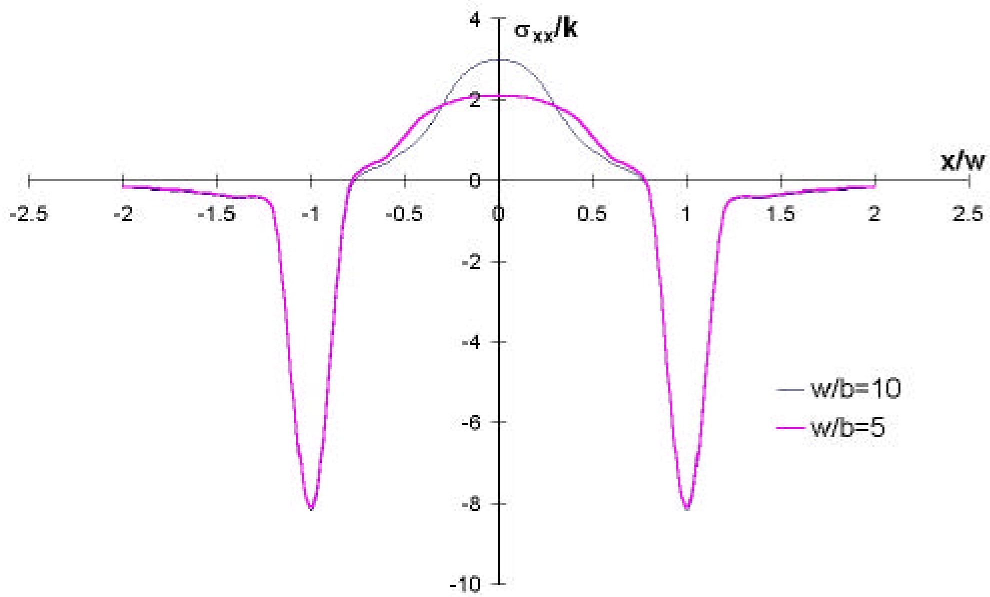

Figure 6.5 Surface tension associated with shear traction.

It has been shown that the presence of the shearing traction alone induces tension at the centre of the contact area. The stress parallel with the surface (σ_{xx}) due to the normal pressure, and the normal pressure itself, take the same numerical value for any pressure distribution over the surface of the half plane, and hence may be found directly from Figures 6.3 and 6.4. The combined effect of the tractions is displayed in Figure 6.6, and indicates that there is *no* central tension produced, and this is indeed the case for all pad aspect ratios. The dip in the compressive stress at the centre is caused by the surface shear traction, but it is found that the compression caused by the pressure dominates the problem. The central compression increases in magnitude with increasing pad aspect ratio, because the central contact pressure itself increases, while the shear traction is limited to the shear yield stress, k.

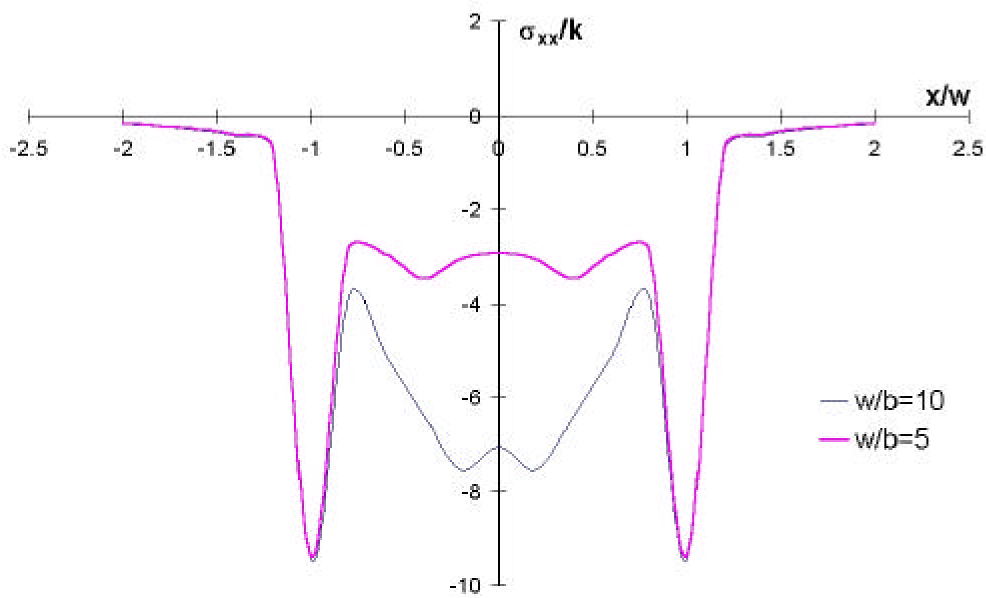

Figure 6.6 Resultant surface in-plane direct stress

6.4 Attainment of the limit state avoids tension

It has been shown that there is never any tension induced on the surface at any point, *providing that the limit state is attained.* The main practical import of this result is the need to match the design of the interlayer with the material very carefully. The solution developed does not apply if the interlayer does not achieve a true limit state, and hence it is essential to ensure that the initial thickness of the interlayer is sufficiently high for plastic flow to occur. This is easy to determine by integrating the normal pressure distribution along the interface and equating it with the total load, P, as shown in Figure 6.7. In order to use this figure in a practical design, it is simply necessary to ensure that the combination of load, pad aspect ratio and interlayer yield strength is such that the point representing this combination initially lies to the right of the line shown in the Figure 6.7. Plastic flow will then occur so as to reduce the height, b, and hence to move the point towards the limit state line. On the other hand, the initial thickness should not be too great, or the amount of 'settling' which accompanies plastic flow will be undesirable.

If the initial thickness of the interlayer is too thin, so that full plasticity is not achieved, there can be no assurance that local tensions will not arise.

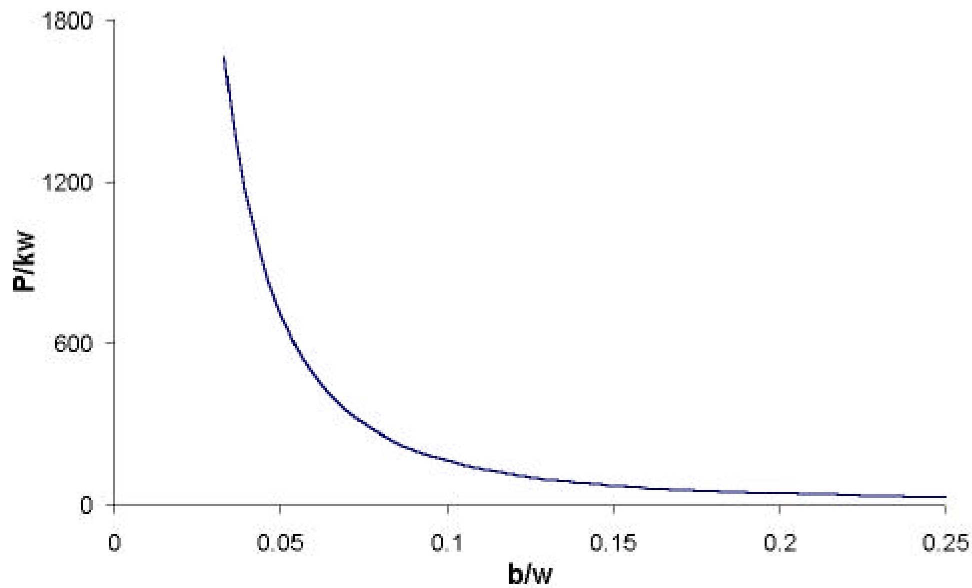

Figure 6.7 Geometry of problem and its effect on the limit state

6.5 Edge cracks exposed to rigid punch loading under conditions of plain strain

For a material which fails due to bulk tension alone, the satisfaction of the conditions outlined in the previous section are sufficient to provide a safe design. However, it was shown in Chapter 4 that, even in the absence of bulk tension, glass failure may still occur as a result of shearing stresses on edge cracks. In this section and the next, the possibility of such a failure is investigated for the contact loading via a rigid plastic punch, described above.

The solution to the rigid plastic interlayer problem given earlier in the chapter is in transverse plane strain. The half plane formulation was presented as a slice through a larger three dimensional problem. Hence, it is important to note that the cracks considered in the forthcoming sections are also three dimensional in nature. They contrast with the cracks considered in Chapters 2 and 4, which were assumed to be uniform in length over the glass plate thickness. Here it is assumed that the cracks extend in a homogeneous manner all the way along the *z* axis, or that they are sufficiently long that their finite dimension in the *z* direction does not greatly impact upon the solution for a half plane intersecting at some point in the middle of the crack.

Chapter 4 demonstrated that the mode II stress intensity factor at the tip of a crack in a compressive field governs initial wing crack propagation. A study is undertaken here to investigate this stress intensity for a straight crack in the compressive field generated by the contact loading given previously in the chapter. The calculation of K_{II} follows the same method as that outlined in section 4.2, the only difference being that the applied stress field [$s_S(v_k)$ and $s_N(v_k)$, of equation (4.8)] is evaluated using the stress field for the rigid punch problem being considered here. Note that the crack faces are assumed to be frictionless.

Exhaustive results for a wide range of pad aspect ratios are not given, as the primary interest in this section is the investigation of compression failure as a mechanism. Hence, the results presented below all correspond to a pad aspect ratio of *w/b=8.12.* Figure 6.8 shows results for a crack oriented perpendicular to the surface, as this is the dominant inclination expected in practice. It shows the mode II stress intensity factor as a function of location, with respect to the punch width, and for a series of crack lengths.

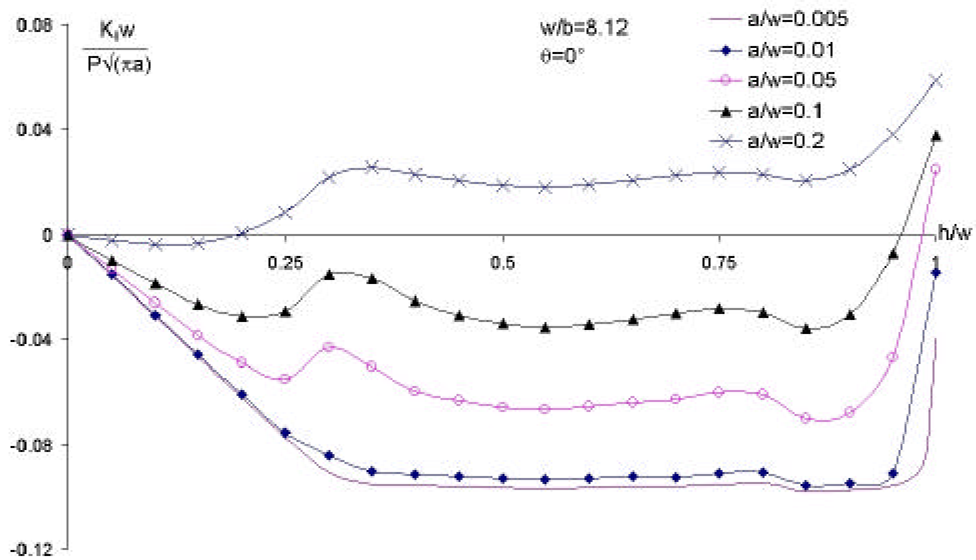

Figure 6.8 Mode II stress intensity factors with location for a perpendicular crack, of various lengths

The maximum *magnitude* of the stress intensity factor (negative in this case) for each curve in Figure 6.8 occurs at about *h/w=0.86.* Recall that this was for a crack oriented perpendicular to the surface. In Figure 6.9 the variation in stress intensity with crack inclination from the surface normal is presented. It shows the maximum K_{II} to correspond to a crack inclined at 8 to the normal.

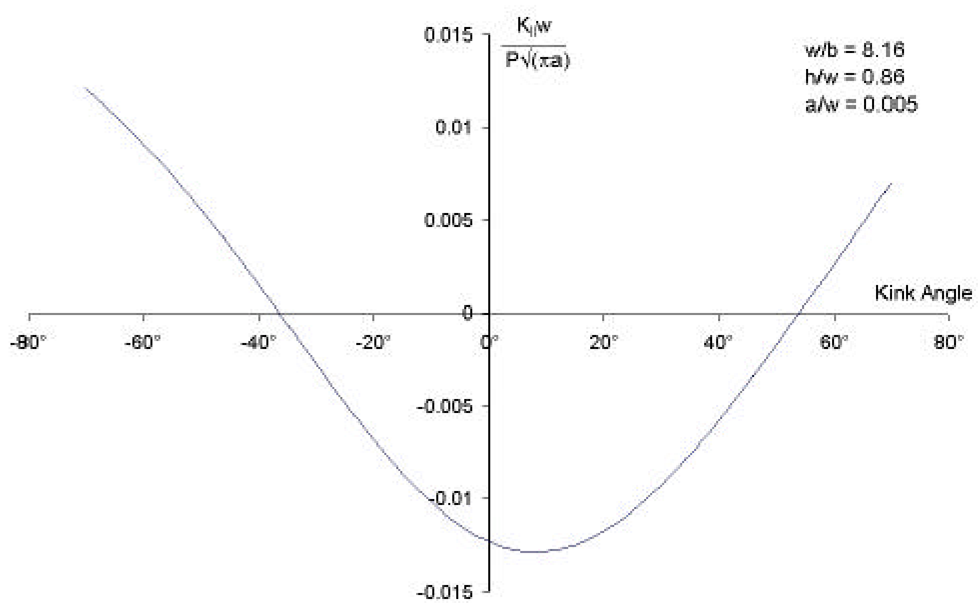

Figure 6.9 Variation in K_{II} with crack inclination

Figure 6.8 shows the stress intensity factor normalised with respect to the crack length and Figure 610 gives alternative plots of K_{II} normalised with respect to the punch width. This means that the effect of crack length is easier to appreciate. The results are for both a perpendicular crack and one inclined at 8 to the surface normal. It can be seen that K_{II} for the inclined crack is consistently greater than that of the normal crack, and peaks for a crack length of approximately *a/w=0.05*.

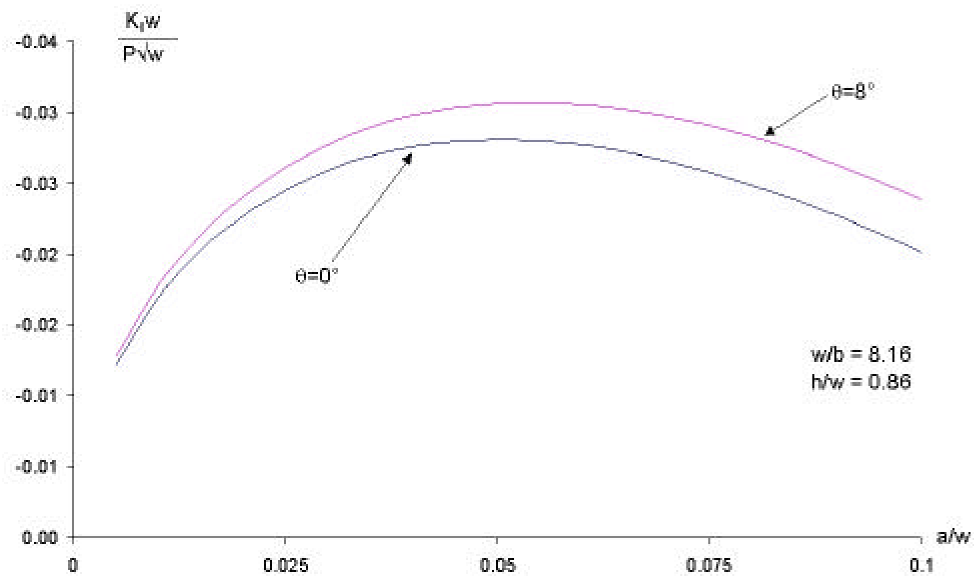

Figure 6.10 K_{II} with crack length for perpendicular crack (*q=0*) and maximum K_{II} orientation (*q=8*)

6.6 Kinked cracks under plane strain loading conditions

In the previous section the maximum K_{II} for an edge crack in a half plane subjected to rigid punch loading via a plastic interlayer was presented. Growth from the end of the straight crack by the wing crack mechanism described in Chapter 4 is considered here. As initial propagation is dominated by the mode II stress intensity factor, the crack which results in the maximum K_{II} is set as segment 1 in the following analysis, which follows that of section 4.3.

Figure 6.11 shows the stress intensity factors at the wing crack tip, as a function of kink angle, for a series of segment 2 lengths. As expected, the curves for small wing crack lengths reflect the general form of the mode II singular stress field. Also, the magnitude of the K_I plot reduces as the segment 2 length increases, indicating self-arrest as the wing crack propagates. The maximum values of K_I, versus the wing crack lengths for which they occur, are presented in Figure 6.12.

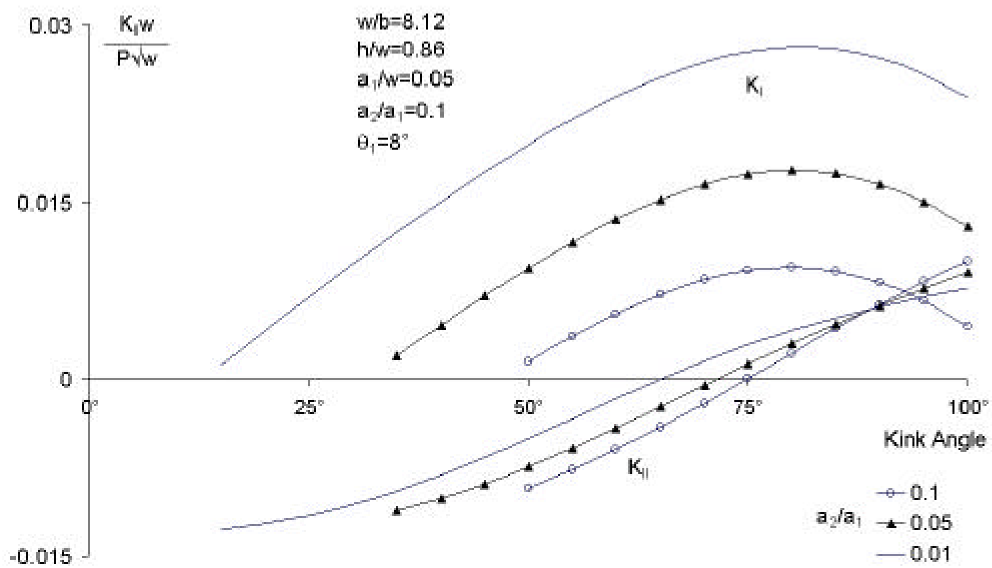

Figure 6.11 Stress intensity factors with kink angle

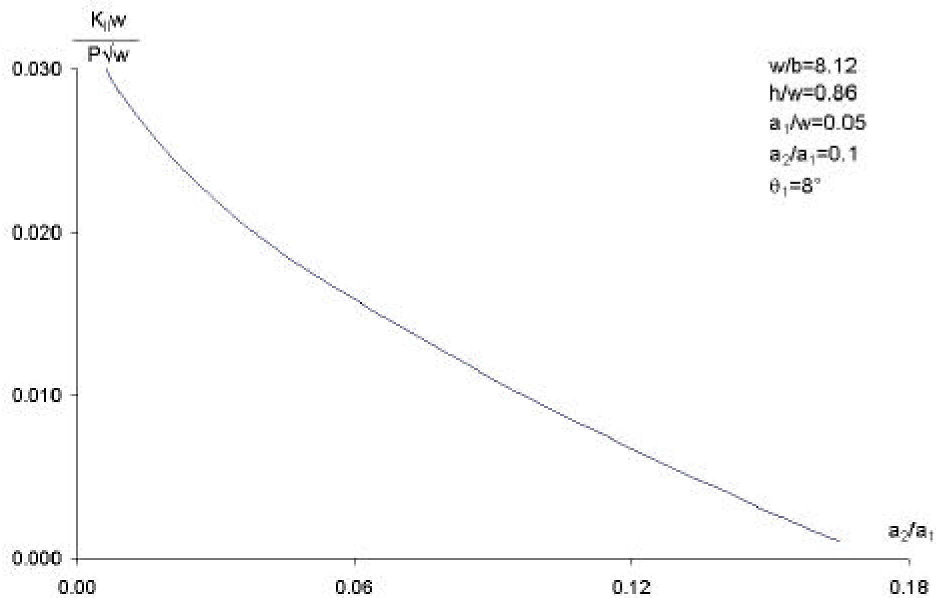

Figure 6.12 Maximum mode I stress intensity factor with wing crack length

6.7 Formulation for plane stress

Consider, now, a plate of glass being loaded on its edge, as shown in Figure 6.1(c). As the plate thickness is reduced, the degree of transverse constraint (along the z axis) also reduces. For a thin plate, the displacements of the pad in the x direction will be negligible compared to those in the z direction, due to the proportionally greater x direction constraint, resulting in plane stress conditions. In this case, the pad material flows across the plate, in the yz plane, rather than in the xy plane, as in plane strain. The result is a differing traction profile imparted to the glass. As the loading is now in plane stress, the direct traction on the glass surface in any xy plane is constant. Equally, as any displacements in the x direction on the glass surface are vanishingly small, the shearing tractions in this direction are insignificant. The rigid plastic tractions given in Figure 6.3 are now representative of the new tractions produced across the glass plate, in the yz plane, which are slightly different due to the new geometry.

Of particular interest in the plane stress loading arrangement is the generation of tensile stresses in the centre of the plate thickness due to the spreading of the pad. However, Chapter 2 demonstrated that the predominant cracks in structural glass applications are *across* the glass thickness, and therefore perpendicular to any of the tensile stresses proposed here. In addition, the shear stresses are self-equilibrating, and, due to the thinness of the glass, will have little global impact on the stress state. Therefore, only the tractions in the xy plane will be considered. It has been stated that the direct traction will be uniform along the pad length, but it will not be of constant magnitude across the width of the glass. For example, the direct stress on the plane of $z=0$ will be greater in magnitude than that on the plane $z=0.25t$ (where these dimensions were defined in Figure 6.1). In later sections, the fracture mechanics of a crack present in the plane stress contact stress field will be investigated. The cracks analysed extend across the whole thickness of the glass, and will therefore lessen the effect at the crack tip of this contact stress variation across the width. Therefore, it will be assumed, for this analysis, that the normal traction is evenly distributed over the loaded area, and is of magnitude p_0 (per unit area), and that the shear tractions are zero. Loading of this sort corresponds to the many approaches often taken in engineering practice to bearing connection design, and therefore has a more general relevance.

The stress field generated in a half plane by a uniform normal stress traction is well documented (Hills *et al.*, 1993), and has been shown to be compressive at every point in the half plane. Therefore the problem of compressive failure is again encountered. Results for a straight, and then kinked, crack in such a stress field are therefore given in the following sections. Solution of the fracture mechanics problem is again performed using the techniques outlined in Chapter 4 (sections 4.2 and 4.3). As for the plane strain solution given earlier in the chapter, the only modification required is a variation in the stress field component of equations (4.11) and (4.29) – (4.31). In this case these values come from the standard solution for a half plane loaded by a uniform pressure, p_0, over the interval $-1 \leq x/w \leq 1$ (Hills *et al.*, 1993).

6.8 Results for a straight crack under plane stress loading conditions

In Section 6.5 results for a straight edge crack in a half plane subjected to contact loading from a rigid plastic interlayer under plane strain conditions were presented. Similar results are presented in this section, but in this case the geometry is assumed to be under conditions of plane stress, as discussed in the previous section.

Figure 6.13 shows the variation in the mode II stress intensity factor at the tip of a crack perpendicular to the half plane edge as a function of its location. It is clear that the maximum occurs when the crack is located at the edge of the loading width (*h/w=1*). It is worth noting here that the half plane stress field, in the absence of the crack, is singular at this point. However, numerical problems are avoided in the calculation of the stress intensity factor through the quadrature being used. The collocation points (v_k) are distributed along the crack so that the stress at the half plane surface need not be evaluated. Therefore, provided the crack is not so short that collocation points towards the crack mouth are highly influenced by the singular stress field, the calculation may continue unaffected.

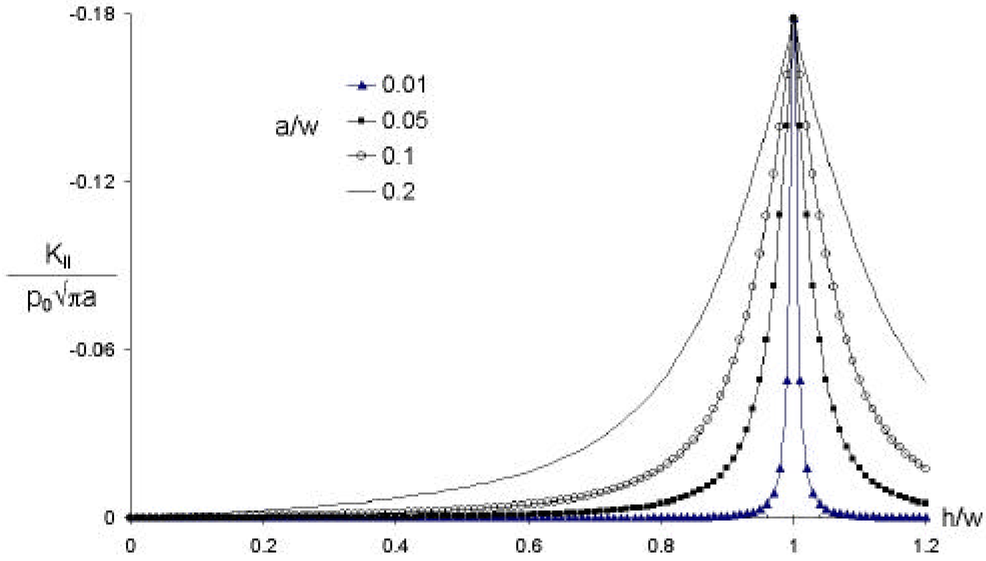

Figure 6.13 Results for a perpendicular crack along edge

Figure 6.13 demonstrates that the edge of the contact loading is the critical location for the stress intensity factor. Figure 6.14 presents the variation in K_{II} with crack inclination for a crack inserted at this critical position. It shows that the maximum magnitude of K_{II} occurs at an inclination of -3 .

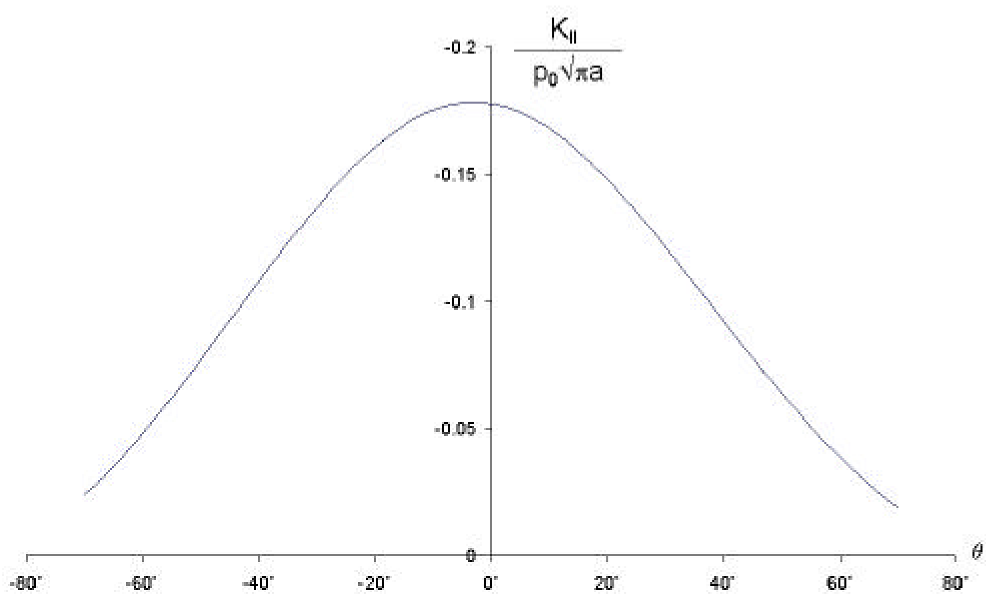

Figure 6.14 K_{II} with inclination for *h/w=1, a/w=0.2*

Although the maximum K_{II} is achieved through placing the crack at the contact edge, it is also interesting to note the variation in the stress intensity factor for a crack located elsewhere under the applied traction. Figure 6.15 gives the variation in the mode II stress intensity factor with crack inclination for a centrally located crack. As the shear stress along the line $h=0$ is zero, the shearing stresses induced along the crack are dominated by the direct stresses resulting from the uniform applied traction. Therefore, Figure 6.15 displays a sinusoidal trend, reflecting the variation in shear stress produced along the line of the crack by a uniform, vertical stress.

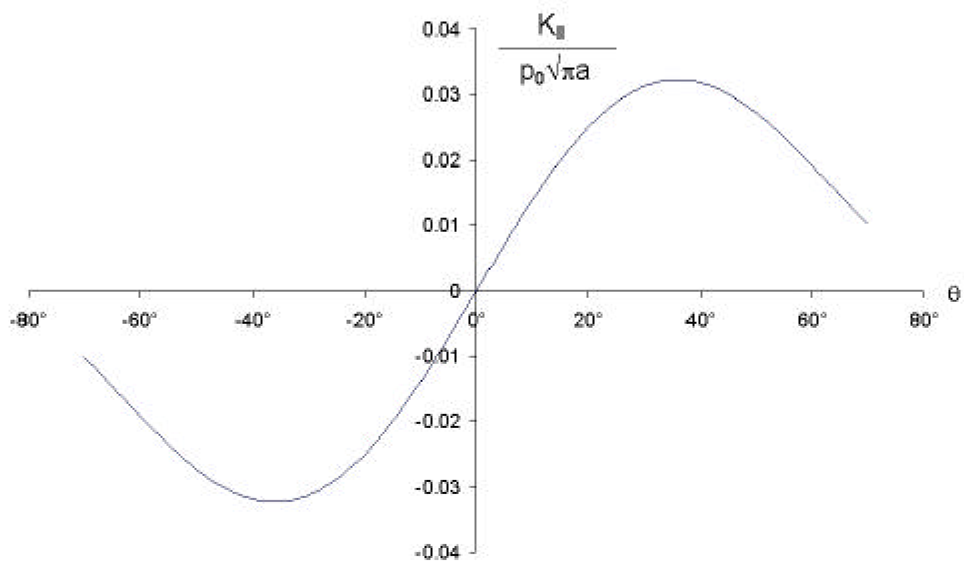

Figure 6.15 K_{II} with inclination for $h=0, a/w=0.2$

Consider, now, the mode II stress intensity factor at the tip of a crack located at the edge of the contact loading area ($h/w=1$) as its length increases. This is plotted in Figure 6.16 for both a perpendicular crack, and one inclined at –3 to the surface normal. It is interesting to note that, unlike other such plots for different contact loading regimes (see Figures 5.16 and 6.10), K_{II} continually increases in magnitude. This behaviour is more typical of fracture mechanics problems, where stress intensities are generally proportional to the square root of the crack length. It is also worth noting that the two curves in Figure 6.16 are virtually identical, showing that a perpendicular crack may be taken as the critical one in design without significant loss in accuracy.

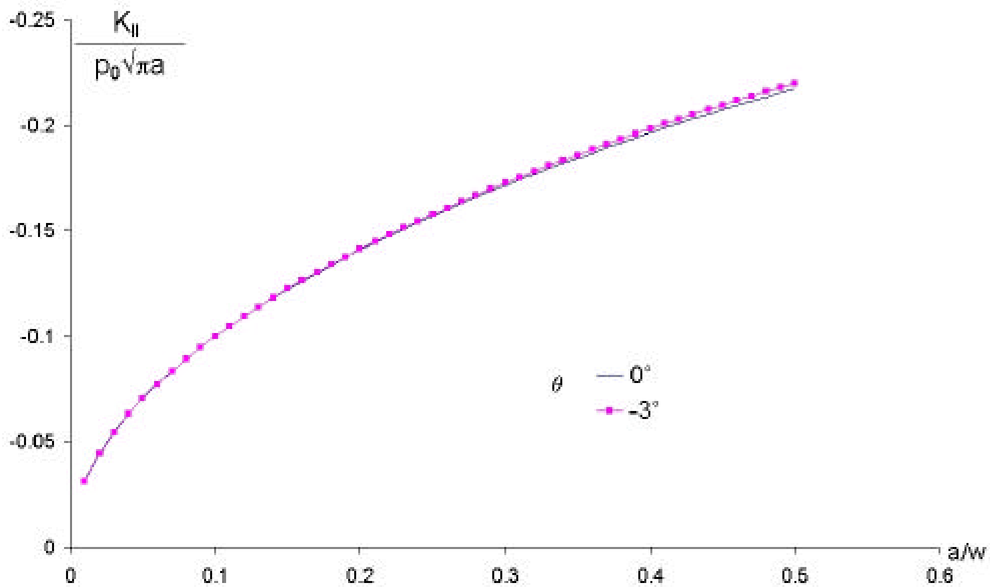

Figure 6.16 K_{II} with crack length at *h/w=1*

6.9 Results for a kinked crack under loading conditions of plane stress

Figure 6.16 shows that there is no absolute maximum in K_{II} with extending crack length. Therefore, in considering the growth of such a crack via the wing crack mechanism, it is not obvious which crack length should be taken, as it was in previous sections (see section 5.8 and 6.6). The analysis followed here assumes segment 1 of the crack to be perpendicular to the half plane surface, and of length $a_1 / w = 0.1$. This length is somewhat longer than in the previous cases considered (sections 5.8 and 6.6), but is used to ensure that any deleterious effects of the stress singularity at *h/w=1* are insignificant.

Figure 6.17 shows the stress intensity factors at the tip of the wing crack as it extends. As for other such plots (Figures 4.12, 5.17 and 6.11), it is found that the stress intensity factors reflect the shapes of the corresponding direct and shear stresses from the mode II singular field, show in Figure 4.2. Also, Figure 6.17 shows that as the wing crack length increases, the mode I stress intensity factor diminishes, leading to self arrest of the crack.

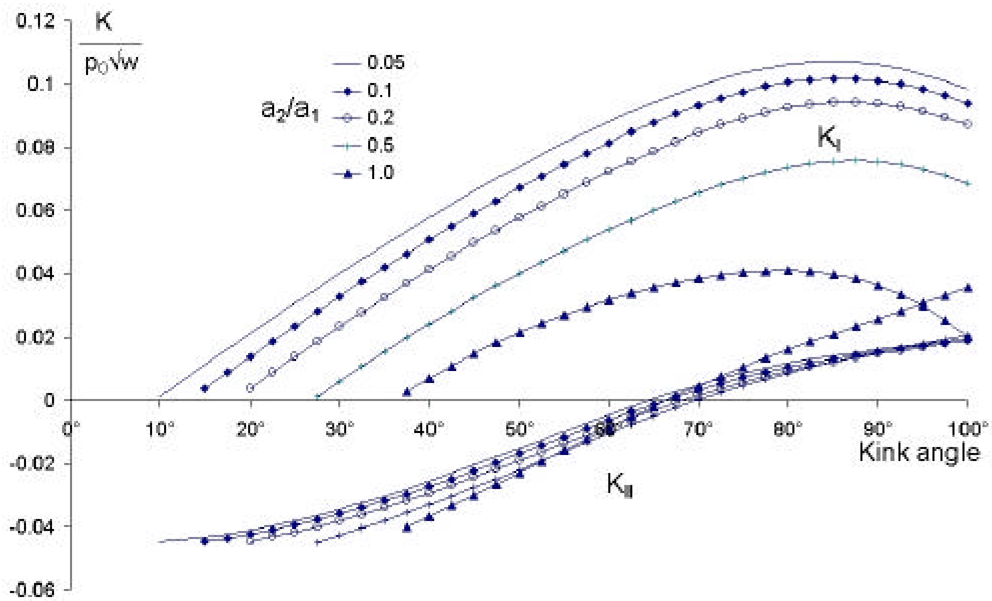

Figure 6.17 Stress intensity factors with kink angle

In Figure 6.18 the maxima for each K_I curve of the preceding figure are plotted against the wing crack length for which they occur. It is interesting to note that this curve does not decay to zero as quickly as in the previous contact problems (Figures 5.18 and 6.12). Instead, it is more similar to the plot obtained for a kinked crack in a uniform compressive field (Figure 4.14), and therefore is also more susceptible to slow crack growth after wing crack initiation, as in the uniform compression case.

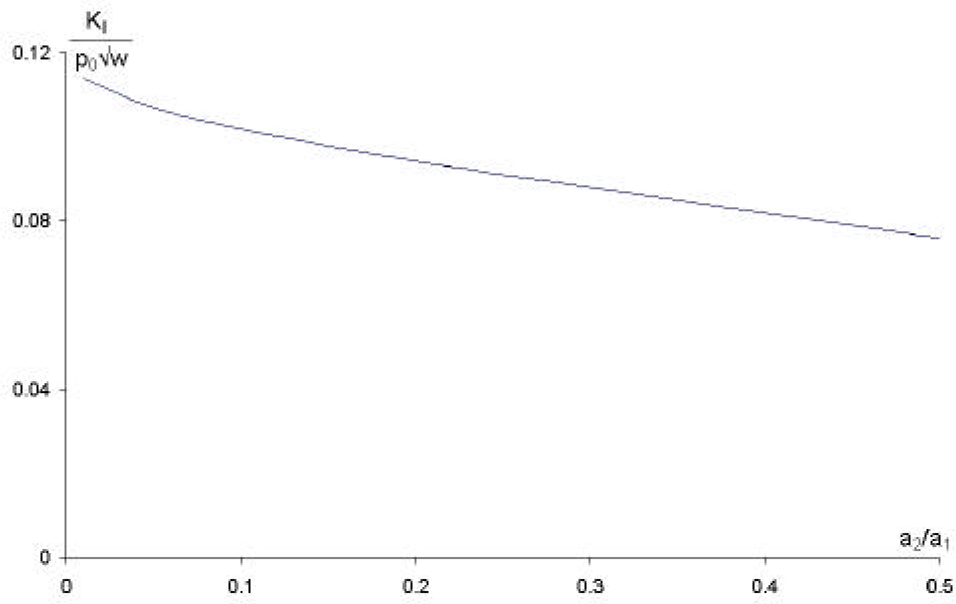

Figure 6.18 Maximum mode I stress intensity factor with wing crack length

6.10 Application of the Crack Size Design method to contact loading by a rigid punch via a rigid plastic interlayer

In this chapter, two types of contact loading have been investigated: plane strain and plane stress analyses of rigid punch loading of the half plane via a plastic interlayer. In both cases it has been shown that the stress state induced is sufficient to cause growth of wing cracks from pre-existing edge cracks. In previous investigations (sections 4.5 and 5.9), it has been shown that the wing crack growth mechanism may be satisfactorily incorporated into the new Crack Size Design method.

In section 4.5, six points were listed which described the behaviour of glass failure in a bulk compressive field. There have been no new developments in the current chapter which contradict these statements, and therefore the design method based upon them may be again applied here.

In section 4.5 the particular concern was growth of edge cracks in a uniform compressive field. In this case the mode II stress intensity factor for the straight edge crack increased in proportion to the square root of the crack length. This behaviour was also demonstrated in the plane stress results of section 6.8, but here the critical crack orientation is perpendicular to the edge. This characteristic makes the determination of an initial design crack size trivial. It is simply the same as that derived in section 2.5.2.1, that is, it is the same initial design crack as that used for an edge crack subject to far field tension. This is because in both cases the requirement is to find a perpendicular edge crack of sufficiently large size that it satisfies a given small probability of occurrence.

The behaviour of the straight edge crack due to loading under conditions of plane strain (section 6.5) showed similarities with that of the contact loading via an elastic interlayer (section 5.7). In both cases there was a maximum K_{II} for a finite crack length. In section 5.9 it was shown that this local maximum had an effect on the determination of the initial design crack in the crack size design procedure. It was noted that if an initial design crack (a_0^*), based on the derivation of section 2.5.2.1, were larger than the crack length for maximum K_{II}, $a_{contact}$, then the design case would not represent the worst case scenario. A modification to the determination of the initial design crack size was suggested to allow for this case, as described in equation (5.21). Since the stress intensity factors presented in section 6.5 exhibit the same behaviour of having an intermediate maximum, the same design method should be applied here for plane strain loading conditions.

With an initial design crack size evaluated, and corresponding to a maximum K_{II} likely to be encountered in the glass, design may proceed in the standard manner to allow for wing crack propagation. This design method was proposed in section 4.5, and will therefore not be reproduced here.

Chapter 7

Conclusion

In this thesis, issues relating to the use of glass in structural applications have been investigated. In such applications glass is required to support long term loads when used as a material for beams and columns. In Chapter 2 it was shown that the current design methods for glass, based predominantly on design against transient lateral loading for windows, do not adequately account for the behaviour of glass when used in these new applications. Addressing these shortfalls, and proposing new design methods, has been a primary object of this thesis. To do this, the fracture mechanics of a linear elastic material have been used to describe the behaviour of the glass and to incorporate this behaviour into a structural engineering design framework. In each chapter this integration was performed for a different physical case of loading or crack geometry.

Chapter 2 provided a review of the material properties of glass, and described its behaviour under the long term in-plane loading conditions of structural glass applications. It was shown that the strength of glass, and its fatigue with time, were determined by the cracks on its surface, and were therefore best described using fracture mechanics. A new design method was then developed, based on the principles of fracture mechanics and incorporating limit state design concepts. This new "Crack Size Design" method was proposed as an alternative to the allowable stress method currently used in structural glass design. Its basic design condition, which must be satisfied at all times during the life of the structure, can be expressed as:

$$K_I^* \leq f K_{IC} \tag{7.1}$$

where K_I^* is a design stress intensity factor, K_{IC} is the critical stress intensity factor, and f is a capacity reduction factor. The components used to generate the design stress intensity factor are the applied stress and the crack size.

In Chapter 3 it was demonstrated that in many glass applications the most common type of crack present along the glass edge did not extend right across the glass thickness, but was a thumbnail crack localised on the corner of the glass element. Investigations of the behaviour of such a crack under tensile stresses showed that the original Crack Size Design method could be extended to account for this case.

It is often the case in glass design that engineers search for the point of maximum tension and compare its magnitude to that of an allowable stress. If there is no zone of tension, then it is often thought that failure will not occur. In Chapters 4, 5 and 6, cases with no bulk tension were investigated. In Chapter 4 the case of an edge crack subjected to a uniform compressive field, such as that found in a column, was considered. In Chapters 5 and 6 the more complicated case of contact loading was investigated. It was shown that, even in compressive stress fields, brittle failure of glass was possible, and was a result of the existing cracks present in the glass. This had two important results. First, it showed that the consideration of cracks, as advocated in the Crack Size Design method, was essential to glass design. More importantly, it showed that even when there is no zone of tension, failure is still possible, and describable. This is particularly relevant to work with connection design. In this case, designers often perform detailed finite element analyses of the contact, ignoring the presence of cracks, and base design on the stresses calculated. Chapters 4, 5 and 6 show that this is not rigorous, and an unforeseen compressive failure may occur as a result.

Although Chapters 4, 5 and 6 consider a number of different loading cases, it was shown that each instance could be incorporated under the umbrella of Crack Size Design. In all cases the failure mechanism was compression wing cracking, but the critical initiating conditions varied. A modification was made to the original Crack Size Design formulation to allow for a different approach to the determination of the initial crack size. However, it should be noted that this was done in order to obtain the critical condition for the left hand side of equation (7.1), and therefore conforms to the basic tenet of the new design method.

It has been shown that Chapters 5 and 6 provide guidance on glass design for contact loading problems. However, the methods used in developing the solutions presented are also of significance as they have a relevance and applicability to the broader fracture mechanics field. Such methods include solution techniques for the stress intensity factors of an edge crack which is closed over all of its length with frictional sliding between the crack faces, or, a kinked edge crack in a compressive field whose upper segment is closed while the lower segment undergoes classical mode I opening. Also, the derivation of the stress fields induced in a half plane due to rigid punch loading via an interlayer, with various frictional conditions on either side of the layer, present some new innovations for such contact mechanics problems. All of these solution methods are numerically efficient, and therefore may be usefully applied in other non-glass related problems.

This thesis is the first to propose the Crack Size Design method, and therefore future possible work on the topic is almost limitless. There are particular points of interest which might be investigated first. These include an integration of the new design method with concepts of alternative load paths (discussed by Crompton (1999)), a more detailed investigation of the types of cracks encountered in structural glass applications and the residual stresses produced by glass processing, and the evaluation of some of the design factors, such as f, to comply with acceptable risk limits set out in international building codes. It is inevitable that, in the course of this future work, the detail of Crack Size Design will be modified, but it is important that the basic concept of founding glass design on the fracture mechanics criterion of equation (7.1) be preserved.

References

Alexander J.M., "The effect of Coulomb friction in the plane-strain compression of a plastic-rigid material", *Journal of the Mechanics and Physics of Solids*, Vol. 3, pp. 233-245, 1955.

Anderson T.L., *Fracture Mechanics – Fundamentals and Applications*, Second Edition, CRC Press, Florida, 1995.

Ashby M.F., Hallam S.D., "The failure of brittle solids containing small cracks under compressive stress states", *Acta Metallurgica*, Vol. 34, No. 3, pp. 497-510, 1986.

Bakioglu M., Erdogan F., Hasselman D.P.H., "Fracture mechanical analysis of self-fatigue in surface compression strengthened glass plates", *Journal of Materials Science*, Vol. 11, pp. 1826-1834, 1976.

Beason W.L., Morgan J.R., "Glass failure prediction model", *Journal of Structural Engineering*, Vol. 110, No. 2, pp. 187-212, 1984.

Benthall R.H., Johnson K.L., "An elastic strip in plane rolling contact", *International Journal of Mechanical Sciences*, Vol. 10, 637-663, 1968.

Brace W.F., Bombolakis E.G., "A note on brittle crack growth in compression", *Journal of Geophysical Research*, Vol. 68, No. 12, pp. 3709, 1963.

Charles R.J., "Static Fatigue of Glass II", *Journal of Applied Physics*, Vol. 29, No. 11, pp. 1554-1560, 1958.

Comninou M., Dundurs J., "Partial closure of cracks at the interface between a later and a half space", *Engineering Fracture Mechanics*, Vol. 18, No. 2, pp. 315-323, 1983.

Comninou M., "The Interface Crack", *Journal of Applied Mechanics*, Vol. 44, pp. 631-636, 1977.

Crompton P.R., "Assessment of Design Procedures for Structural Glass", M.Sc Thesis, Department of Engineering Science, The University of Oxford, 1999.

Dai D.N., Hills D.A., Nowell D., "Modelling of growth of three-dimensional cracks by a continuous distribution of dislocation loops", *Computational Mechanics*, Vol. 19, pp. 538-544, 1997.

Dewynne J.N., Hills D.A., Nowell D., "Calculation of the opening displacement of surface-breaking plane cracks", *Computer Methods in Applied Mechanics and Engineering*, Vol. 97, pp. 321-331, 1992.

Erdogan F., Gutpa G. D., Cook T. S., “Numerical solution of singular integral equations”, in *Methods of Analysis and Solutions of Crack Problems*, edited by G.C. Sih, Noordhoff, Leyden, pp. 368-425, 1973.

Evans A.G., “A method for evaluating the time-dependent failure characteristics of brittle materials and its application to polycrystalline alumina”, *Journal of Materials Science*, Vol. 7, pp. 1137-1146, 1972.

Evans A.G., “Slow crack growth in brittle materials under dynamic loading conditions”, *International Journal of Fracture*, Vol. 10, No. 2, pp. 251-259, 1974.

Fair L., “Structural Glass”, 4^{h} Year Project Thesis, The Department of Engineering Science, The University of Oxford, 1996.

Fischer-Cripps A.C., Collins R.E., “Architectural Glazings: Standards and Failure Models”, *Building and Environment*, Vol. 30, No. 1., pp. 29-40, 1995.

Griffith A.A., “The phenomena of rupture and flow in solids”, *Philosophical Transactions of the Royal Society of London, Series A*, Vol. 221, pp. 163-198, 1920.

Gutpa P. K., Walowit J. A., “Contact stresses between an elastic cylinder and a layered elastic solid”, *Transactions of the ASME, Series F, Journal of Lubrication Technology*, pp. 250-257, April 1974.

Hills D.A., Nowell D., Sackfield A *Mechanics of Elastic Contacts*, Published by Butterworth-Heinemann, Oxford, 1993.

Hills D.A., Kelly P.A., Dai D.N., Korsunsky A.M., *Solution of Crack Problems: The Distributed Dislocation Technique*, Kluwer Academic Publishers, Dordrecht, 1996.

Hoek E., Bieniawski Z.T., “Brittle fracture propagation in rock under compression”, *International Journal of Fracture Mechanics*, Vol. 1, No. 3, pp. 137-155, 1965.

Horii H., Nemat-Nasser S., “Brittle failure in compression: splitting, faulting and brittle-ductile transition”, *Philosophical transactions of the Royal Society of London*, Vol. A319, pp. 337-374, 1986.

Hopkins S.W., Rau C.A. Jnr., “Prediction of Structural crack growth behaviour under fatigue loading”, in *Fatigue Crack Growth Measurement and Data Analysis*, ed. Hudak S.J. Jnr. & Bucci R.J., American Society for Testing and Materials, Philadelphia, 1981.

Irwin G.R., “Analysis of stresses and strains near the end of a crack traversing a plate”, *Journal of Applied Mechanics*, Vol. 24, pp. 361-364, 1957.

Jaffar M.J., “Asymptotic behaviour of thin elastic layers bonded and unbonded to a rigid foundation", *International Journal of Mechanical Sciences,* Vol 31, pp. 229, 1989.

Jofeh C., *Structural Use of Glass in Buildings*, The Institution of Structural Engineers, London, 1999.

Johnson W., Mellor P.B., *Plasticity for mechanical engineers*, D. Van Nostrand Company Ltd, London, 1962.

Kelly P., Hills D.A., Nowell D., "Models for plastic constraint in brazed or diffusion-bonded joints between ceramic components", *Acta Metallurgica et Materialia*, Vol. 40, No. 9, pp. 2149-2154, 1992.

Kelly P., O'Connor J.J., Nowell D., "The use of Fourier transform theory in solving the two dimensional problem of an elastic layer in contact with or perfectly bonded to a substrate, suffering contact loading or containing a dislocation", Report No. OUEL 1979/93, The University of Oxford, UK, 1993.

Krenk S.Q., "On the use of the interpolation polynomial for solutions of singular integral equations", *Quarterly of Applied Mathematics*, Vol. 32, pp. 479-484, 1975.

Lawn B.R., *Fracture of Brittle Solids*, 2nd Edition, Cambridge University Press, Cambridge, 1993.

Levengood W.C., "Effect of origin flaw characteristics on glass strength", *Journal of Applied Physics*, Vol. 29, No. 5, 1958.

Murakami Y., *Stress Intensity Factors Handbook*, Volume 2, Pergamon Press, Oxford, p. 714, 1987.

Nemat-Nasser S., Horii H., "Compression-induced nonplanar crack extension with application to splitting, exfoliation, and rockburst", *Journal of Geophysical Research*, Vol. 87, No. B8, pp. 6805-6821, 1982.

Newman J.C. Jr, Raju I.S., "Stress-intensity factor equations for cracks in three-dimensional finite bodies subjected to tension and bending loads", *NASA Technical Memorandum 85793*, NASA, Hampton, Virginia USA, 1984.

Nowell D., Hills D.A., "Open cracks at or near free edges", *Journal of Strain Analysis*, Vol. 22, No. 3, pp. 177-185, 1987.

Nowell D., Hills D. A., "Contact problems incorporating elastic layers", *International Journal of Solids and Structures,* Vol. 24, pp. 105-115, 1988.

Ohji K., Kubo S., Tsuji M., "Life Prediction of surface crack propagation in plates with or without residual stresses under fatigue loadings", *Mechanical behaviour of materials - VI*, Vol. 2, Edited by Jono M., Inoue T., Pergamon Press, Oxford, 1992.

Overend M., Buhagiar D., Parke G.A.R., “Failure prediction – What is the true strength of glass?”, in *Glass in Buildings,* ed. Ledbetter S. & Harris R., Centre for Window and Cladding Technology, Bath, 1999.

Phillips C.J., “Fracture of glass”, *Fracture - An advanced treatise*, ed. Liebowitz H., Volume VII, Academic Press, New York, 1972.

Ritter J.E., Service T.H., Guillemet C., “Strength and fatigue parameters for soda-lime glass”, *Glass Technology,* Vol. 26, No. 6, 1985.

Scarr D., “Bearing Stresses in Glass”, 4h Year Project Thesis, The Department of Engineering Science, The University of Oxford, 1997.

Sedlacek G., Blank K., Güsgen J., “Glass in structural engineering”, *The Structural Engineer*, **73**, No. 2, pp. 17-22, 1995.

Sglavo V.M., Gadotti M., Micheletti T., “Cyclic loading behaviour of soda-lime silicate glass using indentation cracks”, *Fatigue and Fracture of Engineering Materials and Structures*, Vol. 20, No. 8, pp. 1225-1234, 1997.

Sneddon I.N., *Fourier Transforms* (Chapter 9), McGraw Hill, 1951.

Timonshenko S., Goodier J.N., *Theory of elasticity,* 3rd Edition, McGraw Hill, NY., 1970.

Vaughan H., “Crack propagation and the principal-tensile-stress criterion for mixed-mode loading”, Technical Note, *Engineering Fracture Mechanics*, Vol. 59, No. 3, pp. 393-397, 1998.

Way S., “Some observations on the theory of contact pressures”, *Journal of Applied Mechanics,* Vol 7, 147-157, 1940.

Weibull W., “A statistical theory of the strength of materials”, *Royal Swedish Institute for Engineering Research*, Vol. 151, 1939.

Wiederhorn S.M., Bolz L.H., “Stress corrosion and static fatigue of glass”, *Journal of the American Ceramic Society*, Vol. 53, pp. 543-548, 1970.

Williams J.M., McKenzie H.W., *Float glass edge strength overview*, Group Research Report GR/97/126, Pilkington, Lathom, UK, 1997.

Williams M.L., “Stress singularities resulting from various boundary conditions in angular corners of plates in extension”, *Journal of Applied Mechanics,* Vol. 19, 526-528, 1952.

Wren S., “Testing of Structural Glass Columns”, 4th Year Project Thesis, The Department of Engineering Science, The University of Oxford, 1998.

Yingzhi L., Hills D.A., “Stress intensity factor solutions for kinked surface cracks”, *Journal of*

Strain Analysis, Vol. 25, No. 1, 1990.

Zhao W., Sutton M.A., "Elastic solutions for corner cracks undergoing uniform displacement-controlled loading", *International Journal of Fracture*, Vol. 70, pp. 335-346, 1995.

Appendix A

Development of an expression for time to failure

It is desired to find the time to failure, t_f, for a piece of glass with initial crack size a_0 and subject to a stress s. This is done by examining the rate of change of the size a of the crack. The following have been given earlier in Chapter 2.

$$K_I = Y\sigma\sqrt{\pi a} \qquad \ldots (2.1)$$

$$\frac{da}{dt} = v = v_0\left(\frac{K_I}{K_{IC}}\right)^n \qquad \ldots (2.2)$$

Combining these gives:

$$\frac{da}{dt} = v_0\left(\frac{Y\sigma\sqrt{\pi}}{K_{IC}}\right)^n a^{n/2} \qquad (A.1)$$

For a period of constant stress the only variable on the right hand side is a, so that equation (A.1) can be integrated:

$$\int a^{-n/2}\,da = \int v_0\left(\frac{Y\sigma\sqrt{\pi}}{K_{IC}}\right)^n dt \qquad (A.2)$$

Leading to:

$$\frac{2}{2-n}\left(a^{(2-n)/2}-a_0^{(2-n)/2}\right)=v_0\left(\frac{Y\sigma\sqrt{\pi}}{K_{IC}}\right)^n t \tag{A.3}$$

or

$$\sigma^n t=\frac{2}{(n-2)v_0}\left(\frac{Y\sqrt{\pi}}{K_{IC}}\right)^{-n}\left(a_0^{(2-n)/2}-a^{(2-n)/2}\right) \tag{A.4}$$

Where a_0 is the crack size at $t=0$. For predictions of the time to failure t_f, the final crack size is equal to the critical crack size:

$$a=a_c=\frac{1}{\pi}\left(\frac{K_{IC}}{Y\sigma}\right)^2 \tag{A.5}$$

Substituting equation (A.5) into equation (A.4) and rearranging gives the lifetime of a glass member with initial crack size a_0 under a constant stress of σ:

$$t_f=\frac{2}{(n-2)v_0}\left(\frac{Y\sqrt{\pi}}{K_{IC}}\right)^{-n}\left(a_0^{(2-n)/2}-\left[\frac{1}{\pi}\left(\frac{K_{IC}}{Y\sigma}\right)^2\right]^{(2-n)/2}\right)\sigma^{-n} \tag{A.6}$$

Equation (A.6) can be used to generate strength versus time plots such as in Figures 2.5 and 2.6.

Appendix B

Derivation of a probabilistic crack size using the Weibull distribution

For a set of glass tensile failure test results the Weibull distribution (Weibull, 1939) can be written (Beason & Morgan, 1984):

$$P_{Survival}(A_0) = \exp\left[-kA_0\sigma^m\right] \tag{B.1}$$

where $P_{Survival}(A_0)$ is the probability of survival of a test specimen of area A_0 subjected to an applied stress σ. k and m are Weibull distribution variables.

The Weibull parameters must be determined from specimens which are tested in the same way as the glass is to be loaded. In this case the test set must be for abraded edges in tension. Note that m is dimensionless and k has the dimensions $\text{length}^{-2} \times \text{stress}^{-m}$.

Rearranging equation (2.1) and substituting it into equation (B.1) gives the probability P of survival of a specimen of area A_1.

$$P = \exp\left[-kA_1 \left(\frac{K_{IC}}{Y\sqrt{\pi}} \right)^m a^{-m/2} \right] \tag{B.2}$$

Which can be rearranged to give the size of the failure initiating crack for the given failure stress and probability.

$$a = \left(\frac{K_{IC}}{Y\sqrt{\pi}} \right)^2 \left(-\frac{kA_1}{\ln P} \right)^{2/m} \tag{B.3}$$

Appendix C

Review of the analysis method for an interlayer on a half plane substrate

The theory used by Kelly *et al.* (1993) is reproduced here, in part, for completeness. It follows the method set out by Sneddon (1951) and used elsewhere (for example Gutpa & Walowit (1974)).

The solution technique makes use of Airy Stress functions (Timonshenko & Goodier, 1970) in the interlayer (Φ_L), and the half plane substrate (Φ_S). These are, by definition, related to the stress components by

$$s_{xx} = \frac{\partial^2 \Phi}{\partial y^2}, s_{yy} = \frac{\partial^2 \Phi}{\partial x^2}, t_{xy} = -\frac{\partial^2 \Phi}{\partial x \partial y} \tag{C.1}$$

and hence, through Hooke's Law, to the displacements by

$$\begin{aligned}
\frac{\partial u_x}{\partial x} &= \frac{1+n}{E}\left\{(1-n)s_{xx} - n s_{yy}\right\} \\
\frac{\partial u_y}{\partial y} &= \frac{1+n}{E}\left\{(1-n)s_{yy} - n s_{xx}\right\} \\
\frac{\partial u_x}{\partial y} + \frac{\partial u_y}{\partial x} &= \frac{2(1+n)}{E} t_{xy}
\end{aligned} \tag{C.2}$$

under plane strain. To recover the plane stress solution replace n by $n/(1+n)$ inside the curly brackets in the first two of the equations.

Fourier transforms, $G(l, y)$, of the stress functions are now introduced, defined by

$$G(l, y) = \int_0^\infty \Phi(x, y)\cos(l x)dx$$

and

$$\Phi(x, y) = \frac{2}{p}\int_0^\infty G(l, y)\cos(l x)d l \tag{C.3}$$

Kelly *et al.* (1993) show that G has the form,

$$G(l, y) = [A + Bly]\cosh(ly) + [C + Dly]\sinh(ly) \tag{C.4}$$

Note that Sneddon (1951) and others use exponential rather than trigonometric arguments in equation (C.4).

To solve for four unknown coefficients in both the interlayer and substrate ($A_{L/S}$, $B_{L/S}$, $C_{L/S}$ and $D_{L/S}$) boundary conditions are invoked. First, the stress functions are continuous over the interlayer/substrate interface. Secondly, stresses also vanish at an infinite depth in the substrate. Further, the frictional conditions under the punch and along the interlayer/substrate interface are also used to specify either a continuous tangential displacement (adhesion), or zero shear stress (perfect lubrication). The final condition arises from the normal traction at the top of the interlayer. Using the expression for σ_{yy} from equations (C.1) and (C.3) it can shown that the applied stress, *p(x)*, must satisfy the following;

$$-p(x) = -\frac{2}{p}\int_0^\infty l^2 G\Big|_{y=b} \cos(lx)\,dl \qquad \text{(C.5)}$$

The boundary conditions given above are sufficient to solve for the eight unknowns, $A_{L/S}$, $B_{L/S}$, $C_{L/S}$ and $D_{L/S}$. Using equations (C.1) and (C.2) the stresses and displacements in the interlayer and substrate may be expressed in terms of these eight variables. The resulting expressions are given in Appendix D.

Appendix D

Expressions for stresses and displacements in an interlayer and half plane substrate for all combinations of adhesion and full lubrication along both interlayer surfaces

This appendix gives the expressions for the stresses and displacements in the interlayer and substrate. This has been done for all four combinations of adhesion and full lubrication along the two interfaces. The equations for the condition of a frictionless punch/interlayer connection and adhered interlayer/substrate interface (case 1) are as given by Kelly *et al*. (1993). The remaining three cases are novel. The solutions are also valid for both conditions of plane strain and plane stress.

Preliminary definitions

Young's Modulus, E_i

Poisson's ratio, ν_i

In plane strain, $\kappa_i = (3-4\nu_i)$

In plane stress, $\kappa_i = \dfrac{(3-\nu_i)}{(1+\nu_i)}$

$$\mu_i = \frac{E_i}{2(1+\nu_i)}$$

i = S, L for the substrate and interlayer respectively.

$$\Gamma = \frac{m_L}{m_S}$$

Dundurs' constants

$$a = \frac{\Gamma(k_S + 1) - (k_L + 1)}{\Gamma(k_S + 1) + k_L + 1}, \quad b = \frac{\Gamma(k_S - 1) - (k_L - 1)}{\Gamma(k_S + 1) + k_L + 1}$$

Explicitly, the stress and displacement components developed by a normal contact pressure on the top of the interlayer are

$$s_{xxL} = +\frac{2}{p}\int_0^\infty \left\{ \begin{array}{l} \left[A_{NL} + B_{NL}\, l\hat{y} + 2D_{NL}\right]\cosh(l\hat{y}) \\ \qquad + \left[2B_{NL} + C_{NL} + D_{NL}\, l\hat{y}\right]\sinh(l\hat{y}) \end{array} \right\} \frac{\tilde{p}_c(l)}{w}\cos(l\hat{x})\,dl \quad \text{(D.1)}$$

$$s_{yyL} = -\frac{2}{p}\int_0^\infty \left\{ \begin{array}{l} \left[A_{NL} + B_{NL}\, l\hat{y}\right]\cosh(l\hat{y}) \\ \qquad + \left[C_{NL} + D_{NL}\, l\hat{y}\right]\sinh(l\hat{y}) \end{array} \right\} \frac{\tilde{p}_c(l)}{w}\cos(l\hat{x})\,dl \quad \text{(D.2)}$$

$$t_{xyL} = +\frac{2}{p}\int_0^\infty \left\{ \begin{array}{l} \left[B_{NL} + C_{NL} + D_{NL}\, l\hat{y}\right]\cosh(l\hat{y}) \\ \qquad + \left[A_{NL} + B_{NL}\, l\hat{y} + D_{NL}\right]\sinh(l\hat{y}) \end{array} \right\} \frac{\tilde{p}_c(l)}{w}\sin(l\hat{x})\,dl \quad \text{(D.3)}$$

$$\frac{u_{xL}}{w} = +\frac{1}{pm_L}\int_0^\infty \left\{ \begin{array}{l} \left[A_{NL} + B_{NL}\, l\hat{y} + \frac{1}{2}(K_L + 1)D_{NL}\right]\cosh(l\hat{y}) \\ \qquad + \left[\frac{1}{2}(K_L + 1)B_{NL} + C_{NL} + D_{NL}\, l\hat{y}\right]\sinh(l\hat{y}) \end{array} \right\} \tilde{p}_c(l)\frac{\sin(l\hat{x})}{l}\,dl \quad \text{(D.4)}$$

$$\frac{u_{yL}}{w} = +\frac{1}{pm_L}\int_0^\infty \left\{ \begin{array}{l} \left[\frac{1}{2}(K_L - 1)B_{NL} - C_{NL} - D_{NL}\, l\hat{y}\right]\cosh(l\hat{y}) \\ \qquad + \left[-A_{NL} - B_{NL}\, l\hat{y} + \frac{1}{2}(K_L - 1)D_{NL}\right]\sinh(l\hat{y}) \end{array} \right\} \tilde{p}_c(l)\frac{\cos(l\hat{x})}{l}\,dl \quad \text{(D.5)}$$

where $\tilde{p}_c(l) = w\int_0^\infty p(x)\cos(l\hat{x})\,d\hat{x}$ (D.6)

The expressions for the displacement fields show the correct *form*, but the integral is found to be infinite, as the vertical displacement in an infinite half plane cannot be defined. If the origin is taken as the reference point, the surface normal displacement becomes

$$\frac{u_{yL}}{w} = +\frac{1}{pm_L}\int_0^\infty \left(\left\{ \begin{aligned} &\left[\frac{1}{2}(K_L - 1)B_{NL} - C_{NL} - D_{NL}\, l\hat{y}\right]\cosh(l\hat{y}) \\ &+ \left[-A_{NL} - B_{NL}\, l\hat{y} + \frac{1}{2}(K_L - 1)D_{NL}\right]\sinh(l\hat{y}) \end{aligned} \right\}\cos(l\hat{x}) - \frac{1}{2}(K_L - 1)B_{NL} + C_{NL} \right)\frac{\tilde{p}_c(l)}{l}\,dl \tag{D.7}$$

Expressions for the substrate may be obtained by substituting S for L in all the above equations.

Evaluation of the Coefficients

The above equations contain the coefficients $A_{NL}, B_{NL}, C_{NL}, D_{NL}$, $A_{NS}, B_{NS}, C_{NS}, D_{NS}$. Their values depend on the boundary conditions. The degree of friction between the punch and the interlayer (f_1) and that connecting the interlayer to the substrate (f_2) is either frictionless (0) of fully adhered (∞).

First, define the following frequently occurring expressions.

$$P = \frac{1}{4(b-a)(1+b)}$$

$$Q = 1 - a^2$$

$$R = (1-a)(a-1-2b)$$

$$S = (1+a)^2 + 2b(a-1-2b) \tag{D.8}$$

$$T = \frac{1}{2}\frac{(a-1)}{(a-b)}$$

$$U = \frac{(a-1)}{(a+1)}$$

$$V = \frac{1}{2}\left(\frac{2b-a-1}{a-b}\right)$$

The cœfficients are then explicitly given by the following set of equations.

Case 1: Frictionless top surface and fully adhered bottom surface, f_1=0, f_2= ¥

$$B_{NL} = \frac{(PR+1)\sinh(l\hat{b}) - (PQ - l\hat{b})\cosh(l\hat{b})}{(l\hat{b})^2 - PS(PR+1) + P(S-R)\cosh^2(l\hat{b}) + PQ[\sinh(2l\hat{b}) - PQ]}$$

$$D_{NL} = \frac{-(PS+1)\cosh(l\hat{b}) - (PQ + l\hat{b})\sinh(l\hat{b})}{(l\hat{b})^2 - PS(PR+1) + P(S-R)\cosh^2(l\hat{b}) + PQ[\sinh(2l\hat{b}) - PQ]}$$

$$A_{NL} = P(QB_{NL} + RD_{NL})$$

$$C_{NL} = P(SB_{NL} - QD_{NL})$$

$$A_{NS} = C_{NS} = A_{NL}$$

$$B_{NS} = D_{NS} = C_{NL} - A_{NL} + B_{NL} \qquad \text{(D.9)}$$

Case 2: Frictionless top and bottom surfaces, f_1=0, f_2=0

$$B_{NL} = \frac{l\hat{b}\cosh(l\hat{b}) + \sinh(l\hat{b})}{U\cosh(l\hat{b})\sinh(l\hat{b}) - \cosh^2(l\hat{b}) + 1 + Ul\hat{b} + (l\hat{b})^2}$$

$$D_{NL} = \frac{(U + l\hat{b})\sinh(l\hat{b})}{U\cosh(l\hat{b})\sinh(l\hat{b}) - \cosh^2(l\hat{b}) + 1 + Ul\hat{b} + (l\hat{b})^2}$$

$$C_{NL} = -B_{NL}$$

$$A_{NL} = UB_{NL}$$

$$A_{NS} = C_{NS} = A_{NL}$$

$$B_{NS} = D_{NS} = -A_{NL} \qquad \text{(D.10)}$$

Case 3: Fully adhered top and bottom surfaces, f_1=¥ , f_2=¥

$$B_{NL} = \frac{(PQ - l\hat{b})\sinh(l\hat{b}) - (PR + T)\cosh(l\hat{b})}{T\{P(R-S)\cosh(l\hat{b})\sinh(l\hat{b}) - 2PQ\cosh^2(l\hat{b}) + PQ - l\hat{b}\}}$$

$$D_{NL} = \frac{(PQ + l\hat{b})\cosh(l\hat{b}) + (PS + T)\sinh(l\hat{b})}{T\{P(R-S)\cosh(l\hat{b})\sinh(l\hat{b}) - 2PQ\cosh^2(l\hat{b}) + PQ - l\hat{b}\}}$$

$$A_{NL} = P(QB_{NL} + RD_{NL})$$

$$C_{NL} = P(SB_{NL} - QD_{NL})$$

$$A_{NS} = C_{NS} = A_{NL}$$

$$B_{NS} = D_{NS} = C_{NL} - A_{NL} + B_{NL} \qquad \text{(D.11)}$$

Case 4: Adhered top surface and frictionless bottom surface, f_1=¥ , f_2=0

$$B_{NL} = \frac{-T\cosh(l\hat{b}) - l\hat{b}\sinh(l\hat{b})}{T\cosh(l\hat{b})\sinh(l\hat{b}) + [l\hat{b}(1+V-T) - UT]\cosh^2(l\hat{b}) - l\hat{b}(R+1)}$$

$$D_{NL} = \frac{(U + l\hat{b})\cosh(l\hat{b}) + V\sinh(l\hat{b})}{T\cosh(l\hat{b})\sinh(l\hat{b}) + [l\hat{b}(1+V-T) - UT]\cosh^2(l\hat{b}) - l\hat{b}(R+1)}$$

$$C_{NL} = -B_{NL}$$

$$A_{NL} = UB_{NL}$$

$$A_{NS} = C_{NS} = A_{NL} \qquad \text{(D.12)}$$

Appendix E

Mixed boundary value problem formulation

As part of the work undertaken in developing the solutions for Chapter 5, the formulation presented here was investigated. It deals with an algebraic formulation for a mixed boundary value problem, which, in general, is difficult to obtain. Boundary conditions of both displacement and stress criteria are incorporated in one equation. Solution of this equation is not forthcoming, thus leading to the use of dislocations in Chapter 5. However, it is thought that there is some merit in presenting the formulation here, for possible future reference.

Consider an interlayer on a rigid substrate being compressed by a vertical pressure over a width of $-w$ to $+w$, which results in a compressive normal stress at every point along the interlayer/substrate interface. The interface is subject to Coulomb friction. There is a central zone over which the interlayer "sticks" to the substrate (ie. where the friction is sufficient to cause the horizontal displacement, u_x, to be zero) which extends from $-d$ to $+d$. Outside this region the shear stress is $\pm f\sigma_{yy}$. The problem is to be able to specify the boundary condition over the interlayer/substrate interface for the above shear and displacement conditions.

Kelly *et al.* (1993) show that the horizontal displacement may be evaluated using

$$u_x = \frac{1+v}{2pE}\int_{-\infty}^{\infty}\left[(1-v)\frac{\partial^2 G}{\partial y^2}+va^2 G\right]i\frac{e^{-iax}}{a}\partial a \tag{E.1}$$

Noting that $u_x=0$ for the central zone, and differentiating with respect to y gives

$$0 = \frac{1}{2p}\int_{-\infty}^{\infty}\left[(1-v)\frac{\partial^3 G}{\partial y^3}+va^2\frac{\partial G}{\partial y}\right]i\frac{e^{-iax}}{a}\partial a \tag{E.2}$$

Simplifying equation (E.2) leads to

$$\frac{1}{2p}\int_{-\infty}^{\infty} ia\frac{\partial G}{\partial y}e^{-iax}\partial a = \frac{(v-1)}{v2p}\int_{-\infty}^{\infty}\frac{\partial^3 G}{\partial y^3}i\frac{e^{-iax}}{a}\partial a \tag{E.3}$$

It is now noted, from Kelly *et al*. (1993), that the left hand side of equation (E.3) is the definition of $\tau_{xy}(x,y)$. Equation (E.3) is, therefore, the expression for the shear stress when $u_x=0$.

Now consider the shear stress along the interface. The definition, from Kelly *et al.* (1993), is

$$t_{xy}(x,y) = \frac{1}{2p}\int_{-\infty}^{\infty} ia\frac{\partial G}{\partial y}e^{-iax}\partial a \tag{E.4}$$

Taking the Fourier inverse leads to

$$ia\frac{\partial G}{\partial y} = \int_{-\infty}^{\infty} t_{xy}(x,y)e^{iax}\partial x \tag{E.5}$$

Substitution for τ_{xy} according to the respective regions of behaviour gives

$$ia\frac{\partial G}{\partial y} = \int_{-\infty}^{d} fs_{yy}(x,y)e^{iax}\partial x + \int_{-d}^{d}\left[\frac{(v-1)}{v2p}\int_{-\infty}^{\infty}\frac{\partial^3 G}{\partial y^3}i\frac{e^{-iax}}{a}\partial x\right]e^{iax}\partial x + \int_{d}^{\infty} - fs_{yy}(x,y)e^{iax}\partial x \tag{E.6}$$

Equation (E.6) is an expression which combines the boundary conditions of both displacement and stress into a single expression, and therefore constitutes a true mixed boundary value formulation. However, solution of this equation is difficult, and therefore has not been pursued further here.